UNIVERSITÀ DEGLI STUDI DI PARMA

DIPARTIMENTO DI FISICA

Structural and Electronic Properties of Strongly Correlated Molecular Systems

Fabio Gianferrari

Thesis submitted for the award of the degree of Ph.D. in Physics
Dottorato di Ricerca in Fisica

Supervisor: Prof. Mauro Riccò

XX Ciclo – Gennaio 2008

This document was typeset in Adobe® Utopia and Computer Modern Roman
by the author using the LaTeX2ε software.
The file in Portable Document Format was generated with pdfTeX version 14h.

AUTHOR'S ADDRESS

Fabio Gianferrari
Dipartimento di Fisica
Università degli Studi di Parma
Parco Area delle Scienze, via G.P. Usberti 7/A, I-43100 Parma, Italy
E-MAIL: Fabio.Gianferrari@fis.unipr.it

Contents

List of Figures

Introduction

In the last 20 years atomic clusters have attracted great interest, at first in the field of basic science, and later in engineering and technology. The elements, in their cluster phase, show physical and chemical properties often different from those in the bulk phase [101]. It is known that in metal clusters valence electrons keep the shell structure typical of systems with confined electrons [27], thus, no metallic features arise. The increasing interest in cluster investigation can be principally motivated by this reason: based on the electronic structure of metal clusters, the possibility of using clusters as atom-like building blocks for new materials becomes realistic [90]. This point of view was further on encouraged with the discovery of C_{60} (Kroto 1985, see ref. [62]), and, even more, with the discovery of crystalline solid C_{60} (simultaneously with the macroscopic production method of fullerenes, Krätshmer and Huffman, 1990, ref. [61]), where fullerenes form a face centered cubic crystalline lattice. C_{60} is surely one of the most interesting clusters which has been intensively studied up to now. This 60-carbon atom cluster is the most stable and symmetric molecule belonging to the fullerenes family. Since the discovery of fullerenes many research efforts have been addressed to the development of new carbon based materials with the aim to synthesize new classes of materials interesting for applications in different technological fields, ranging from nanoelectronics to nuclear medicine. Nevertheless to further emphasize the importance of basic research, it is worth noticing that the discovery of C_{60} represents, first of all, a wonderful example of serendipity (unexpected discovery). During experiments aimed at understanding the formation mechanism of long-chain carbon molecules in interstellar space (investigations considered as part of the intriguing background of “basic science”) the super symmetric 60-carbon atom molecule appeared from the laser irradiation of graphite [62]. This discovery, moreover, was followed by another remarkable one: the possibility of doping the pristine C_{60} with alkali atoms yielding the formation of the well known charge transfer salts: the fullerides [48]. These fullerene compounds belong to the intriguing class of strongly correlated molecular systems, and are characterized by remarkable electronic properties like superconductivity [52] (A_3C_{60}, where A is the alkali metal) and other effects arising from the strong electron correlation. Thanks to the high C_{60} redox stability, the principal feature which can be ascribed to these new materials is, however, the changing of electronic properties upon stoichiometric variation of the alkali doping atom. This is, of course, inherited directly from the molecular properties of C_{60} which, moreover, maintain a leading role in the determination of the crystal properties in fullerides. Starting from this framework, many research efforts in the field of physics, chemistry, and material science, have been devoted to the extension of the remarkable electronic properties of fullerides to different molecular systems, not only C_{60}-based. This Ph.D thesis shows the results obtained in this research line working on different solid state molecular compounds whose building block is respectively the fullerene molecule or the phthalocyanine molecule. In the former case our research effort has been devoted first to the synthesis of a new class of C_{60} compounds, namely *fullerenium salts*, then to the structural and magnetic characterization of such new materials, where the C_{60} is present, for the first time in the solid state, in its oxidized form C_{60}^{2+}. In the latter case the metal phthalocyanines solid state compounds have been studied upon alkali metal doping with the aim to investigate a phenomenology possibly similar to the one of fullerides, as previously reported [23]. The characterization has been performed with SQUID magnetometry, X-rays diffraction (XRD), muon Spin Relaxation (μSR), and Nuclear Magnetic Resonance (NMR). A summary of the reported techniques will be presented in the Chapter 2.

Chapter 1

Strongly correlated systems

Physical systems that are well understood from a theoretical point of view usually are described in terms of ensembles of free particles or pseudo-particles. These toy models, then, are developed in the perspective to understand the phenomenology of more complicated systems. For example, semiconductors and many metals can be described as having non-interacting electrons. This simple approach is valid because the interaction (Coulomb) energy of electrons is much smaller than their kinetic energy. Another example is alkali atoms, that show Bose-Einstein condensation at low temperatures. Alkali atoms can be treated as non-interacting bosons because their scattering length (i.e. the length at which they interact with each other) is much smaller than the average distance between the particles.

However there are important systems for which interactions between the particles are not weak, and these interactions play a major role in determining the properties of such systems. The most remarkable features which may arise in such "strongly correlated systems" are reported in the following.

1. *Superconductivity.* For cuprates the origin of superconductivity is still unclear, but it is commonly believed that it comes mostly from the Coulomb interaction between the electrons [18], rather than the electron-ion interactions that are important for the conventional superconductors. What is also intriguing about the cuprates is that superconductivity appears in materials that are not good metals to begin with. In fact their normal state properties are so unusual that they are often called "strange metals".

   The intercalation compounds of C_{60}, namely *fullerides*, show s-wave superconductivity with critical temperature surprisingly high, if compared with the conventional s-wave superconductors [44]. These compounds belong, by all means, to the class of strongly correlated systems; in the case of the superconducting ones (A_3C_{60}, where A represents the intercalated alkali metal) it is widely accepted that superconductivity arises from a conventional phonon-mediated mechanism; nevertheless their unconventional phenomenology is not so far completely understood.

2. *Metal-insulator transitions.* These transitions consist in a sudden change in electrical conductivity due to a reversible change from localized to itinerant behaviour of the electrons. Many examples of similar phenomenology can be found in the fullerene compounds: this is the case of ammonia-intercalated fullerides [94], where the insertion of ammonia in the crystal lattice induces a Mott-Hubbard transition to an insulating and magnetic state in $NH_3K_3C_{60}$ [55], while, on the contrary, K_3C_{60} show superconductivity at 19 K. Since in these molecular systems, ammonia is supposed to act as a simple lattice spacer, in $NH_3K_3C_{60}$ the superconductivity can be recovered applying external pressure [112].

3. *Magnetic ordering.* As a consequence of a mott-Hubbard transitions the electron localization takes place yielding an insulating state. An antiferromagnetic ordering is also expected in the insulating phase, since, if the onsite Coulomb energy is large but not infinite, each electron site in the ground state remains singly occupied, however an electron can briefly visit its neighbour's site if the neighouring spins are antiparallel: in this case an energetic saving occurs promoting an antiparallel arrangement of the spins. The system turns out to be an antiferromagnet.
   Moreover a remarkable example of magnetic ordering in C_{60}-based materials is the well known ferromagnetic compound TDAE-C_{60}.
   The TDAE molecule (tetrakis-dimethylaminoethylene) donates one of its electrons to the C_{60} producing the $TDAE^+$-C_{60}^- charge-transfer compound. At the time of the discovery [2], its Curie temperature $T_c = 16$ K was one order of magnitude higher than the ones of the other organic ferromagnets: it is a surprisingly high transition temperature for a compound comprising only carbon, hydrogen and nitrogen, which gave a strong input to the research in the field of p-electron ferromagnetism.

1.1 Fullerenes and Fullerides

The molecule of C_{60} was discovered in 1985 by H. W. Kroto [62] during researches on long chains of carbon atoms in interstellar space; it is the most stable symmetrical molecule of the fullerenes family (C_{70}, C_{84},...,C_{100} and others, bigger molecules). Nevertheless the great interest for this super symmetric new carbon allotropic form, the microscopic quantities of C_{60} (and also C_{70}) synthesized for the first time by Kroto et. al., with the method of laser evaporation of graphite in inert gas atmosphere, hindered, initially, the research in this field. The first apparatus for mass production of fullerenes was developed in 1990 by Krätshmer and

Huffman (University of Arizona, USA, [61]): this gave an important input in the studies of fullerenes, available from that moment, on a macroscopic quantity, within the soot produced in the Krätshmer reactor. Here the evaporation of graphite take place through a voltaic arc in helium atmosphere.

1.1.1 The C_{60} molecule

Taking a closer look to the most interesting molecule of the family, the C_{60}, one sees that the 60 carbon atoms are arranged at the vertexes of a truncated icosahedron which could roughly fit into a sphere of about 7 Å diameter.

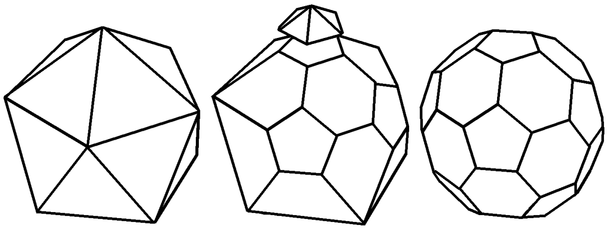

Figure 1: Truncated icosahedron

The structure of fullerene molecule belongs to the Icosahedral point group (I_h) having up to 120 symmetry operations. The regular truncated icosahedron is obtained from the regular icosahedron by passing planes normal to each of the 6 fivefold axes passing through the center of the icosahedron so that the edges of the pentagonal faces thus formed are equal in length to the edges of the hexagonal faces. The interesting electronic properties of the molecule arise from the π molecular orbitals originated from the sp^2-like atomic orbitals of each carbon atom of the molecule [87]. Each carbon atom is placed among two hexagonal faces and a pentagonal face, and it is linked to the other carbon atoms by three molecular bonds. The lengths are slightly different for the two different types of bonds: 1.45 Å for the ones shared between pentagonal and hexagonal faces, and 1.40 Å for the “so called” double bond shared between two hexagonal faces.

The *σ-bonding sp^2* electrons involved in the formation of the C_{60} cage are 180. These levels are deep in energy and completely occupied; they contribute to the structural stability of the molecule.

The remaining 60 electrons are distributed in the π molecular orbitals reported in figure 3. In particular the highest occupied molecular orbital (HOMO) has h_u symmetry and degeneracy 5, while the lowest unoccupied molecular orbital (LUMO), has t_{1u} symmetry and triple degeneracy. C_{60} is, thus, a diamagnetic molecule with a HOMO-LUMO gap of $\sim$ 1.7 eV; moreover these electronic structure shows an exceptional stability upon electron doping, yielding to the formation of the well-known C_{60} intercalation compounds, the *fullerides* [38]. It is

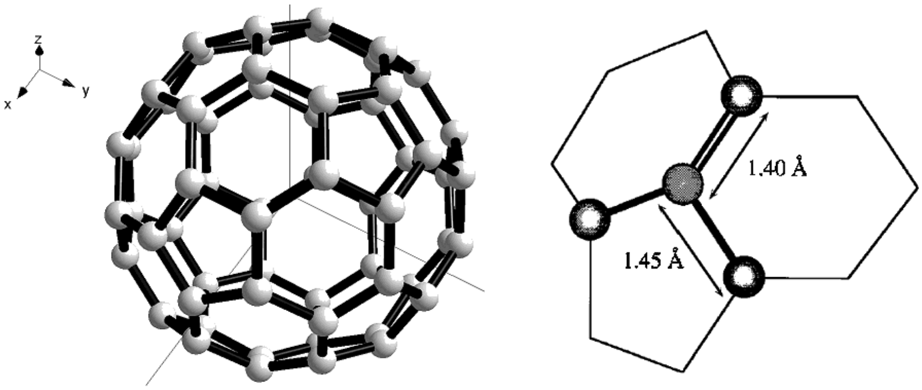

Figure 2: C_{60} molecule and shared bonds for each carbon atom: all the carbons atoms see the same electronic background. The bond angles formed inside the hexagons are $\sim 120°$, as in graphite, while the other bond angle (inside the pentagonal face) is about 108°, due to the sensible deviation from planar geometry. The molecular radius is reported to be 3.55 Å [87].

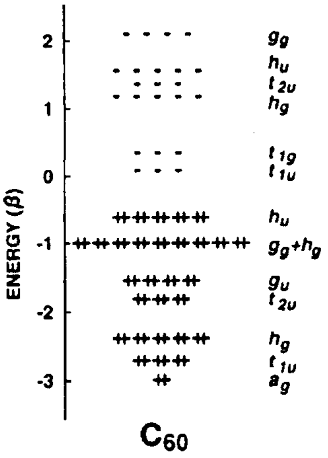

Figure 3: C_{60} molecular levels.

worth noticing that it is the progressive filling of LUMO-derived band, that gives rise, in the solid state, to the remarkable electronic properties of the alkali-doped fullerides, discussed in the section 1.1.3.

1.1.2 Crystalline C_{60}: fullerite

The C_{60} molecule in the solid state is an insulating plastic crystal whose electronic properties are inherited from the molecular ones. For this reason the understanding of the characteristics of the free molecule is, as expected, a fundamental starting point to understand the properties of the solid state C_{60}, namely *fullerite*. The weak interaction between molecules suggests that many of the molecular orbitals symmetry properties could be transferred, with minor variations, to the corresponding band, originated in the solid state. The energy levels, shown in figure 3 came from extended Huckel calculations [87].

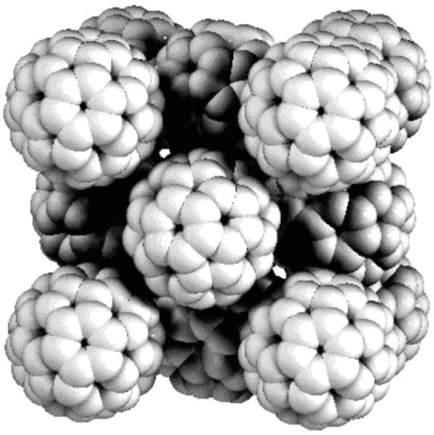

Figure 4: The fcc structure of the *fullerite*.

The fullerite particular properties are summarized in the following.

- The crystal structure is a face centered cubic lattice with $Fm\bar{3}m$ space group. The lattice spacing is 14.17 Å, and the nearest neighbours distance is 10.18 Å: there are, thus, many void spaces in the structure. For each C_{60} two *tetrahedral* sites and another one with *octahedral* symmetry can be identified. These empty sites are progressively filled with the alkali atoms during the intercalation reaction of the pristine C_{60} crystal.

  Taking a closer look to the fullerite it is worth noticing that symmetry translation however is no longer valid in this compound because it is a plastic crystal. This means that crystalline order is present only for the nodes of the lattice, but the translational symmetry for each carbon atom in the C_{60} molecule is violated. This situation yields to the presence of rotational degrees of freedom for the molecules, which determine the complex dynamical behaviour of pristine C_{60} as a function of temperature [104, 111, 110]. At room temperature the molecules show an isotropic rotation due to the thermal energy; upon cooling the system undergoes dynamical phase transitions yielding the freezing of the isotropic rotation; moreover, in an intermediate temperature region, rotations about fixed axes having quantized orientations take place (*ratcheting* phase [10, 87]). This characteristic behaviour has been probed with Nuclear Magnetic Resonance (NMR) [104].

- Based on the group theory, no Bravais lattice with fivefold symmetry is possible: a symmetry lowering, thus, is expected to occur when fullerenes crystallize in the solid state. Indeed the $Fm\bar{3}m$ space group does not include the icosahedral point group I_h, thus not all the icosahedral symmetry elements are preserved when the C_{60} molecules are placed in a fcc lattice. This results in the presence of three inequivalent carbon atoms on each molecule in the *fcc* lattice, breaking, thus, the equivalence of every carbon atom in the isolated C_{60}. Since at room temperature the fullerene molecules rotate isotropically, this situation arise only at temperature T<90 K where the C_{60} rotational dynamics is blocked. In these condition, thus, the fullerite crystal shows a peculiar molecular ordering, namely *merohedral disorder*: it consists in the presence of two different orientations of the C_{60}, randomly "chosen" by the molecules with equal probability, yielding, thus, a disordered molecular distribution. Several articles and reviews describe this subject, e.g. [7,53,87].

- The weakness of the Van der Vaals intermolecular interactions gives rise to *narrow bands* in the solid state. Consequently the HOMO- and LUMO-derived bands do not overlap (the bandwidth is estimated to be $\sim$ 0.5 eV) yielding an insulating compound having the Fermi level placed in the middle of the gap between HOMO- and LUMO-derived bands. Together with the narrow bandwidth, moreover, the high degeneracy of the molecular energy levels, produces a relatively high *density of states* (DOS) for partial filling of the HOMO- or LUMO-derived bands. In particular the latter, with degeneracy 3, if progressively filled with electrons upon alkali ions doping, yields the formation of the fullerides, the intercalation C_{60} salts with different electronic properties, depending on the alkali atom stoichiometry.

1.1.3 Alkali-doped fullerides

After the production of solid C_{60}, various fullerene compounds with metallic elements called fullerides (A_xC_{60} where A = K, Rb, Cs) have been produced. In this section a description about the charge transfer salts obtained intercalating the pristine C_{60} with alkali atoms will be provided.

The alkali metals generally promote a complete charge transfer and become cations; the alkali-metal ionic radius is quite smaller than the atomic radius, so that the steric hindrance is reduced and the intercalant can fit better into the lattice spacings. There is a nearly complete charge transfer, at least for $x \leq 6$; this demonstrates that the fullerene molecule is a strong electron acceptor, and may, therefore become C_{60}^{6-} in the solid state.

As previously reported, fullerides electronic properties depend strongly on the stoichiometry of the doping metal (see tab. 1). In particular, considering as a first approximation a simple band-filling model we could easily guess how the A_3C_{60} show, at room temperature, a metallic behaviour, while the A_6C_{60} are insulating. This is due respectively to the half-filling and the complete filling with $6n$ electrons of the LUMO-derived band.

Usually fullerides showing a polymeric structure are A_1C_{60}: neighbourings fullerene molecules form true covalent bonds between either one or two of the p_z-like orbitals (which acquire a sp^3 character). However it is worth noticing that Li_4C_{60} represents a singular case, for A_4C_{60},

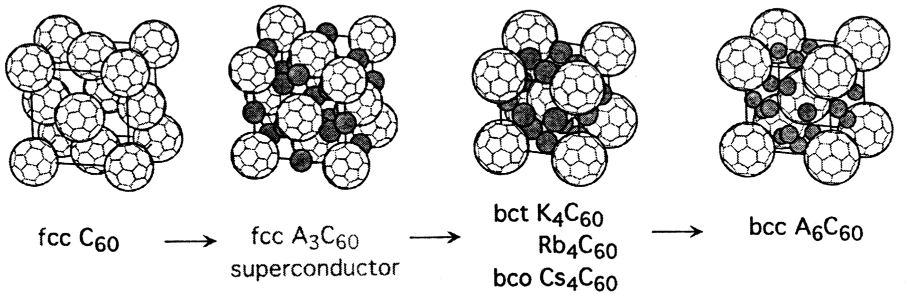

Figure 5: Fullerides

alkali stoichiometry	electronic properties	crystal structure
A_1C_{60}	insulating	polymer structure
A_3C_{60}	metallic and super-c T_c ranging from 10 to 40 K	fcc
A_4C_{60}	non metallic Jahn-Teller distortion	*bct*
A_6C_{60}	insulating	*bcc*

Table 1: Variability of the fullerides electronic properties as a function of the alkali atom stoichiometry. Metallicity at room temperature and superconductivity arise in A_3C_{60} (with T_c ranging from 10 to 40 K). The non metallic nature of A_4C_{60} can be ascribed to strong correlation effects: the Jan-Teller distortion, lifting the LUMO-band degeneracy, yields an insulating state.

because its room temperature structure is polymeric (characterized by the formation of [2+2]-cycloaddition in one direction [75, 93]); moreover it depolymerizes at about 250 °C, yielding a monomer cubic structure with metallic character [9, 88].

The A_3C_{60} phase is the most important one concerning superconductivity; all of the alkali metal fullerides that are superconducting crystallize in this structure. Filling of octahedral and tetrahedral sites of the fcc lattice are complete in the A_3C_{60}: no structural phase transitions take place upon cooling, indeed, for alkali stoichiometry $x \leq 3$, while the system undergoes to structural transition from a *fcc* phase to a *bcc* one, for higher doping stoichiometry.

The A_2C_{60} and A_5C_{60} do not exist in a pure phase: such alkali stoichiometry values are always index of two mixed phases, with the only exception of Na_2C_{60}; due to thermodynamical reasons the A_3C_{60} phase is the most stable and its formation is highly preferred in the annealing treatments usually performed to obtain the alkali metals intercalation within the solid.

1.1.4 Strong correlation effects in A_3C_{60} and A_4C_{60}

Band theory calculations find out a width of $W \sim 0.5$ eV for t_{1u} band, while the on-site Coulomb repulsion U can either be estimated as ~ 1 eV or be measured using Auger spectroscopy for solid C_{60} as 1.6 eV [69]. Basing on the Hubbard model, the system Hamiltonian is made up of two components. The first component is the hopping integral. The hopping integral is typically represented by the letter t and it represents the kinetic energy of electrons hopping between atoms; for metallic systems $t = W/2$. The second term in the Hubbard model is then the on-site repulsion, typically represented by the letter U: it represents the potential energy arising from the charges of the electrons.

We can guess that, for the reported values of U/W, these systems are Mott insulators, very close to the metal-insulator transition. In particular the metal-insulator transition, in the standard, non degenerate, Hubbard model, should take place for U/W values ~ 1.5 or less. Realistic U/W values for fullerides were estimated by O. Gunnarsson to range from 1.5 to 2.5, so that all alkali-doped fullerides should have been insulators, in contradiction to experimental results [45]. However from a detailed study of the effects of orbital degeneracy on the metal-insulator transition came out that the presence of such a degeneracy, together with the partial filling of the relative band (t_{1u} band for alkali-doped fullerides) result in a shift of the U/W critical value from ~ 1 to $\sim \sqrt{d}$, where d is the degeneracy. The shift contribution of partial band filling is maximum for half-filling conditions, as shown by Quantum Monte-Carlo calculations, while it is reduced upon moving from half-filling. This explanation can justify why A_3C_{60} show a metallic behaviour, as expected from a simple band filling model. Moreover to get in more detail in this analysis other effect must be taken into account:

- the different crystal symmetry between A_3C_{60} (fcc) and A_4C_{60} (bct);
- the competition between Jahn-Teller effect and Hund's rule, influencing the band filling;
- the strong electron-phonon coupling with intra-molecular high energy phonons which can induce superconductivity, as well as the mentioned Jahn-Teller effect;

In fullerene compounds two different phonon groups with different energy ranges can be identified: the low energy *inter*-molecular phonons and the high-energy *intra*-molecular ones.

The Jahn-Teller effect essentially arises from the electron-phonon interaction where the coupling is with *intra*-molecular modes; in the strong-coupling condition, for degenerate systems, it promotes a symmetry breaking and removes the band degeneracy. This results in different electronic configurations depending on the band filling. For the described effect to take place, it is necessary that the energy gain from the degeneracy lift compensates the increase of potential energy due to the symmetry loss. The situation becomes even more complicated due to the possibility for Jahn-Teller effect, to be both *static* or *dynamic*, which will not be discussed here.

By summarizing, we can conclude that, due to the assumed values for U/W ratio ($1.5 \div 2.5$), fullerides are molecular systems so close to a Mott-Hubbard transition, that it gives rise to a borderline situation in which contributions from several comparable effects may decide the final properties of each compound.

Consequently, despite their apparent similarity, based on incomplete band filling, the A_3C_{60} and A_4C_{60} fullerides show completely different magnetic and transport properties, because of the different balance of the various strong-correlation effects.

In particular, in the case of A_4C_{60} the following effects prompt for the formation of a non magnetic insulating state:

1. the *bct* crystal symmetry: it promotes the development of a gap for U/W values smaller than in the case of a fcc lattice [50];
2. the reduced increasing effect of the U/W ratio, due to degeneracy;
3. the partial band filling, different from x=3;
4. Jahn-Teller effect: in a triple degenerate band, it induces a splitting between the degenerate band states, but only for even integer filling of the band itself ($x = 2, 4$).

Thus, for the same reason, the Jahn-Teller contribution, together with the stronger effects of the fcc lattice symmetry and U/W increase, yields the formation of a metallic state in A_3C_{60}.

A separate paragraph will be dedicated, now, to a brief description of the phenomenology related to the C_{60} superconductors, showing unconventional features, like unexpectedly high critical temperatures (see table 2), that cannot be ascribed simply to the strong coupling condition.

1.1.5 Superconductivity in A_3C_{60}

It is widely accepted that the superconductive mechanism in fullerene superconductors A_3C_{60} (A = K, Rb, Cs) is the conventional phonon mediated electron pairing; however their phenomenology, as well as the superconductive parameters values cannot be thoroughly described within the BCS framework [8], even considering its natural extension for strong-coupling, Migdal-Eliashberg (ME) theory [79,35]). The reason for this singularity is that in superconducting fullerides a borderline situation arise in which the energy scale for electrons and C_{60} H_g intra-molecular phonons are very close one to each other.

This yields the breakdown of the classical adiabatic approximation which states that electron and lattice dynamics can be treated separately as far as electrons energies are higher

C_{60} superconductors	**Lattice constant** (Å)	T_c (K)
Na_2RbC_{60}	14.028	2.5
Na_2CsC_{60}	14.133	11
K_3C_{60}	14.253	19.2
K_2RbC_{60}	14.299	21.8
K_2CsC_{60}	14.292	24
KRb_2C_{60}	14.364	26
Rb_3C_{60}	14.436	29.4
$(NH_3)_4Na_2CsC_{60}$	14.473	29.6
Rb_2CsC_{60}	14.493	31.3

Table 2: Superconducting fullerides

than phonon energies: the fullerene compounds are, thus, intrinsically nonadiabatic. Consequently, the electron-phonon coupling of these half-filled band metals cannot be treated anymore within the framework of the adiabatic approximation. In fullerides this condition is no longer satisfied because the phonons giving rise to superconductive coupling, as well as the other strong correlation effects, are the intra-molecular C_{60} modes (represented in figure 6): the stiffness of the C_{60} molecule, provides, indeed, particularly high phonon frequencies (up to 0.2 eV). On the other hand, the low density of carriers and the molecular character of the solid give rise to a small electron bandwidth (W=0.5 eV, as previously assumed) [45].
In particular semi-empirical calculations and Raman spectroscopy [44] have shown that the tangential C_{60} modes (Hg(7) and Hg(8) with frequencies 1428 and 1575 cm^{-1}, respectively; see table 3) are those mainly responsible for the electron-phonon coupling.

By summarizing, the most remarkable fact related to the unconventional phenomenology of A_3C_{60} fullerides consists in their high superconductive critical temperature (up to 40 K for Rb_3C_{60} in high pressure conditions). These values cannot be justified within the theoretical background of conventional theories (BCS and Migdal-Eliashberg theory), as previously asserted.

Moreover, another notable unconventional feature regards, by all means, the isotope effects. In this case, due to the strong interplay between lattice and electron dynamics in fullerene superconductors, such effects are expected to influence also physical quantities which, in the conventional BCS framework, are not modified by the isotopic mass substitution.

The dependence of the superconducting transition temperature T_c on the isotopic mass ($T_c \propto M^{-\alpha}$, with $\alpha_{T_c} \simeq 0.5$), has been historically considered as the “smoking gun” of phonon mediated superconductivity [8]. However, the many published reports concerning the carbon isotope effect on the T_c of A_3C_{60} give very different results, still not well un-

	Energy (cm^{-1})					
Modes	Varma[a]	Jishi[b]	Antropov[c]	Quong[d]	Faulhaber[e]	Expt.[f]
$H_g(8)$	1721	1575	1462	1576	1567	1575
$H_g(7)$	1596	1401	1387	1443	1425	1428
$H_g(6)$	1406	1217	1290	1244	1200	1250
$H_g(5)$	1260	1102	1091	1093	1067	1099
$H_g(4)$	924	788	785	767	750	774
$H_g(3)$	711	708	753	727	640	710
$H_g(2)$	447	439	454	439	421	437
$H_g(1)$	263	296	281	258	249	273
$A_g(2)$		1468	1463	1499	1493	1470
$A_g(1)$		492	458	478	459	496

Table 3: Frequencies of C_{60} modes (adapted from ref. [44]): [a]Varma *et al.* 1991; [b]Jishi *et al.*, 1992; [c]Antropov, Gunnarsson *et al.*, 1993; [d]Quong *et al.*, 1993; [e]Faulhaber *et al.*, 1993; [f]Bethune *et al.*, 1991.

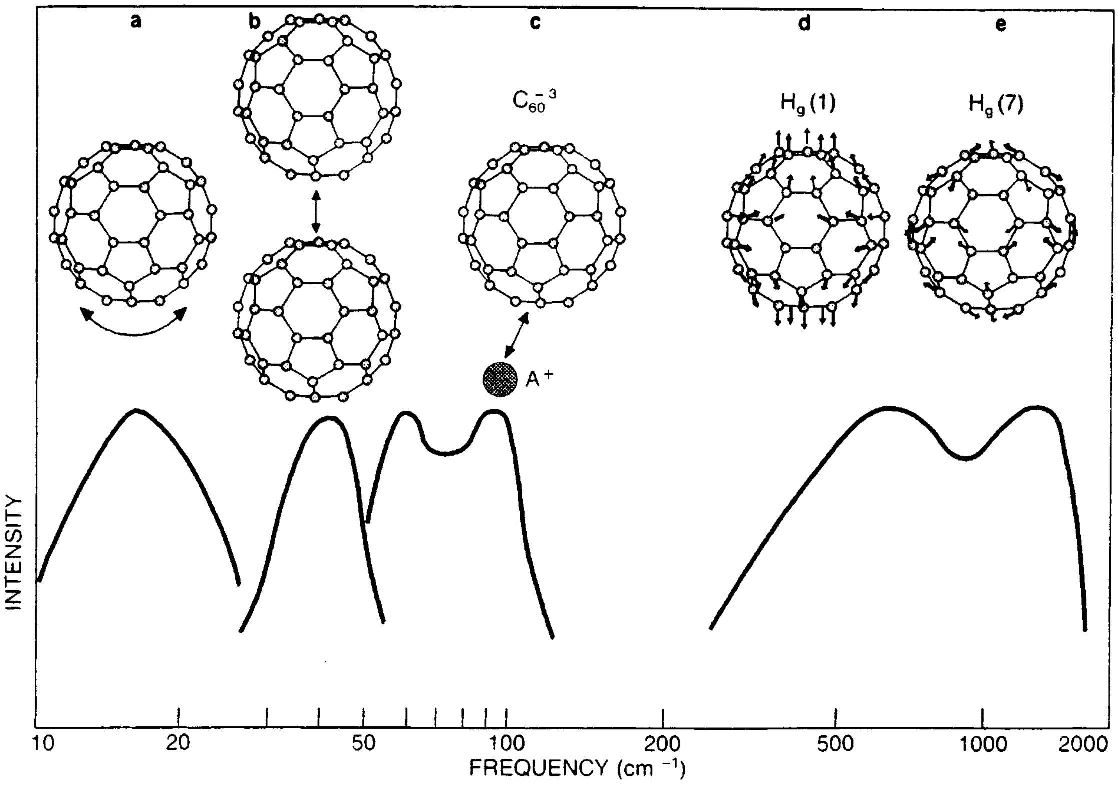

Figure 6: Phonons in the C_{60} superconductors: (a) librations; (b) optical phonons C_{60}-C_{60}; (d) and (e) intra-molecular modes H_g [44].

derstood, and apparently not correlated to each other [39]. Due to these reasons, for the first time a direct observation of these unconventional effects on Pauli spin susceptibility has been provided, using both SQUID magnetometry and NMR measurements [92]. The isotopic shift in Pauli susceptibility, χ_P, has been determined from the comparison between 85% ^{13}C-enriched K_3C_{60} samples and natural ^{13}C abundance samples. We found, surprisingly, that the numerical value or the sign of the shift do not agree with the best theoretical estimates [84], hinting at a still more complex phenomenology than that currently taken into account.

However a dramatic negative isotope shift was found on χ_P: this effect measured first by magnetometry, and successively confirmed also by NMR, represents a clear, though only qualitative, evidence of an unconventional, non ME behaviour.

1.2 Phthalocyanines

Transition-metal Phthalocyanines are well known for their industrial applications: these compounds present wide applications as dyes [43] and catalysts [83]. The recent interest for metal phthalocyanines (MPc), in the field of material science, arise from the possible existence of a close analogy between the electronic properties of their salts and the fullerides.

A first indication on this regard was given in 2004 [103]; in this work the authors pointed out the interest in doping the nontransition metal phthalocyanines (ZnPc, MgPc and others). In these systems the extra electrons should occupy the $2e_g$ orbital (LUMO) with double degeneracy. Since MPcs are characterized by a strong on-site electron repulsion U and intra-site Jahn-Teller couplings, in the condition of half-filling $n = 2$ there will be competition between Hund's rule exchange J (favouring the triplet state) and the Jahn-Teller coupling E_{JT} with the molecular MPc vibrations (favouring a singlet state). The values of the coupling strength, moreover, although not accurately known in MPcs, seem to be very similar to those present in fullerides, where U=1 eV, E_{JT}=0.15 eV, J=0.03 eV, W=0.5 (being W the width of the LUMO-derived band). Taking into account the Hamiltonian for electrons in e_g orbitals of the phthalocyanine molecules and the hopping term between neighbourings sites, Tosatti *et. al.* [103] showed that the resulting Hamiltonian could be studied by Dynamical Mean Field Theory (DMFT) yielding a very rich phase diagram as a result. In a doping region very close to the half-filling ($n = 2$) many effects may arise, such as Mott transitions or strongly correlated superconductivity.

Furthermore in phthalocyanines thin films an interesting behaviour of the conductivity versus potassium doping (using vapors) has been found by Craciun *et. al.* [21, 22, 23]. The results will be presented in the paragraph 1.2.2.

Part of this thesis work was devoted to the investigation of this molecular systems in order to mimic the remarkable properties of the fullerides, as the behaviour of the electronic

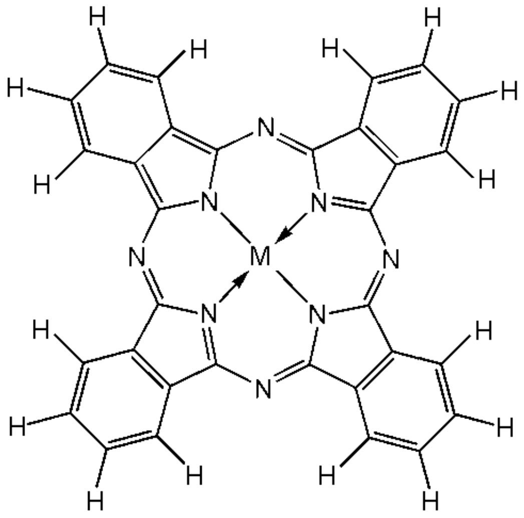

Figure 7: The phthalocyanine molecule

properties upon alkali atoms doping.

1.2.1 The phthalocyanine molecule

The phthalocyanines are macrocyclic compounds formed by carbon, nitrogen, hydrogen. The molecule can coordinate hydrogen and metal cations in its center by coordination bonds with the four nitrogen atoms. Most of the elements have been found to be able to coordinate to the phthalocyanine macrocycle. Therefore, a variety of phthalocyanine complexes exist.

We are interested in *metal phthalocyanines* (MPc) where M is a bivalent metal (Co^{2+}, Cu^{2+}, Zn^{2+}, Mg^{2+} etc.) [66,77].

The generic MPc molecule is represented in figure 7; the bonds formed by the metal ion with the inner nitrogen atoms present both covalent and ionic character. The other two nitrogen atoms interact with the metal ion with two coordination bonds, stabilizing the molecule.

The mentioned analogy between phthalocyanines solid state compounds and fullerides originates, eventually, from the redox stability of the molecule, which only recently have attracted the scientific community. Theoretical investigations of the electronic structure of different MPc-s by density-functional methods (DFT) [67] evidence that these molecules are able to assume several oxidation states, thanks to the stabilizing action of the phthalocyanine ring, which acts as an electron buffer during the oxidation and reduction of the metal.

The molecular levels calculated for some phthalocyanines are shown in figure 8. The HOMO orbital is generally localized on the central metal atom [23,67], while the LUMO $2e_g$ level corresponds to an electron delocalization on the internal ring. As previously discussed the double degeneracy of the LUMO orbital in the solid state, is responsible for the interesting

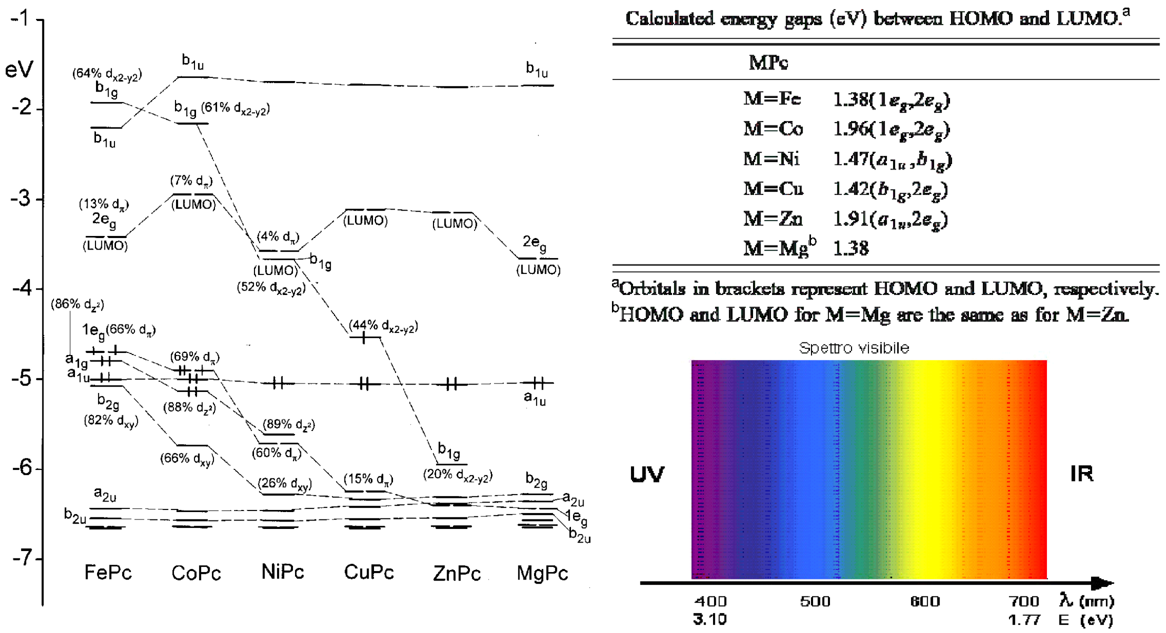

Calculated energy gaps (eV) between HOMO and LUMO.[a]

MPc	
M=Fe	1.38($1e_g$,$2e_g$)
M=Co	1.96($1e_g$,$2e_g$)
M=Ni	1.47(a_{1u},b_{1g})
M=Cu	1.42(b_{1g},$2e_g$)
M=Zn	1.91(a_{1u},$2e_g$)
M=Mg[b]	1.38

[a] Orbitals in brackets represent HOMO and LUMO, respectively.
[b] HOMO and LUMO for M=Mg are the same as for M=Zn.

Figure 8: Phthalocyanines molecular levels

effects discussed in the next paragraph and, can maybe, justify the experimental results on thin phthalocyanines films, mentioned in the paragraph 1.2.

1.2.2 Phthalocyanines in the solid state

Phthalocyanines, in the solid state, exhibit different polymorphic structures in which a 1-dimensional stacking of the molecules can be identified, giving rise to chains. The orientation of the molecules with respect the stacking direction characterizes the different polymorphs and influences the electronic properties of the compound. The same phthalocyanine may present, in the solid state, polymorphs with different magnetic properties (as in the case of

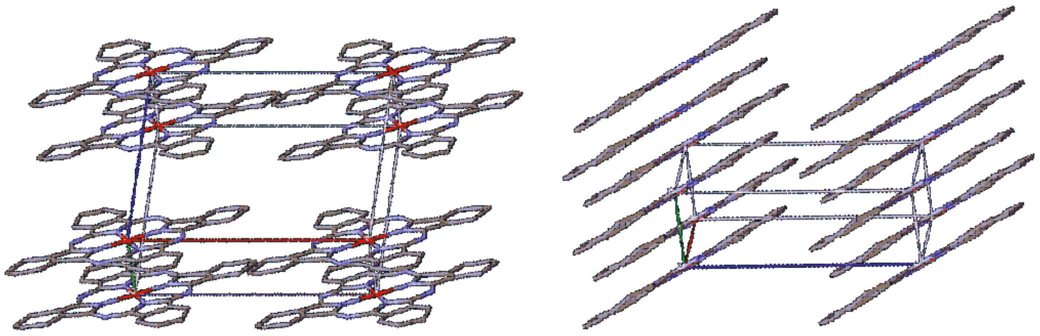

Figure 9: Packing of metal-phthalocyanines in the solid state: 1-D stacking yields the formation of chains

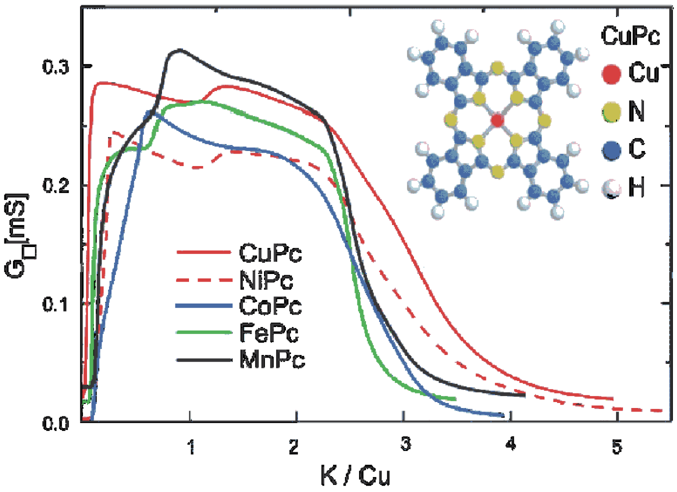

Figure 10: Conductivity in MPc thin films for different potassium doping levels. Adapted from [23, 22]

CoPc) because the stacking angle modifies the molecular orbitals overlap (both for intra-chain and inter-chain orbitals). A typical chain-stacking structure is shown in figure 9.

The molecular character of the compounds originated, in the solid state, by the phthalocyanines should be quite evident, even if this issue is so far under debate [9]. The mentioned double degeneracy of the LUMO orbital is expected to determine, in the band structure, a situation quite similar to the case of fullerides, where the LUMO-derived band, thanks to the level degeneracy, may accept $3n$ electrons giving rise to the well known tuning of the A_3C_{60} electronic properties through electron doping. In the case of the phthalocyanines LUMO orbital, with double degeneracy, it is expected to reach the half-filling condition, in the LUMO-band, doping with 2 electrons.

This point has been tested recently, as introduced in the paragraph 1.2, in the experimental work of Craciun *et. al.* [23]; they performed experiments on thin phthalocyanines films in order to test the behaviour of the film conductance as a function of electron doping. Treating the films with potassium vapors, the electron transfer from the alkali atoms to the phthalocyanine inner ring should take place.

The results are reported in figure 10 which shows the square film conductance as a function of the electron transfer: a transition to a metallic state appears in the region between 1 and 2 electrons transferred (a slight dependence of the conductive region on the specific phthalocyanine is also observed). Our experimental work was, thus devoted to the extension of such results to the bulk phases in the solid state. Phthalocyanines powder samples were characterized by X-Ray diffraction, SQUID magnetometry, and μSR.

In particular our work was focused on lithium phthalocyanines, due, essentially, to experimental reasons which will be discussed in the section 3. These phthalocyanines present two

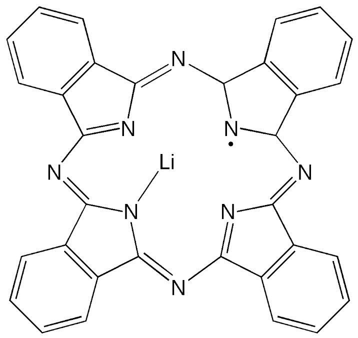

Figure 11: LiPc molecule: the intrinsic magnetism arise from the unpaired electron localized in the inner nitrogen atom

stable forms at room temperature: LiPc and Li_2Pc. The former is quite particular because it is a radical. Thus, it is interesting in the pure phase for its intrinsic magnetic properties due to the presence of an unpaired electron in a nitrogen atom of the inner ring (see figure 11).
LiPc SQUID characterization was discussed in detail in the Ph.D thesis of Dr. Matteo Belli *Magnetic and Transport Properties of Intercalated Fullerides* [9].
In the present work μSR results on LiPc will be shown as well as results of Li_2Pc characterization upon progressive lithium doping.

1.3 Fullerenium salts

The C_{60} molecule, thanks to its remarkable redox stability, give rise to the fullerides upon electron doping. The electron properties of these compounds arise from the LUMO-derived band. In analogy a very interesting research perspective was identified in the synthesis (and characterization) of a new class of C_{60} molecular compounds, the *Fullerenium salts* where the HOMO-derived band may assume a leading role in the determination of the electronic properties.
The first compound belonging to such a new class of C_{60}-based materials has been synthesized in the research group of prof. Mauro Ricco', working on strongly correlated, carbon-based, molecular materials.

The fullerene molecule, in this case, is present for the first time in the solid state, in its oxidized form C_{60}^{2+}; thus the hole-doping of the HOMO-derived band is expected to take place in a hypothetical fullerenium salt having a fulleride-like band structure.

In this perspective one of the most interesting subjects of our research line concerns by all means the magnetism in new carbon-based materials. A theoretical investigation of the magnetism in C_{60} isolated ions has been performed by Lüders *et. al.* [63, 64] in order to shed more light on the possible analogies or differences between the negative C_{60}^{n-} and the positive C_{60}^{n+} ions. The ground-state spin for the charge states ranging from -3 to +5 has

been computed taking into account the electron electron and electron-vibration interactions. The former, through the Coulomb exchange, promotes the molecular Hund's rule magnetism, while the latter through the Jahn-Teller distortions favors the spin pairing providing an energy gain for the low spin states and, thus, quenching the magnetism. In particular previous hints can be found in the literature [6, 73] outlining how for C_{60}^{n-} ions the contribution from JT interaction is expected to overcome the Coulomb exchange leading the C_{60}^{2-} ion, as well as C_{60}^{4-} to be non magnetic. The results reported in the reference [64], on the contrary, predict the ion C_{60}^{2+} to be magnetic being its ground state with spin S=1 30 meV lower in energy than the spin state S=0.
Although this prediction con not be straightforward extended to the solid state compounds it represents a strong input in the investigation of the magnetic property of the fullerenium salt $C_{60}(AsF_6)_2)$, since, for the first time in this case the C_{60} cation C_{60}^{2+} can be studied in the solid state.

Moreover, in the perspective of doping with holes the HOMO-derived band starting from fulleride-like band structure, others predictions, related to the superconductivity, motivate the research on fullerene cations.
Considering that superconductivity of alkali doped fullerides was one of the major breakthroughs in fullerene science, the possibility to find a similar phenomenology in such new materials represented a strong input to this research line. In particular, classical theories of superconductivity indicate an exponential increase of T_c with the increase of the density of state (DOS) at the Fermi level, as well as the increasing of the e-ph coupling strength. Both these effects are enhanced in a hypothetical hole-doped fulleride-like superconductor which could keep cubic symmetry. We can guess this directly from the well known BCS formula

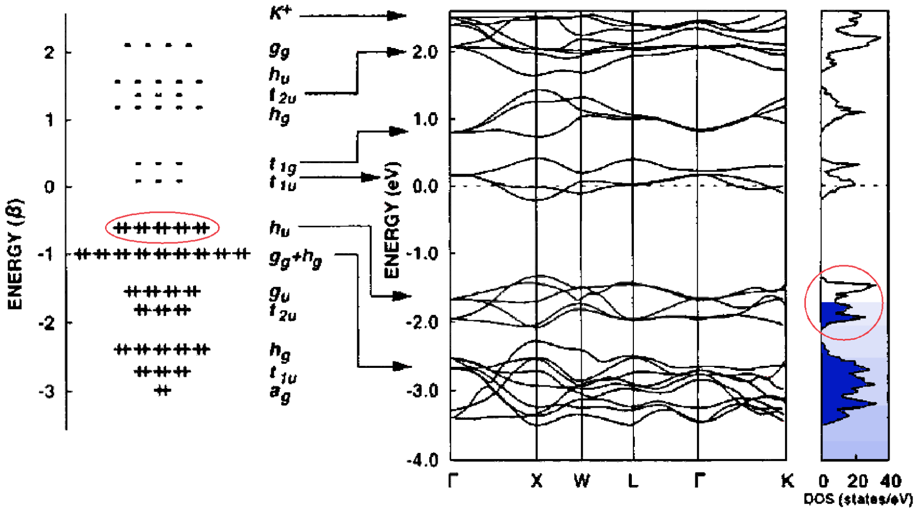

Figure 12: Hypothetical HOMO-band filling in a fulleride-like fullerenium superconductor

expressing T_c as a function of the phonon frequency,

$$k_B\ T_c = 1.14\hbar\omega_D e^{\left(-\frac{1}{V_0\ D(E_f)}\right)}, \tag{1}$$

where $D(E_f)$ represents the density of states at the Fermi level.
In the HUMO-band, the 5-fold degenerate h_g HOMO orbital gives rise to an higher DOS than in the case of alkali doped fullerides, where the 3-fold degenerate t_{1u} orbitals are involved (see figure 12).

Moreover BCS/Hartree-Fock calculations performed by Granath and Östlund [42] showed an interesting behaviour of the calculated superconducting T_c as a function of hole-doping in a *fcc* C_{60} crystal. They studied the effects of electronic correlations on the fullerene crystal taking into account strong intra-molecular electron-electron interactions. Preliminarily they solved the Hubbard model on a truncated icosahedron in second order perturbation theory in the on-site repulsion U. Based on the calculated HOMO states they built up an effective Hamiltonian for the interactions in a single C_{60} unit. This effective Hamiltonian represents the on-site interactions in the final Hartree-Fock calculation performed on a *fcc* lattice of fullerenes with nearest neighbours hopping. The resulting T_c is peaked close to 3 holes and it is strongly suppressed in the region between 4 and 6 holes. This remarkable result outlines a further analogy between hole-doped and electron-doped C_{60} molecular systems: in the alkali doped fullerides, as well, T_c as a function of electron doping presents a narrow peak between 2.5 and 4 electrons per C_{60} [44].

This interesting scenario, however, has been precluded for a long time, because of the difficulties in oxidizing C_{60}: it is much more difficult to synthesize materials in which C_{60} is present in its oxidized state, although the stability of C_{60} cations is however confirmed by cyclic voltammetry which clearly shows at least three reversible oxidation states [16]. The extremely high oxidation potentials of the fullerene molecule (1.27V for C_{60}^{+} and 1.71V for C_{60}^{2+} versus ferrocene/ferrocenium in TCE solution [16]) hampered initially the synthesis procedure: the identification of a strong oxidant appeared unavoidable [91].
C_{60} cations are chemically very reactive species, then a crystal formed byC_{60}^{n+} may not be stable. The only way to produce a fullerenium salt is to identify a particularly strong oxidant associated to a non nucleophilic counter-ion having relatively small steric hindrance such as its intercalation in the crystal lattice can occur. However, the majority of sufficiently strong oxidants, as halogens, are highly nucleophilic and yield the formation of undesired covalent compounds.

These problems could be overcome by using the conjugate base of the superacid $H(AsF_6)$ as a counter-ion, whose the large dimensions and the unitary charge prevent the nucleophilic attach on the buckyball.
$H(AsF_6)$ is a quite common superacid, as it is obtained, following a general rule on the

composition of superacids, by adding a Brønsted acid (AsF_5) to a strong Lewis acid (HF) [81]. Its oxidation activity proved however sufficiently strong to oxidize C_{60} to its dication and, in the same time, its conjugate base AsF_6^- proved also sufficiently inert and non nucleophilic to live the fullerenium ion unattached.

In the next paragraph, I remind the synthesis procedure which constitutes the central issue in the Ph.D. thesis work of Dr. Massimo Pagliari *Sintesi e Caratterizzazione di Fulleriti Cationiche* [85].

In the present work the results of XRD, NMR, SQUID magnetometry measurements will be presented, with the aim to identify the structure of the new synthesized C_{60} phase, namely the fullerenium salt $C_{60}(AsF_6)_2$, together with its electronic properties.

1.3.1 Synthesis of $C_{60}(AsF_6)_2$

The procedure identified [24,26,25] to synthesize the fullerenium salt $C_{60}(AsF_6)_2$ required the following reagents: AsF_5 as a very oxidant gas and liquid SO_2 as non-nucleophilic solvent. It is the same reaction which takes place between graphite and AsF_5 which is known to disproportionate through charge transfer following the scheme:

$$3\,AsF_5 + 2e^- \longrightarrow 2\,AsF_6^- + AsF_3 \tag{2}$$

In our case, the reaction of C_{60} with AsF_6^- was performed by suspending C_{60} in liquid SO_2 where the gaseous AsF_5 is soluble. The oxidation reaction takes place at room temperature at high pressure and follows the scheme:

$$C_{60} + 3\,AsF_5 \longrightarrow C_{60}(AsF_6)_2 + AsF_3 \uparrow \tag{3}$$

For the chemical synthesis we use a 3 stages glass reactor (fig. 13): we can operate with inert atmosphere (Ar) and vacuum and we can safely condense and transfer the reaction gas; the samples and the solid reagents are handled in a controlled atmosphere glove Box (moisture and oxygen concentration lower than 2 ppm). The glass reactor is connected with a pressure sensor which allows stoichiometric gas additions to the reaction solution. The stoichiometric amount of AsF_5 (in ratio 1:3) is condensed on the C_{60} powder in a suspension of liquefied SO_2 at 77 K.

After a 17 hours heterogeneous reaction the liquid SO_2 is thermally evaporated and neutralized in a NaOH solution. The reaction vessel temperature is stabilized and controlled with an accuracy of ~ 0.1 °C.

Figure 13: Experimental apparatus for the chemical reaction 3

Chapter 2

Experimental techniques

2.1 Nuclear Magnetic Resonance

Most elements have at least one isotope with a non-zero spin angular momentum, $\mathbf{J} = \hbar\mathbf{I}$, and an associated magnetic moment, $\boldsymbol{\mu}$, which are related by the gyromagnetic ratio

$$\boldsymbol{\mu} = \hbar\gamma\mathbf{I}\,, \tag{4}$$

$\mathbf{J}$ is a quantized characteristic of the nucleus, and its value describes the symmetry of the nuclear charge distribution. The nucleus has the properties of a magnetic dipole (essentially a bar-magnet); moreover nuclei with spin higher than 1/2 possess also a quadrupolar momentum; the most important parameters for some nuclei are shown in table 4. Spin =1/2 nuclei, for which the nuclear charge distribution is spherically symmetric, are the most often studied by NMR since they generally have both higher resolution and higher sensitivity spectra (therefore, it is relatively easier to extract chemical information from these nuclei). In an NMR experiment we are interested in exploring the interactions perturbing the Zeeman coupling between nuclear magnetic moments and an external magnetic field. The energy of this magnetic dipole-dipole interaction is given classically as,

$$E = -\boldsymbol{\mu} \cdot \mathbf{H_0}\,, \tag{5}$$

where $\mathbf{H_0}$ is the strength of the external magnetic field. The external field direction provides a coordinate system for the NMR experiment. From here on, we will work in coordinate systems where the applied magnetic field is oriented along the z-axis.

The magnetic resonance phenomenon is due to the absorption of electromagnetic energy from the nuclei: it takes place if nuclei with intrinsic magnetic moment are irradiated (in presence of a static magnetic field) with a radio-frequency field having frequency equal or very close to differences in the energy levels of the system. Thanks to the phenomenon of resonance, it is possible to observe the nuclear magnetism otherwise completely masked by

Nuclei Table

Nucleus	I	Abund. (%)	γ (rad / T s)	μ (μ_N)	Q (mbarn)	Rel. Sens.	ν (MHz)
^{1}H	1/2	99.98	$26.752 \cdot 10^{7}$	4.837	–	1.00	400.00
^{2}H	1	$1.5 \cdot 10^{-2}$	$4.107 \cdot 10^{7}$	1.213	2.86	$1.45 \cdot 10^{-6}$	61.40
^{6}Li	1	7.42	$3.937 \cdot 10^{7}$	1.163	-0.808	$6.31 \cdot 10^{-4}$	58.86
^{7}Li	3/2	92.58	$10.398 \cdot 10^{7}$	4.204	-40.1	0.27	155.45
^{10}B	3	19.58	$2.875 \cdot 10^{7}$	2.079	84.59	$3.90 \cdot 10^{-3}$	42.99
^{11}B	3/2	80.42	$8.585 \cdot 10^{7}$	3.471	40.59	0.13	128.34
^{13}C	1/2	1.108	$6.728 \cdot 10^{7}$	1.217	–	$1.76 \cdot 10^{-4}$	100.58
^{19}F	1/2	100	$25.181 \cdot 10^{7}$	4.553	–	0.834	376.36
^{23}Na	3/2	100	$7.081 \cdot 10^{7}$	2.863	104	$9.25 \cdot 10^{-2}$	105.81
^{27}Al	5/2	100	$6.976 \cdot 10^{7}$	4.309	146.6	0.21	104.23
^{39}K	3/2	93.1	$1.250 \cdot 10^{7}$	0.505	58.5	$4.73 \cdot 10^{-4}$	18.67
^{41}K	3/2	6.88	$-1.554 \cdot 10^{7}$	-1.451	-73	$5.78 \cdot 10^{-6}$	10.25
^{63}Cu	3/2	69.09	$7.112 \cdot 10^{7}$	2.875	-220	$6.43 \cdot 10^{-2}$	106.02
^{65}Cu	3/2	30.91	$7.604 \cdot 10^{7}$	3.075	-204	$3.52 \cdot 10^{-2}$	113.58
^{75}As	3/2	100	$4.596 \cdot 10^{7}$	1.858	3.14	$2.54 \cdot 10^{-2}$	68.48
^{85}Rb	5/2	72.15	$2.593 \cdot 10^{7}$	1.601	276	$7.57 \cdot 10^{-3}$	38.62
^{87}Rb	3/2	27.85	$8.786 \cdot 10^{7}$	3.553	133.5	$4.87 \cdot 10^{-2}$	130.89
^{133}Cs	7/2	100	$3.533 \cdot 10^{7}$	2.928	-3.43	$4.74 \cdot 10^{-2}$	52.47

Table 4: The most important parameters for some nuclei: the spin angular momentum I, the natural abundance, the gyromagnetic factor γ, the nuclear magnetic moment, the nuclear quadrupole moment, the NMR relative sensitivity with respect to the ^{1}H nucleus (obtained by multiplying the absolute sensitivity for a constant number of nuclei by the natural abundance) and the NMR reference frequency in a 400 MHz magnet (9.3950 T).

the electron paramagnetism and diamagnetism, more intense than the former of at least 3 orders of magnitude ($\mu_N/\mu_B \sim 10^{-3}$). The Nuclear Magnetic Resonance (NMR) technique provides information not only on nuclei, but also on the electronic and lattice dynamics.

It is based on the fact that the response to electromagnetic energy absorption from NMR active nuclei may provide information on various electronic properties of the sample. The quantistic description of the resonance phenomenon refers to the transitions between nuclear spin energy levels. A semi-classic treatment, however, is a simplified approach which is more useful in the different experimental applications of NMR. In this case a generic spin **S** in presence of a magnetic field $\mathbf{H_0}$ oriented along the **z** direction, begins to precess around the field direction with a characteristic frequency $\omega_0 = \gamma H_0$. Using a coil placed in the x-y plane, with an alternating potential difference having frequency equal to ω_0 a linearly polarized magnetic field will be generated. This field can be considered like the superposition of two different oscillating fields with circular polarization but rotating in the opposite direction. Considering only the rotating component $\mathbf{H_1}$ following the precession of $\mathbf{S}$, it results in a reorientation of the magnetic moment whose angular quantification depends on the exchanged energy with the magnetic system. The phenomenon can be suitably described in a rotating reference frame with frequency ω_0: in this case the magnetic field $\mathbf{H_1}$ results static, and $\mathbf{H_0}$ is absent: its effect (the rotation) is already accounted for by the non-inertial rotating frame. The application of $\mathbf{H_1}$ induces a spin rotation according to the law $\omega_1 = \gamma H_1$. The signal detection is performed on the same induction coil used for the irradiation. To get the maximum signal from the spin magnetic moment it should be detected when the spin lies in the x-y plane. This situation corresponds to a rotation of $\pi/2$ (or $(k+1/2)\pi$) around the field $\mathbf{H_1}$ and it takes place irradiating with a RF pulse, whose duration turns out to be $\tau = \frac{\pi}{2\gamma H_1}$.

This qualitative description does not take into account factors which in real systems yield the damping of the induced voltage. Since the detected macroscopic signal arises from the summation of all the contributions from different spins, it decays because of the spin decoherence coming from field inhomogeneity or from the strong coupling with the electronic and lattice dynamics. Such irreversible phenomena are accounted for with the relaxation times spin-spin and spin-lattice, which will be described later.

The signal induced in the sample coil is commonly called FID (Free Induction Decay) and it presents, in the simplest case, an exponential shape: its Fourier transform is consequently a Lorentzian function:

$$L(\omega) = \frac{1}{\pi} \frac{\frac{1}{2}\Gamma}{(\omega - \omega_0)^2 + \left(\frac{1}{2}\Gamma\right)^2} \ , \tag{6}$$

where Γ is the full width at half maximum (FWHM).

2.1.1 Semi classic description

The application of the second cardinal equation of dynamics to a classical particle with intrinsic magnetic moment $\boldsymbol{\mu} = \gamma \mathbf{J}$ in presence of a static magnetic field $\mathbf{H_0}$ conventionally oriented long $\mathbf{z}$, yields to the precession equation (with frequency $\omega_0 = \gamma H_0$)

$$\frac{d\mathbf{J}}{dt} = \boldsymbol{\mu} \times \mathbf{H_0} \qquad \longrightarrow \qquad \frac{d\boldsymbol{\mu}}{dt} = \gamma \boldsymbol{\mu} \times \mathbf{H_0} \qquad \longrightarrow \qquad \frac{d\boldsymbol{\mu}}{dt} = -\gamma \mathbf{H_0} \times \boldsymbol{\mu} \ . \tag{7}$$

The $\boldsymbol{\mu}$ component perpendicular to $\mathbf{z}$ rotates round $\mathbf{H_0}$ with frequency ω_0; moreover the angle between $\boldsymbol{\mu}$ and the $\mathbf{z}$ axis remains fixed until an energy exchange with the external environment takes place (see figure 14).

If we turn on a variable magnetic field $\mathbf{H_1}$ with circular polarization in the x-y plane:

$$\mathbf{H_1}(t) = H_1 \cos\omega t\, \mathbf{i} - H_1 \sin\omega t\, \mathbf{j} \ , \tag{8}$$

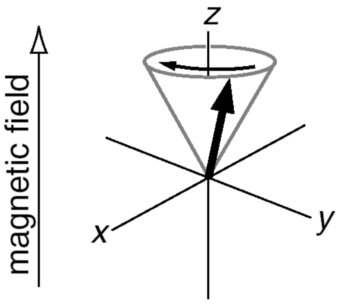

Figure 14: magnetic moment $\boldsymbol{\mu}$ precession around the $\mathbf{z}$ axis

the description in the rotating frame with $\mathbf{H_1}$(t) must account for the term $\boldsymbol{\omega} \times \boldsymbol{\mu}$ [41]; as a result the motion equations will be modified as following

$$\left(\frac{d\boldsymbol{\mu}}{dt}\right)_S = \left(\frac{d\boldsymbol{\mu}}{dt}\right)_{S'} + \boldsymbol{\omega} \times \boldsymbol{\mu} \ , \tag{9}$$

where $(\ )_S$ means the representation of a generic physical quantity in the inertial reference frame, and with $(\ )_{S'}$ the representation of the same one in the rotating frame. Considering also the presence of $\mathbf{H_1}(t)$ and considering the relation (9), the equation (7) becomes:

$$\left(\frac{d\boldsymbol{\mu}}{dt}\right)_{S'} = \boldsymbol{\mu} \times (\gamma \mathbf{H} + \boldsymbol{\omega}) = \boldsymbol{\mu} \times \left[H_1 \cos\omega t\, \mathbf{i} - H_1 \sin\omega t\, \mathbf{j} + \left(H_0 - \frac{\omega}{\gamma}\right)\mathbf{k}\right] \tag{10}$$

Choosing S' so that versor $\mathbf{i}'$ is oriented like $\mathbf{H_1}$(t), the effective field present in the rotating frame results:

$$\mathbf{H}_{eff} = H_1\,\mathbf{i}' + \left(H_0 - \frac{\omega}{\gamma}\right)\mathbf{k} \ . \tag{11}$$

Depending on the value of ω, $\mathbf{H}_{eff}$ would be perpendicular or parallel to $\mathbf{z}$. In off-resonance conditions its value will be dominated from H_0. In resonance conditions ($\omega = \omega_0$) then the motion of the magnetic moment in S' can be described as a simple precession around the $\mathbf{x}'$

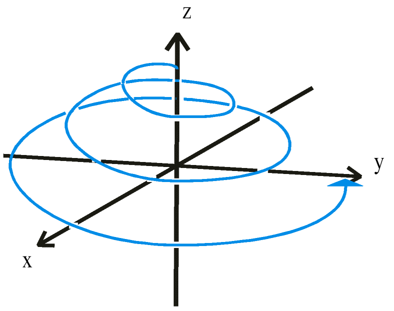

Figure 15: complex path of the magnetic moment $\boldsymbol{\mu}$, in the laboratory reference frame: it arises from the composition of the precession around $\mathbf{z}$ and of the much slower one around the rotating $\mathbf{x}'$ axis.

axis, while in the inertial frame S the spin path is much more complex: the motion results from the composition of two precessions (see figure 15).

This is the reason why the angle θ between $\boldsymbol{\mu}$ and the $\mathbf{z}$ axis changes continuously; moreover, because of equation 5, there is a continuous energy transfer between the spin and the external environment, through the radio-frequency field $\mathbf{H_1}$.

2.1.2 Quantistic description

The well known Zeeman Hamiltonian which takes into account the interaction between a nucleus with intrinsic magnetic moment $\boldsymbol{\mu} = \gamma \mathbf{J} = \gamma \hbar \mathbf{I}$ and the external magnetic field $\mathbf{H}_0$, can be written as in the following:

$$\mathcal{H} = -\boldsymbol{\mu} \cdot \mathbf{H_0} = -\gamma \hbar H_0 I_z \ , \tag{12}$$

where the $2I + 1$ eigenvalues are:

$$E_m = -\gamma \hbar H_0 m \qquad m = -I, ..., I \ . \tag{13}$$

The radio-frequency field $\mathbf{H_1}$ introduced in a typical NMR experiment represents a small perturbation of the system energy levels, but, in resonance conditions, this perturbation promotes transitions between the levels, because the Zeeman eigenstates are no more real eigenstates for the perturbed system. The presence of other interactions can be treated similarly with a perturbative approach. Considering the evolution of a generic spin system under the total perturbed Hamiltonian, the following effects are expected:

1. shifts in the energy levels induced by the perturbative terms which commute with the Zeeman Hamiltonian;
2. contributions to the transitions between the energy levels: this is eventually an extra contribution to the relaxation dynamics coming from the non-commutative terms of the perturbations.

The spin system evolution after the application of the RF pulse can be described with the density matrix formalism [32,33]. The density operator at equilibrium is given by the formula:

$$\sigma_{eq} = \frac{1}{Z}\, e^{-h\,\mathcal{H}/kT} \ , \tag{14}$$

where Z is the partition function.

It changes in time according to the Liouville-Von Newmann equation:

$$i\, \frac{d\sigma(t)}{dt} = [\,\mathcal{H}\,, \sigma(t)\,] \ , \tag{15}$$

where $\mathcal{H}$ is the acting Hamiltonian. It is easy to verify that the solution to this equation under a time independent Hamiltonian is:

$$\sigma(t) = e^{-i\mathcal{H}t}\sigma(0)\, e^{i\mathcal{H}t}\ . \tag{16}$$

Here t is the time during which the Hamiltonian has acted on the spin system, $\sigma(0)$ represents the initial state of the system and $\sigma(t)$ the final state. It is usually convenient to rewrite this in term of the propagator $U(t,0) = e^{-i\mathcal{H}t}$.

$$\sigma(t) = U(t,0)\,\sigma(0)\,U(t,0)^{\dagger}\ . \tag{17}$$

The time evolution of the density operator for a typical NMR experiment is therefore represented by the eq. 17, with initial condition:

$$\sigma(0) = \sigma_{eq}\ . \tag{18}$$

The quantistic observable whose temporal evolution can be related directly to the free induction signal is the expectation value of the operator I_x (or I_y) which changes in time following the equation

$$\langle I_x \rangle = Tr\{I_x\,\sigma(t)\}\ . \tag{19}$$

It is very common to use also $I_+ = I_x + i\,I_y$ in NMR simulations, even if it does not represent a quantistic observable; this only determines a different intensity factor in the spectra.

2.1.3 NMR in macroscopic systems

The generalization of the precession equation to real systems can be performed only introducing parameters related to the relaxation phenomena. Even considering the semi-classic approach, for a more intuitive description, the generalization of the precession equation for the single spin to a macroscopic system with volume magnetization $\mathbf{M}$ is not straightforward, as we can see from

$$\frac{1}{2}\frac{dM^2}{dt} = \mathbf{M}\cdot\left(\frac{d\mathbf{M}}{dt}\right) = \mathbf{M}\cdot\mathbf{M}\times\gamma\mathbf{H} = 0 \tag{20}$$

where the scalar multiplication with $\mathbf{M}$ yields the inconsistent conclusion that the absolute value of $\mathbf{M}$ could not change. We know that in real systems the difference in the energy levels population, due to the presence of a static magnetic field, results in the net magnetization

$$M = N\gamma\hbar\,\frac{\displaystyle\sum_{m=-I}^{I} m\, e^{\frac{\gamma\hbar m H_0}{kT}}}{\displaystyle\sum_{m=-I}^{I} e^{\frac{\gamma\hbar m H_0}{kT}}} \tag{21}$$

where N is the total number of magnetic moments, and $E_m \propto e^{-\frac{E_m}{kT}}$ the level m energy for the single spin.
In 1946 [11] F. Bloch proposed a vector model and a set of phenomenological equations suitable for the description of the relaxation phenomena in the field of high resolution NMR.

$$\begin{aligned}
\frac{dM_z}{dt} &= -\gamma(\mathbf{H_0} \times \mathbf{M})_z + \frac{M_0 - M_z}{T_1} \ , \\
\frac{dM_x}{dt} &= -\gamma(\mathbf{H_0} \times \mathbf{M})_x - \frac{M_x}{T_2} \ , \\
\frac{dM_y}{dt} &= -\gamma(\mathbf{H_0} \times \mathbf{M})_y - \frac{M_y}{T_2} \ .
\end{aligned} \tag{22}$$

Here T_1 and T_2 represent the relaxation time constants of the spin-lattice and spin-spin processes, which will be described in more detail in the next section. Instead of considering individual spins obeying the laws of quantum mechanics, Bloch showed that it is sufficient to focus the attention on the net macroscopic nuclear magnetization obtained by taking the ensemble average over all the spins. This macroscopic magnetization obeys the laws of classical mechanics in its interaction with the applied static and radio frequency fields, while the effects of spin-spin and spin lattice-relaxation may be accounted for phenomenologically by the introduction of simple damping terms in the Bloch equations. In high resolution NMR spectroscopy it is often possible to generalize this picture to systems with many different chemical shifts and spin-spin couplings: in this case each individual resonance in the high resolution spectrum is represented by a vector M with its characteristic intensity and precession frequency. Difficulties in this pictorial model arise in more complicated NMR experiments where multiple pulse sequences are used. It is worth while noticing that this model breaks down in solid state NMR where the interactions on the nuclear spins cannot be treated separately.

2.1.4 Relaxation

The relaxation phenomena provide information on the molecular and structure dynamics; moreover, in case of the spin-lattice relaxation, it limits how rapidly NMR spectra will be acquired. Before describing in more detail the two type of relaxation mechanisms (spin-lattice and spin-spin relaxation) it is useful to describe briefly how a modern pulsed NMR experiment is performed.

The sample is placed inside the inductive coil of a particular RLC circuit (namely the NMR probe), equipped with a variable capacitor for tuning the resonance frequency. A variable inductance is also necessary for a proper impedance matching with the other electronic components (amplifier, preamplifier etc.). The sample coil is oriented in a plane perpendicular to the z axis; the induced magnetic field is therefore perpendicular to the external field H_z. In resonance conditions the excitation can “flip” the magnetization originally oriented along the direction of the external field. The RF excitation sequence is a complicated set of pulses and delays depending on the type of experiment performed, but also on the relaxation properties of the material.

2.1.4.1 Spin-lattice relaxation

The spin-lattice relaxation is determined by all the possible energy exchange mechanisms between the nuclei and their electronic surroundings; "lattice" here is used as a general term for nuclear environment. The electrons with the lattice, indeed, represent a virtually infinite energy source for the nuclear spins, whose magnetic energy scale is three orders of magnitude lower than the electronic magnetism scale.

With the aim to better understand the origin of this relaxation process, let's consider the following ideal experiment: suppose it were possible to drop the NMR sample into the probe instantaneously and then to apply the excitation pulse immediately. Moreover imagine to perform this experiment without the intense external field. In this *ideal* experiment we would not observe any NMR signal. The nuclear polarization would be negligibly small in such an experiment because the nuclei are only polarized by the very weak Earth field, giving a negligible population difference between the upper and the lower energy levels. With a more intense static field, properly oriented, this experiment would, in principle, work; however when the field is suddenly changed to the intense field B_z the building up of the proper Boltzmann population distribution can be quite slow, depending on the different interactions present in the material. Initially the nuclear spins are "hot", and they cool down transferring the magnetic energy to their surroundings: this process is the spin-lattice relaxation. Obviously it is possible only if there are some energy exchange mechanisms: in an ideal sample with no interaction between lattice (in its general meaning) and nuclei, the nuclear magnetization could not relax to its saturation value. This is an extreme situation which doesn't take place in real systems, although it is quite common, mainly in solid state NMR, to perform experiments on materials with very slow relaxation dynamics (characterized by recovery times of the order of minutes or more). These situations arise from the different weights between the NMR interactions present in the sample. The principal contributions, in the solid state, come from:

- direct dipolar interaction,
- quadrupolar interaction (for spin $S > 1/2$ nuclei),
- Chemical shift anisotropy
- Knight shift

Moreover, it is worth noticing that all the anisotropic part of these interactions are averaged to zero in liquid samples, due to the fast tumbling of the molecules. In high resolution NMR, therefore, the principal contribution to the spectrum arise only from:

- isotropic Chemical shift
- j-coupling (indirect dipolar interaction).

These NMR interactions will be described in the next sections.

In summary, the variation of the population difference as a function of time is described by an exponential curve, starting from zero and raising asymptotically toward the Boltzmann equilibrium conditions. Any deviation of the longitudinal magnetization $\mathbf{M_z}$ from the equilibrium value $\mathbf{M_0}$ is followed by an exponential recovery according to the equation:

$$(M_z - M_0)_t = (M_z - M_0)_0 \left(e^{-\frac{\tau}{T_1}} \right) \ , \tag{23}$$

where T_1 is the time constant of the relaxation process, namely the "spin-lattice relaxation time" and $(...)_t$ represents the considered physical quantity at the time t. This time constant is also referred to as "longitudinal relaxation time" in comparison to the "transverse relaxation time" T_2 relative to the spin-spin relaxation process. The equation 23 is simply derived from the Bloch equations 22 written in the rotating frame in absence of any RF field. Moreover starting from the equation 23, and respectively considering $(M_z - M_0)_0 = -M_0$ or $(M_z - M_0)_0 = -2\ M_0$, it is easy to obtain the magnetization behaviour for the specific NMR experiments commonly used to evaluate the time constant T_1: *inversion recovery* and *saturation recovery.*

2.1.4.2 Spin-spin relaxation

This process concerns the decaying of the transverse magnetization (obtained after a $\pi/2$ pulse which drops the longitudinal magnetization in the x-y plane) and is indirectly related to the NMR line width. Roughly speaking the faster is the transverse relaxation the more rapid the decay of the free induction signal will be, yielding a broad lineshape in the Fourier space. Every interaction mechanism which contributes to increase the spin decoherence will be responsible for such a relaxation process, therefore all the mechanisms of spin-lattice relaxation should also be considered mechanism of spin-spin relaxation. However, the time constant T_2 is usually much lower that T_1.

In analogy with the longitudinal relaxation, the transverse magnetization recovery follows an exponential function:

$$M_{xy} = M_0\ e^{-\frac{t}{T_2}} \ . \tag{24}$$

The extraction of the time constant T_2 from the NMR data is, however, not straightforward: it is not directly deducible from the width of the experimental lineshape. The quantity directly related to the linewidth, namely, the effective time constant T_2^*, is correlated to the intrinsic relaxation T_2 through the equation:

$$\frac{1}{T_2^*} = \frac{1}{2T_1} + \frac{1}{T_2} + \gamma \Delta H \ , \tag{25}$$

where $\frac{1}{2\,T_1}$ represent the Heisenberg broadening of the NMR lines (usually negligible in comparison with the other terms), and $\gamma\Delta H$ is the contribution to the spin decoherence due to field inhomogeneity.

The spin dephasing originated from the latter term, due to its phenomenological nature, can be recovered performing an appropriate echo sequence: the Hahn echo [49].

2.1.5 NMR echoes

One of the most intriguing features of the NMR technique is the possibility to perform experiments using pulse sequences which induce the formation of “spin echo” signals. The echoes phenomena may be described properly only from a quantistic point of view and represent a useful tool for the experimentalist in measurements where the strong correlation nature of the interactions within the sample yields an extremely fast decay of the free induction signal (decay times close to few microseconds represent the technological limit for the spectrometer electronics).

Thanks to the echoes phenomena, these signals, otherwise completely lost, can be retrieved in a two-pulse experiment [49]. After the initial free induction signal has disappeared, a second pulse at time τ induces a new response which refocuses at time 2τ. Hahn’s experiment used a couple of $\pi/2$ pulses but the picture results much more intuitive considering the description of a typical $\pi/2 - \pi$ experiment. This sequence removes the effect of the field inhomogeneity over the spin motion; moreover it is successful also in completely refocusing heteronuclear dipolar interactions.

Consider a simplified case where the spin dephasing can be represented only with “isochromat” vectors f and s relative to spins groups precessing respectively (in the rotating reference frame) at higher frequency ($fast$), and lower frequency ($slow$). These vectors are aligned along the **+y** axis by the first $\pi/2$ pulse (see figure 16) and after a time τ a relative dephasing takes place in the **xy** plane. The following π pulse, about the **+x** axis, turns these vectors into mirror image positions with respect to the **+x** axis; so arranged, with the fast spin vector behind the slow vector, all them move into coincidence along the **-y** axis after a further period τ of free precession.

Moreover if the echo peak amplitude is monitored as a function of 2τ in a series of experiments, it is observed to decay with a time constant T_2 which may be much longer than

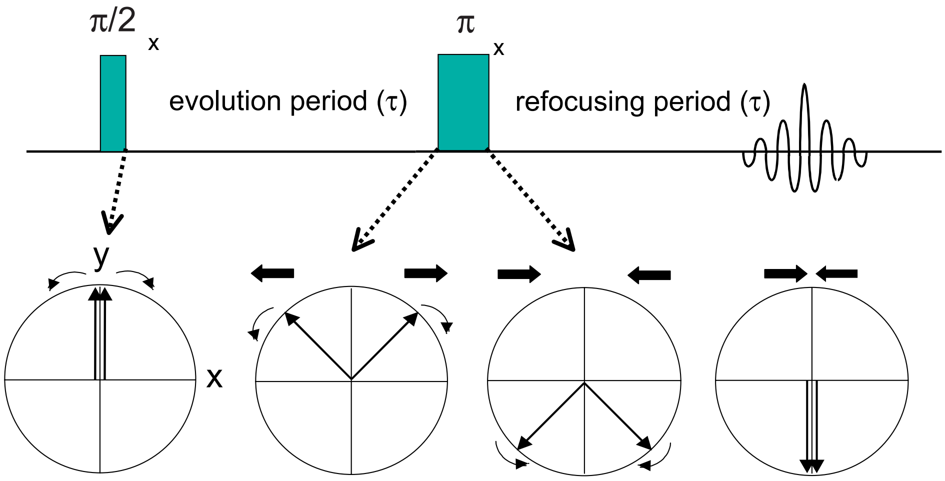

Figure 16: spin echo experiment: the first pulse bends the spins (initially oriented in the **z** direction) in the plane xy. During the delay (the evolution period) between the first and the second pulse the dephasing takes place, but it is recovered after the refocusing period.

T_2^*, as discussed in section 2.1.4.2. This is principally due to the inhomogeneity contribution (see eq. 25). In such a way the spin echo experiment provides the most direct method of measuring spin-spin relaxation times in situations where the natural linewidths are obscured by field inhomogeneity broadening. A typical spin echo train is shown in figure 17.

In summary we can assert that for a group of spins this ordinary echo sequence ($\frac{\pi}{2}\,_x \ldots \tau \ldots \pi\,_x$) refocuses the dephasing which arises from the field inhomogeneity.
Since the magnetic dipolar coupling among neighbour spins is in some way analogous to a field inhomogeneity, it is expected that the same sequence would also refocus the dephasing resulting from magnetic dipolar coupling. This analogy is valid, however, only if the dipolar

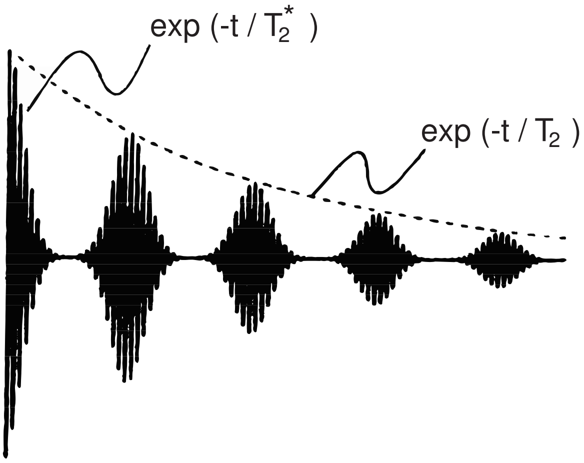

Figure 17: Simulation of a spin echo train showing the rapid signal decay due to field inhomogeneity (T_2^*) and the slower decay of the echo envelope due to intrinsic spin-spin relaxation (T_2).

coupling is between different nuclear species (*e.g.*, ^{19}F and ^{13}C): in this case the ordinary spin echo does refocus the dipolar coupling, otherwise, in the case of like nuclei (*e.g.*, ^{1}H and ^{1}H), such an echo does not work properly.

This fact arises because the π_x refocusing pulse (in case of homonuclear spins) flips both coupled spins I leaving the coupling term $I_{1z} I_{2z}$ unchanged. The inversion of both coupled spins is the key to understand this phenomenon, which can be described starting from the analysis of the heteronuclear coupling.

Consider the heteronuclear coupled spin I and S: the spin I resonance is made of two lines corresponding to the α and β states of S and may be represented with the same vector diagram reported in figure 16. The vector relative to the transition with higher frequency can be referred to as f (faster precessing) and the other one as s (slower precessing). As discussed previously the first pulse aligns both vectors along $+\mathbf{y}$ axis, then during the free precession interval a relative phase difference builds up. At this point the π_x pulse rotates f and s in their mirror-image positions with respect the $\mathbf{x}$-axis.
Had this been the only effect, f and s would come to an exact focus at the time 2τ, in strict analogy with the case of field inhomogeneity broadening: this is exactly what happens for heteronuclear coupled spins, as previously asserted. However if spins I and S are homonuclear, the π_x pulse determines another distinct effect: it also flips the spin S, interchanging the α and β spin states and thus interchanging the labels f and s. This means that the vector f, faster in the first τ interval, becomes slower in the second τ interval yielding an increasing of the divergence, which does not therefore cancel.

Nevertheless, Powles and Mansfield [89] discovered that the homonuclear dipolar coupling could be refocused by applying a pair of $\frac{\pi}{2}$ pulses shifted in phase of 90° with respect to each other. Such a sequence has been referred to as “solid echo” or “dipolar echo”.
Powles and Mansfield provided a theoretical demonstration that this sequence refocuses perfectly spins $\frac{1}{2}$ nuclei interacting only in pairs and they showed it experimentally for $CaSO_4{\cdot}2H_2O$. However it does not refocuses larger groupings of spins perfectly [99].
Within this PhD. work, molecular systems characterized by the presence of homonuclear dipolar coupling between groupings of 6 spin 1/2 have been probed with solid state NMR. ^{19}F NMR measurements performed with solid echo sequences will be shown in the Results section.

2.1.6 Nuclear interactions probed with NMR

In this section the principal interaction channels between nuclei and electrons which can give a contribution to the NMR lineshape will be considered in more detail. The description will be principally devoted to the interactions relevant in solid state NMR experiments, where the presence of broad lineshapes may provide a wealth of information on the dynamics. The NMR study of the molecular dynamics vs. temperature is, for instance, a very useful tool (which can be considered complementary to X-Ray diffraction) in the structural characterization of new materials. Structural phase transitions in C_{60} have been discovered with this technique [10, 53, 104].

2.1.6.1 Zeeman interaction

Consider the magnetic moment $\boldsymbol{\mu}$ in presence of an external field $\mathbf{H_0}$, its unperturbed Hamiltonian is:

$$\mathcal{H}_Z = -\gamma\hbar\,\mathbf{H_0}\,\mathbf{I}. \tag{26}$$

If the radio-frequency field is turned on, the effect of such perturbation can be accounted with the Hamiltonian:

$$\mathcal{H}_1 = -\frac{1}{2}\gamma\hbar H_1\left(I_+e^{-i\omega t} - I_-e^{i\omega t}\right). \tag{27}$$

Due to the properties of $I_\pm$, $\mathcal{H}_1$ elements are non-zero only for the I_z eigenstates $|m\rangle$ and $|m'\rangle$ where $m' = m + 1$. For this reason transitions will arise only if $\Delta E = \gamma\hbar H_0 = \hbar\omega_0$.
In strong field conditions this perturbative approach can be extended also to the other perturbing interactions as previously discussed (see 2.1.2).

2.1.6.2 Chemical shift

This interaction arises from the screening effect of the valence electrons with respect to the external magnetic field. Consequently the effective field at the nuclear site results lower than the applied field: this yields a shift of the resonance frequency but also, due to the anisotropic nature of the interaction, a broadening of the NMR line. Depending on the local symmetry at the nuclear site, the magnitude of the chemical shift will vary as a function of the orientation of the molecule with respect to the external magnetic field. This orientation dependence of the chemical shift is referred to as chemical shift anisotropy (CSA).
Mathematically, the chemical shift is described by a second-rank tensor (a 3 by 3 matrix), where the tensor trace, representing the isotropic part of the interaction, is directly related to the shift in frequency of the resonance line. The Chemical shift Hamiltonian is therefore:

$$\mathcal{H}^{CS} = \sum_{k=1}^{N}\gamma_k\mathbf{I}_k\cdot\sigma_k\cdot\mathbf{H}_0\,, \tag{28}$$

where σ_k represents the chemical shielding tensor which can be written in the principal axis system assuming, thus, the form:

$$\sigma_{\mathbf{k}}^{\mathbf{PAS}} = \begin{pmatrix} \sigma_{11}^k & 0 & 0 \\ 0 & \sigma_{22}^k & 0 \\ 0 & 0 & \sigma_{33}^k \end{pmatrix}. \tag{29}$$

Other quantities are usually defined to obtain a more direct physical interpretation of the tensorial features: *isotropic chemical shift* σ_{iso}, the *anisotropic chemical shift* σ_{aniso} and the *asymmetry* of the chemical shift η_{CS}:

$$\sigma_{\text{iso}} = \frac{1}{3}Tr\{\sigma\} = \frac{\sigma_{11}+\sigma_{22}+\sigma_{33}}{3}, \ \sigma_{aniso} = \sigma_{33} - \sigma_{\text{iso}}, \ \eta_{CS} = \frac{|\sigma_{11}-\sigma_{22}|}{\sigma_{33}-\sigma_{\text{iso}}} \tag{30}$$

The absolute value of σ_{iso} represents the shift in the resonance line position with respect to a standard reference compound. For the ^{13}C nucleus the reference is tetramethyl silane (TMS), which has been chosen since it yields the most shielded ^{13}C spectrum known. For ^{19}F a widely used reference is CFCl$_3$, but, for experimental reasons in our ^{19}F NMR measurements we used C$_6$F$_6$ as a reference compound. Having the $\sigma_{\mathbf{k}}^{\mathbf{PAS}}$ tensor non zero trace, the chemical shift represents, together with the scalar coupling (see paragraph 2.1.6.5), the most important NMR interaction probed in high resolution NMR experiments. Indeed, in liquid samples, where the fast tumbling of molecules averages the anisotropy to zero, NMR spectra are formed by sharp lines whose position in frequency is directly correlated to the molecular species present in the samples.

2.1.6.3 Knight shift

The mathematical description of such an interaction is analogous to the one of Chemical shift: both are anisotropic effects induced from the hyperfine interaction between nuclei and electrons; however the physical mechanism originating the Knight shift is completely different from the one previously discussed. First of all the Knight shift describes the interaction between the nuclei and the electrons in the conduction band. The polarization of conduction electrons, induced by the external field, determines an extra field at the nucleus site; thus, the local effective field results increased. This effect is comparable with the Chemical shift and it represents a hallmark of the metallic state. The Knight shift interaction reflects the crystallographic symmetries because of its non-localized nature. Considering that the isotropic contribution of such an interaction arises from the well known Fermi contact Hamiltonian,

$$\mathcal{H} = \frac{8\pi}{3}\gamma_e\gamma_n\hbar^2\mathbf{I}\cdot\mathbf{S}\,\delta(\mathbf{r})\,, \tag{31}$$

where $\delta(r)$ is the delta function and the electron as well the nuclear magnetic moments are respectively $\boldsymbol{\mu}_e = -\gamma_e\hbar\mathbf{S}$, $\boldsymbol{\mu}_n = -\gamma_n\hbar\mathbf{I}$. This implies the presence of s-like electronic states, coupled with nuclear spins, which is not the case of fullerides. In alkali metals the conduction band is s-like, yielding a consistent isotropic contribution to the Knight shift; however it is important to notice that in fullerides, due to the p-like nature of the conduction band, originated from the t_{1u} orbital, the Knight shift is expected to be strongly anisotropic with K_{aniso} much more relevant than K_{iso}. These quantities can be defined in strict analogy with

$\sigma_{\text{iso}}, \sigma_{aniso}$, and η_{CS}:

$$K_{\text{iso}} = \frac{1}{3}Tr\{\mathbf{K}\} = \frac{K_{11}+K_{22}+K_{33}}{3},\ K_{aniso} = K_{33} - K_{\text{iso}},\ \eta_K = \frac{|K_{11}-K_{22}|}{K_{33}-K_{\text{iso}}}, \tag{32}$$

where $\mathbf{K}$ is the Knight shift tensor:

$$\mathbf{K}_{\mathbf{k}}^{\mathbf{PAS}} = \begin{pmatrix} K_{11}^k & 0 & 0 \\ 0 & K_{22}^k & 0 \\ 0 & 0 & K_{33}^k \end{pmatrix} \tag{33}$$

2.1.6.4 Dipolar interaction

The direct interaction of a nuclear spin with the magnetic field generated by the other surrounding nuclei can be roughly estimated considering as a local field:

$$H_{loc} = \frac{\mu}{r^3}\ . \tag{34}$$

If $r = 2$ Å and $\mu = 10^{-3}\mu_N$, H_{loc} results ~ 1 Gauss.
Depending on the nuclear distance, the contribution of this term to an NMR spectrum can be very significant yielding characteristic features in the lineshape, as it will be shown for a few simple spin systems whose dipolar spectra have been simulated during this Ph.D. work (see paragraph 3.1.5).
The rigorous dipolar Hamiltonian is reported here:

$$\mathcal{H}_{dip} = -\sum_{k,j}\mu_k\mathbf{H}_{k,j} = \frac{1}{2}\sum_{k,j}\left[\frac{\mu_j\cdot\mu_k}{r_{k,j}^3} - 3\frac{(\mu_j\cdot\mathbf{r}_{k,j})(\mu_k\cdot\mathbf{r}_{k,j})}{r_{k,j}^5}\right]. \tag{35}$$

By writing the two magnetic moments μ_k, μ_j in component form, one obtains:

$$\mathcal{H}_{dip} = \sum_{k<j}\frac{\gamma_k\gamma_j\hbar^2}{r_{kj}^3}\left[\mathbf{I}_k\cdot\mathbf{I}_j - \frac{3}{r_{kj}^2}(\mathbf{I}_k\cdot\mathbf{r}_{k,j})(\mathbf{I}_j\cdot\mathbf{r}_{k,j})\right]. \tag{36}$$

Considering a single spin pair, I_1 and I_2, if we express I_{1x} and I_{1y} in terms of the raising and lowering operators I_{1+}, I_{1-}, respectively, and express the Cartesian coordinates in terms of the spherical coordinates, the dipolar Hamiltonian assumes, thus, a particularly convenient from for computing matrix elements (namely the dipolar alphabet):

$$\mathcal{H}_{dip} = \frac{\gamma_1\gamma_2\hbar^2}{r^3}(A+B+C+D+E+F)\,, \tag{37}$$

where

$$\begin{aligned}
A &= I_{1z}I_{2z}(1-3\cos^2\theta)\\
B &= -\frac{1}{4}(I_{1+}I_{2-}+I_{1-}I_{2+})(1-3\cos^2\theta)\\
C &= -\frac{3}{2}(I_{1+}I_{2z}+I_{1z}I_{2+})\sin\theta\,\cos\theta\,e^{-i\phi}\\
D &= -\frac{3}{2}(I_{1-}I_{2z}+I_{1z}I_{2-})\sin\theta\,\cos\theta\,e^{i\phi}\\
E &= -\frac{3}{4}I_{1+}I_{2+}\sin^2\theta\,e^{-2i\phi}\\
F &= -\frac{3}{4}I_{1-}I_{2-}\sin^2\theta\,e^{2i\phi}
\end{aligned} \tag{38}$$

The term A is the only one commutative term of the dipolar Hamiltonian (B also in case of homonuclear spin pair); the other terms contribute to the transitions between the Zeeman levels. Usually, in solid state NMR spectra, only the contribution of the commutative terms is accounted for since they are directly responsible for the dipolar lineshape. The other terms can be neglected in a first order approach. The commutative terms are usually referred to as the scalar part of dipolar Hamiltonian. The typical powder spectrum of a single coupled spin pair is shown in figure 18.

This characteristic lineshape has been probed experimentally by Pake [86] in static NMR measurements. The dipolar Hamiltonian can be represented in a more compact form through the tensor formalism:

$$\mathcal{H}_{dip} = \sum_{i\neq j} \mathbf{I_i}\cdot\widehat{\mathbf{D}}\cdot\mathbf{I_j}\ . \tag{39}$$

where $\widehat{D}$ is a rank 2 traceless tensor. The dipolar interaction, indeed, does not contribute to NMR spectra in the case of isotropic rotation of molecules, as well as for many plastic crystals like fullerides, at room temperature. The same conclusion is valid for high resolution NMR spectra: having the interaction tensor zero trace, there is no possibility to observe the dipolar lineshape.

Even in static NMR experiments (performed at low temperature in solid state samples to block the residual molecular motion) the dipolar spectra presents such characteristic features only if in the sample there are groupings of interacting spins which can be treated separately, thus neglecting the dipolar contribution between different groups. The simplest case is the spin pair (figure 18). If the crystal structure of the sample does not satisfy this condition, in principle, each nuclear dipolar field must be accounted, yielding a Gaussian broadening of the NMR spectrum, as described by the well-known *method of moments*.

This mathematical analysis describes the calculation of the moments relative to the Gaussian distribution representing the broadened NMR spectrum; the most significant one, directly

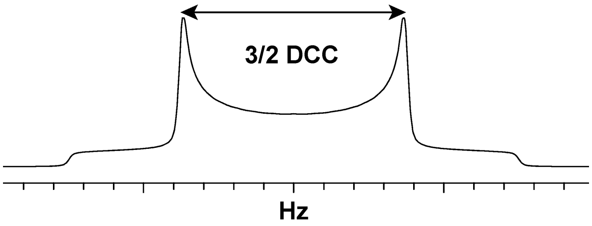

Figure 18: Pake doublet for a homonuclear spin 1/2 pair, where DCC is the dipolar coupling constant, DCC= $\mu_0\gamma_i\gamma_j\hbar/4\pi\langle r^3\rangle$. It was first observed in the ^{1}H NMR spectrum of solid $CaSO_4\cdot H_2O$. The Pake doublet is composed of two subspectra resulting from the α and β spin states of the coupled nucleus.

related to the *half width at half maximum* δ, is the second moment M_2. For heteronuclear coupled spins, it has been calculated through the Van Vleck formula [107]:

$$M_{2\,I\leftarrow S} = \frac{1}{3}\gamma_I^2\gamma_S^2\hbar^2 S(S+1)\frac{1}{N}\sum_{j,k}\frac{(1-3\cos^2\theta_{j,k})^2}{r_{j,k}^6}, \tag{40}$$

which, in the case of homonuclear coupling, becomes

$$M_{2\,homonuclear} = \frac{3}{4}\gamma^4\hbar^2 I(I+1)\frac{1}{N}\sum_{j,k}\frac{(1-3\cos^2\theta_{j,k})^2}{r_{j,k}^6}. \tag{41}$$

The second moment $M_2 = \Delta^2$ of a normalized Gaussian function,

$$f(\omega) = \frac{1}{\Delta\sqrt{2\pi}}\,e^{\left(\frac{-(\omega-\omega_0)^2}{2\Delta^2}\right)}, \tag{42}$$

is related to δ through the formula:

$$\delta = \Delta\sqrt{2\log 2} \sim 1.18\Delta. \tag{43}$$

Thus, the second moment, calculated through the reported relations, can be easily compared with the experimental width of the NMR spectrum. In static conditions, the equations 40 and 41 can be further simplified: performing the powder average of the term $(1-3\cos^2\theta_{j,k})^2$ (assuming the powder sample made of crystallites of random orientations), one obtains:

$$M_{2\,I\leftarrow S} = \frac{4}{15}\gamma_I^2\gamma_S^2\hbar^2 S(S+1)\sum_k\frac{1}{r_{j,k}^6}, \tag{44}$$

and

$$M_{2\,homonuclear} = \frac{3}{5}\gamma^4\hbar^2 I(I+1)\sum_k\frac{1}{r_{j,k}^6}. \tag{45}$$

In summary, the previous discussion shows as, in presence of a rigid lattice, the second moment calculation only requires the knowledge of internuclear distances, which is provided directly from the crystal structure. It is worth noticing, however, that the extension of this model to the case of isotropic rotation of molecules is possible, even if it is not so straightforward. A calculation of the inter-molecular dipolar broadening performed in motional narrowing conditions will be described in the paragraph 3.1.5.

2.1.6.5 J-coupling

The j-coupling interaction, alias scalar coupling, is essentially due to the interaction between nuclei and the electrons in orbitals very close to the nucleus itself. As shown in figure 19 the interaction, mediated via the electron bonds, determines a spin-spin indirect coupling also between nuclear spins quite far one to each other, if they are connected with one or a few chemical bonds.

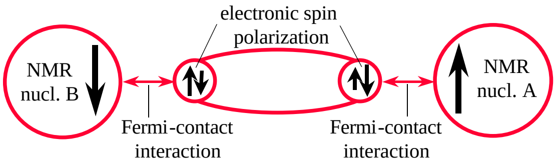

Figure 19: Pictorial representation of the scalar coupling between two nuclei (A,B), mediated through a single electron orbital: the Pauli exclusion principle determines the anti-parallel orientation of the nuclear spins

Two NMR active nuclei can, indeed, also interact indirectly with each other via electrons. Quantum mechanically, the scalar coupling can be subdivided into distinct components, but the most important contribution to the scalar coupling is the Fermi contact term. This term relies on the probability of finding an electron at the site of the two coupled nuclei. With this term, it is therefore expected that *s* orbitals will play a very significant role since their wavefunctions are the only ones that do not have nodes at the nuclear sites. Therefore *s*-like electrons are commonly considered as the only ones contributing in a significant way to this interaction.

Nevertheless, the nature of hyperfine spin-spin interaction between nuclei and electrons is dipolar, thus intrinsically anisotropic, consequently there are also anisotropic contributions to the j-coupling, which, however, are usually neglected in NMR measurements probing this interaction. J-coupling is usually present in high resolution NMR experiments where its

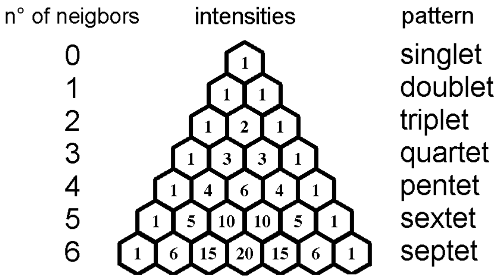

n° of neigbors	intensities	pattern
0	1	singlet
1	1 1	doublet
2	1 2 1	triplet
3	1 3 3 1	quartet
4	1 4 6 4 1	pentet
5	1 5 10 10 5 1	sextet
6	1 6 15 20 15 6 1	septet

Figure 20: J-coupling patterns arising from chemical shift equivalent nuclear spins. Based on the number of neighbour spins interacting, the Pascal triangle determines the peaks composition of the final spectra. The numbers inside the cells represent the relative intensities of the peaks.

dominating isotropic term yields characteristic features in the spectra.

Scalar coupling is responsible for the splitting of NMR lines relative to groupings of chemical shift equivalent nuclei. The peaks pattern arising from this effect is centered on the chemical shift value; it is composed by a variable number of peaks, which depends on the number of neighbour spins following the Pascal's triangle diagram reported in figure 20, where the numbers in the cells represent the relative intensities of the peaks.

2.1.6.6 Quadrupolar interaction

The quadrupolar interaction is the only relevant contribution to the total Hamiltonian of a nuclear spin system with an *electric* origin. All the different coupling channels discussed up to now arise from magnetic properties of the nuclei; in particular from the magnetic dipolar moment, while the quadrupolar interaction describes the coupling between the nuclear quadrupole moment and the electric field gradient at the nuclear site. It is non-zero only for nuclei with $I > 1/2$ and it is generally dominant (apart from the external Zeeman interaction). It can be shown that quadrupolar moment vanishes exactly for $I = 1/2$ considering in more detail the multipole series expansion for an electric charge distribution. The nucleus has charge, but not dipole moment since its charge is all positive. The electric quadrupolar term, thus, is the first non-zero contribution of the series: an ellipsoidal charge distribution (generic nuclear charge) can be represented by a spherical distribution plus a quadrupole; it follows that a spherically symmetric charge has no quadrupole moment. Indeed the physical interpretation of the quadrupolar moment is related to the symmetry of the charge distribution: this is the reason why it vanishes in spin 1/2 nuclei (see paragraph 2.1). The quadrupolar Hamiltonian can be written as usual, in the tensorial compact form:

$$\mathcal{H}^Q = \sum_{k=1}^{N} \mathbf{I}_k \cdot \mathbf{Q}_k \cdot \mathbf{I}_k, \qquad \text{where} \qquad \mathbf{Q}_k = \frac{eQ_k}{2I_k(2I_k - 1)\hbar}\mathbf{V}_k \tag{46}$$

where I_k is the spin of nucleus k, $\mathbf{Q}_k$ is its quadrupole coupling tensor, $\mathbf{V}_k$ is the electric field gradient tensor at the site of nucleus k and e is the modulus of the electron charge. The tensor $\mathbf{Q}_k$ is traceless: we can guess it from electrodynamics, considering the Laplace equation $\nabla^2 V = 0$ (being V the electric potential): it imposes a severe condition on the electric field gradient. In terms of the principal axis components of the tensor $\mathbf{V}_k$, the Laplace equation assumes, indeed, the form:

$$V_{k\ xx} + V_{k\ yy} + V_{k\ zz} = 0, \tag{47}$$

which means exactly $Tr\{\mathbf{V}_k\} = 0$.

2.1.7 NMR apparatus

The block diagram of a typical NMR apparatus is shown in figure 21; it includes the following elements.

- *NMR spectrometer.*
  The NMR spectrometer includes the electronics necessary to control pulses, delays and other instrumental parameters (attenuation, phase, etc.), such as complicated pulse sequences for specific experiments can be performed operating directly in the spectrometer computer interface which usually provides a pulse programmer routine.
  Such a complex instrument performs both the transmission and the signal acquisition. Figure 21 outlines these operation steps (transmission and acquisition) in two different blocks: a brief description of each block is provided in the next lines.

  Transmission. The radio-frequency generator produces a sine wave of the desired frequency; the pulse programmer sets the width operating on the gate, and in some cases the shape of the RF pulses. The RF amplifier increases the pulses power from milliwatts to tens or hundreds of watts. Afterward the amplified signal sees a decoupling circuit

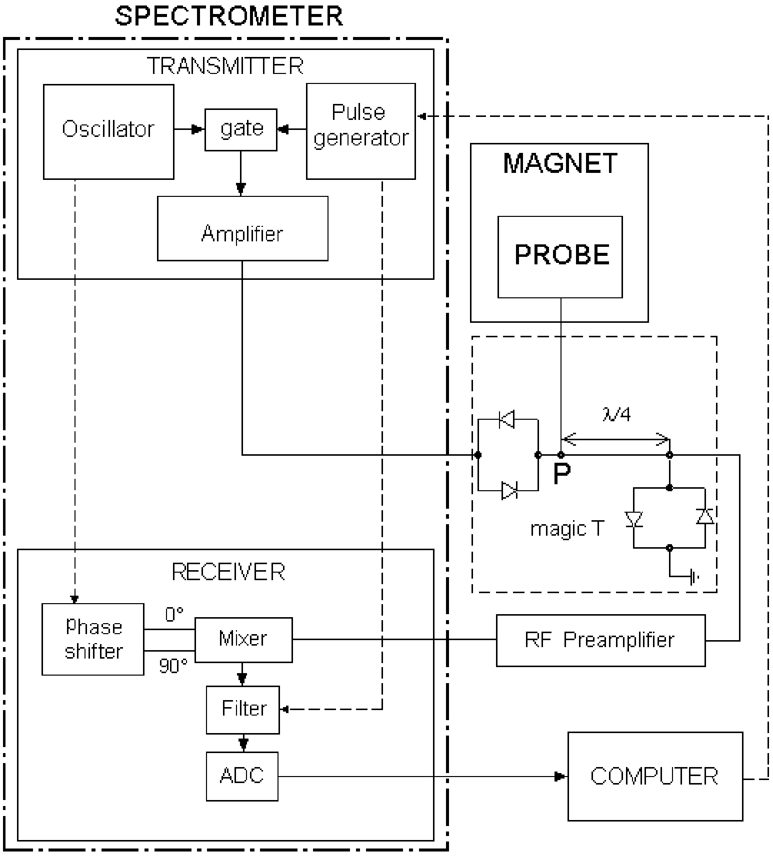

Figure 21: Block diagram of a typical NMR apparatus

where it is redirected through the NMR probe without significant intensity decrease due to reflections. The coupled diodes represent a short circuit for the high-power signal, thus since the length of the coaxial cable between the two sets of coupled diodes corresponds to 1/4 λ (λ being the signal wavelength) a stationary wave arises in the cable having maximum intensity in the point P, connected to the probe.

Acquisition. As a consequence of the excitation, in addition to the nuclear response, other spurious signals are generated in the probe. The mechanical response of the coil is partially responsible, for the persistence of the excitation signal in the first microseconds of the acquisition time, despite the proper instrumental dead time is accounted before starting to acquire. This effect is addressed to as "ringing" in the NMR language and must be excluded from the resulting spectrum by further increasing, if necessary, the time delay before the acquisition starts. On the contrary the induced nuclear response is a very weak signal which does not exceed the voltage threshold of the diodes. This is why the decoupling circuit during the reception time works in a different way than in transmission: the diode pairs, in this case, behave like open circuits, so that the signal can not go back to the transmission stage, but only to the sample circuit.

After the proper impedance matching is carried out by the preamplifier, the signal ν undergoes a complex acquisition procedure, called the *quadrature detection*, where it is mixed with a reference signal ν_0 having the same frequency, (since it originates from the same oscillator) yielding a consistent lowering of the signal frequency which allows a proper sampling. The quadrature detector is a device which separates out the M$_x$ and M$_y$ signals from the whole signal induced in the sample coil. For this reason it can be thought of as a *laboratory to rotating reference frame converter.* The heart of a quadrature detector is a doubly balanced mixer. It has two inputs and one output. If the input signals are $cos(A)$ and $cos(B)$, the output will be $\frac{1}{2}$ $cos(A+B)$ and $\frac{1}{2}cos(A-B)$. For this reason the device is often called a product detector since the product of $cos(A)$ and $cos(B)$ is the output. The quadrature detector typically contains two doubly balanced mixers and a 90° phase shifter: from the input frequencies ν and ν_0 the so called *real* ad *imaginary* parts of the acquired *free induction decay* come out. These represent the components of the transverse magnetization M$_x$ and M$_y$.

- *NMR probe: the sample circuit.*

  The basic circuit of NMR probes is represented in figure 22: the variable coil provides the impedance matching between the circuit and the external components. After the impedance is adjusted the resonance frequency can be regulated tuning the variable capacitor.

The probe circuit is essentially a modified RLC circuit including an extra variable

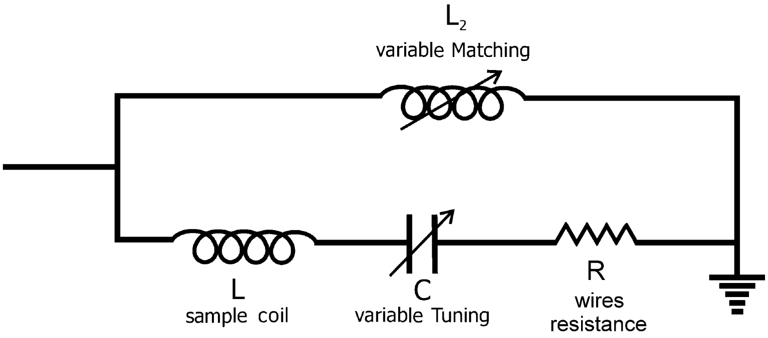

Figure 22: Basic circuit of an NMR probe

inductance as represented in figure 22. Actually experimental complications arise, as the tuning and matching parameters are related; all the circuit components influence each other and we can not treat the system as if it were a simple RLC circuit.

- *Superconducting magnet.*
  The principal feature of the superconducting magnets is the stability of the magnetic field in the persistent mode operation. In the superconducting circuit the time constant (L/R) tends to infinity, because R tends to zero, thus the magnet remains stable for days or even months at a nearly constant field. This characteristic assumes a great importance if signal averaging must be performed over an extended period of time as in NMR experiments involving nuclei with very low sensitivity (like ^{13}C).
  Nowadays different types of superconducting magnets are available: for applications in research institutes working with high-resolution or solid state NMR, magnets with vertical geometry are required (see figure 23); on the contrary magnetic imaging applications require magnets with horizontal geometry; the liquid helium is, however, a common element in the NMR magnets, which may reach fields up to 20 T. Indeed, the whole production of superconducting magnets, nowadays, makes use of low temperature superconductors (LTS) for the built up of the inner coil: this is essentially due to the mechanical properties of these materials, which are much more suitable for the industrial production of wires and filaments with respect to the high temperature superconductors (HTS). HTS lack of the necessary mechanical resistance, and, consequently could not resist to the mechanical stress induced by the high magnetic fields on the superconducting coil. Most superconducting magnets are wound using conductors which are comprised of many fine filaments of a niobium-titanium (NbTi) or niobiun-tin (Nb_3Sn) alloy embedded in a copper matrix for safety reasons: in case of quench the coil energy is mainly absorbed by the copper matrix yielding a controlled heating. These conductors have largely replaced the single filament conductors since the linearity of

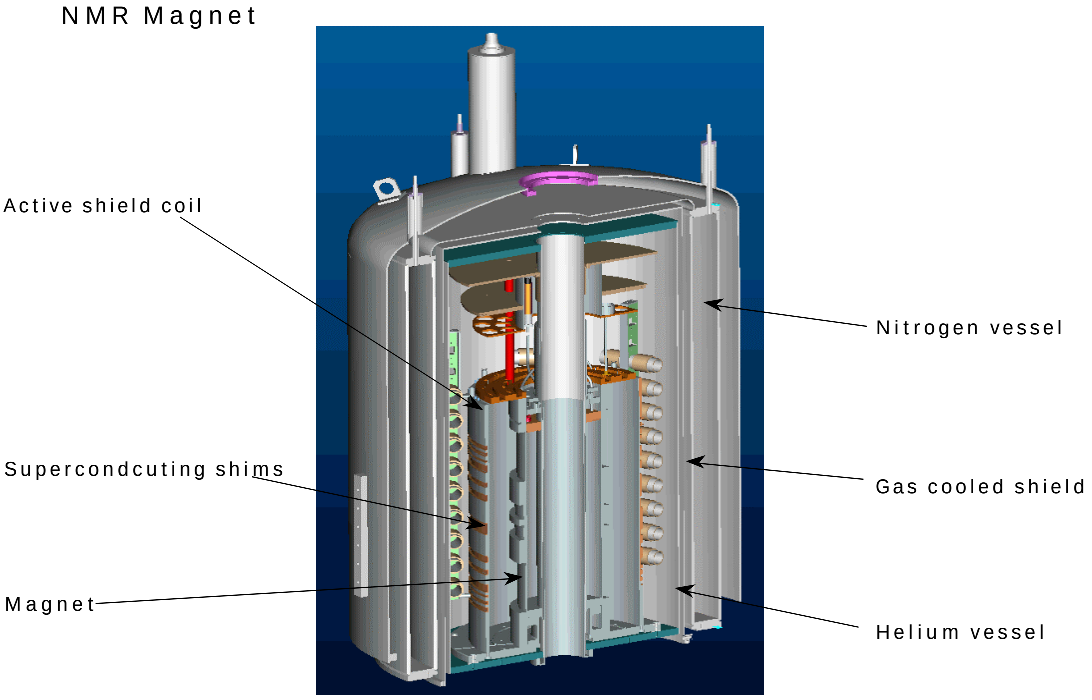

Figure 23: NMR magnet

the magnetic field and the magnet current result greatly improved. Another advantage of these conductors is the more rapid rate at which the magnet can be charged and discharged, typically a few minutes for most laboratory size magnets. A typical superconducting magnet for high-resolution and solid state NMR applications is shown in figure 23.

The instrumentation used in the NMR laboratory of the physics department (Parma University) include mainly the following equipment:

- Stelar e Tecmag spectrometers, used in the frequency range 25÷95 MHz for ^{13}C and ^{75}As, and up to 180 MHz for ^{19}F.
- Superconducting magnets Oxford Instruments, 200 Mhz, and Cryomagnetics, 9 T.
- Oxford cryostat CF 1200
- Home-made cryogenic NMR probe suitable for the Oxford cryostat CF 1200.

NMR measurements were performed as well in the Centro Interfacoltà Misure (CIM) of the University of Parma, with the following NMR instruments:

- Bruker spectrometer AMX 400 equipped with a high resolution probe ($< 1ppm$) for the superconducting magnet Oxford (400 MHz, 9.5 T).

2.2 SQUID magnetometry

Superconducting Quantum Interference Devices (SQUID) are very sensitive magnetometers used to measure extremely small magnetic fields even lower than 1 pT. The DC SQUID was invented in 1964 by Robert Jaklevic, John Lambe, Arnold Silver, and James Mercereau of Ford Research Labs after B. D. Josephson postulated the Josephson effect in 1962 [56,57] and the first Josephson junction was made by John Rowell and Philip Anderson at Bell Labs in 1963. In the electronic properties of the Josephson junction lies, indeed, the working principle of a SQUID; a brief description of such properties will be given in the following.

A Josephson junction is a piece of superconducting material "interrupted" by a thin insulating slab, so thin that it lets the superconductor charge carriers (the Cooper pairs) *tunnel* across the junction (figure 24)

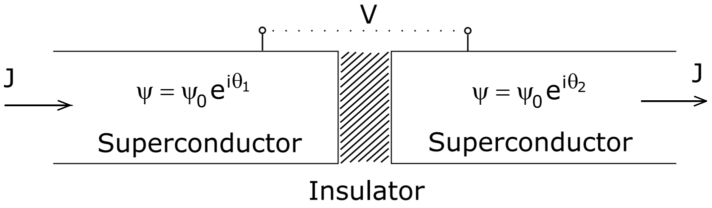

Figure 24: Josephson junction scheme.

In the superconducting state the charge carriers are bosons, thus, the ensemble of particles can be described with the same quantistic wavefunction which may be written in the complex form $\psi = \psi_0\, e^{i\theta}$, being ψ_0 and θ the magnitude and the phase. If the two superconducting regions were in contact the phase value would be the same, while in the Josephson junction the thin insulating slab allows the formation of a phase link between the superconductive regions because a finite tunneling probability is granted by a residual overlap of the wavefunctions (see figure 25b).

This well-defined relation among the phase values is called a *weak link* between two superconductors. The phase difference between the two superconducting elements is related to the number of tunneling particles, and hence to the current density J across the junction:

$$J = J_0 \sin(\delta_0), \;\; \delta_0 = \theta_1 - \theta_2, \tag{48}$$

where θ_1 and θ_2 are the phase values of the two superconductors. On the other hand, the voltage across the junction can be calculated as

$$V = \frac{\hbar}{2e} \frac{\mathrm{d}\delta_0}{\mathrm{d}t}\,. \tag{49}$$

A SQUID consists in a superconducting ring (see figure 25a) interrupted by two Josephson

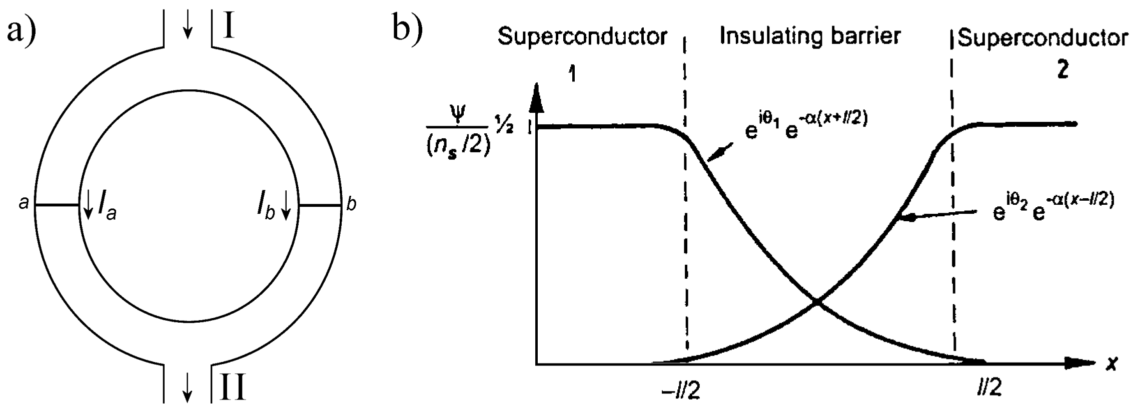

Figure 25: (a) Schematic illustration of a SQUID, consisting in a superconducting ring interrupted by two Josephson junctions, a and b. The current I through the device is modulated by the magnetic flux threading the loop area. (b) Variation of the superconducting wavefunction in the vicinity of a Josephson junction. The exponential decay of ψ in the barrier is due to tunneling of Cooper pairs.

junctions. Its working principle can be described in a few words: in the ring a bias current is always present and a magnetic field concatenated with the superconducting loop yields a different extra phase shift in the two tunnel junctions a and b (see figure 25a), according to the equations

$$\delta_a = \delta_0 + \frac{e}{\hbar}\Phi\,,\ \delta_b = \delta_0 - \frac{e}{\hbar}\Phi\,, \tag{50}$$

thus, equation 48 assumes the form:

$$j = j_a + j_b = 2j_0 \cos(e\,\Phi/\hbar)\sin\delta_0\ . \tag{51}$$

In particular the whole current-voltage characteristic of the SQUID depends on the external flux, and the measured voltage turns out to be *periodic* itself with the external flux with the periodicity of a single flux quantum $\Phi_0 = \frac{h}{2e} = 2 \cdot 10^{-15}$ T m^2 $= 2 \cdot 10^{-5}$ G mm^2 [9].

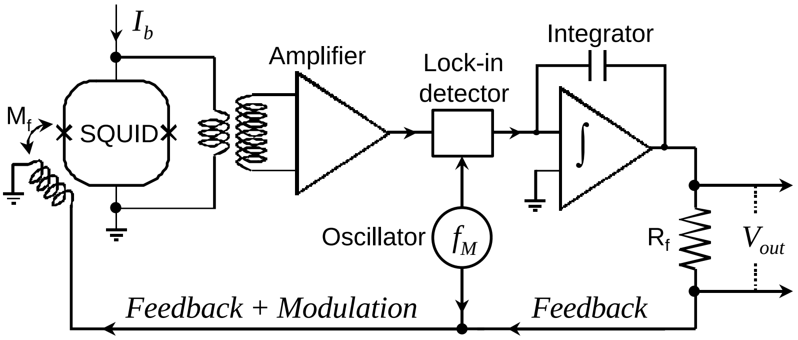

Figure 26: Fluxed Locked Loop (FLL) configuration for SQUID electronics

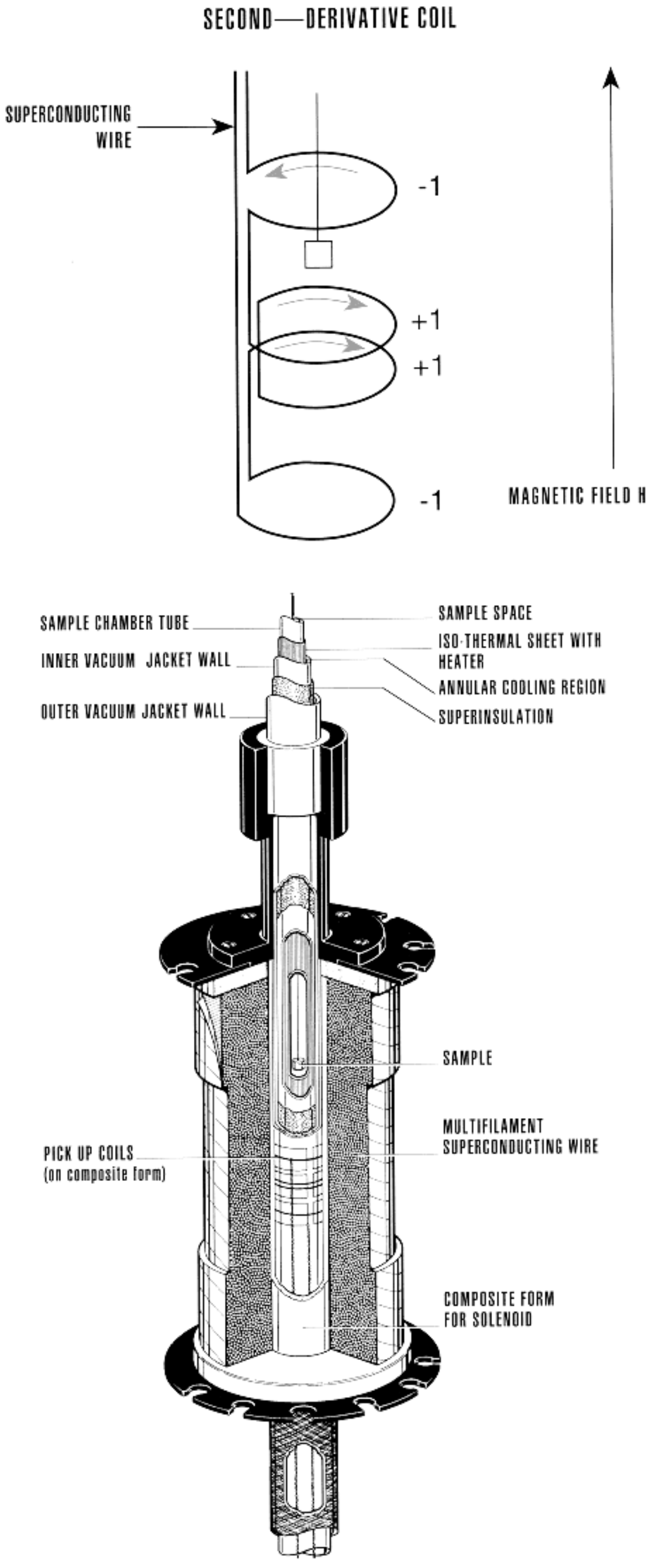

Figure 27: A second order gradiometer pick-up coil is shown in the upper figure: the opposition between the central and the external coils decouples the SQUID response from external fields. The real pick-up coil scheme of a commercial SQUID is reproduced at the bottom.

SQUIDs, thus, are commercially used as extremely sensitive magnetometers, capable of detecting very small magnetic fields, such as those generated within the living body between 10^{-9} T to 10^{-6} T.

The voltage output of the SQUID loop is not directly measured, however: the configuration called *flux-locked-loop* (FLL) (figure 26) is widely used in the commercially available SQUIDs in order to reduce the noise and increase the sensitivity to the maximum levels. Moreover another reason prompts to avoid a direct measure of the sample flux: external magnetic fields are quite often applied in a typical SQUID measurement: their variation could strongly interfere with the measurement itself. Thus the SQUID is generally isolated from the effect of external fields and the magnetic flux variation is measured by a specifically designed pick-up coil arranged in a second-order gradiometer configuration (see figure 27).

The flux variation induced by moving the sample through the pick-up coil can be evaluated with the formula

$$\Phi_B = \frac{\mu_0 m}{2} \cdot \frac{R^2}{(x^2 + R^2)^{3/2}} \ , \tag{52}$$

expressing the flux of the magnetic moment $\mathbf{m}$ having position x along the axis of a coil with radius R. The induced voltage V turns out to be

$$V(x) \propto \frac{\mu_0 m R^2}{2} \sum_{i=1}^{4} \left[(x + d_i)^2 + R^2\right]^{-3/2} , \tag{53}$$

where d_i indicate the relative positions of the single coils in the gradiometer configuration. The overall voltage signal is detected performing a scan over the precalibrated position range; a typical curve is shown in figure 28.

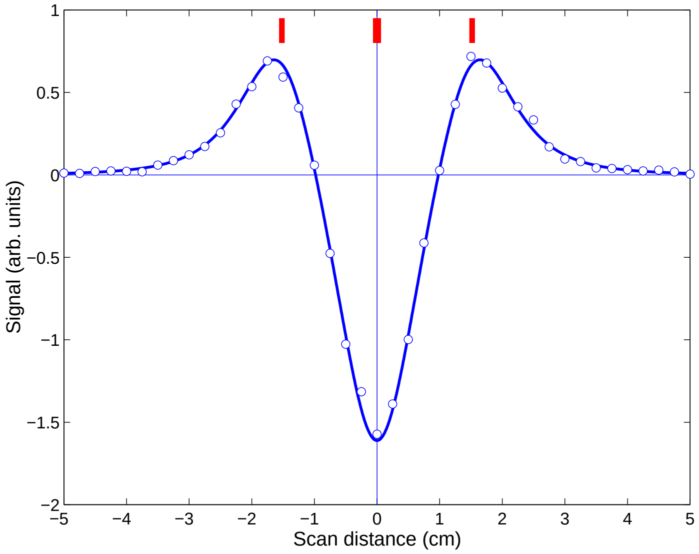

Figure 28: A typical SQUID signal

2.3 X-ray Diffraction

The first method employed in X-ray crystallography is single-crystal X-ray diffraction (XRD). It represents a powerful tool for the investigation of unknown crystalline materials, due to the fact that x-rays possess a wavelength comparable with the typical atomic and molecular distances (~ 1 Å) giving rise to the diffraction phenomena: the X-rays beam is reflected from the atomic planes within the crystal structure, producing a pattern of spots called reflections. Each reflection corresponds to one set of evenly spaced atomic planes. The density of electrons within the crystal is determined from the position and the intensity of the various reflections observed as the crystal is gradually rotated in the X-ray beam; this density, together with other supplementary data, allows the atomic positions to be inferred.

On the contrary, for powder samples the extraction of the structural information results more complicated. Polycrystalline materials are made up of a great number of tiny (μm to nm) single crystals; Figure 29 shows the different diffraction patterns coming from a single crystal and from a polycrystalline sample. The diffracted rays from a single crystal point to precise directions each corresponding to a family of diffraction planes. The diffraction pattern from a polycrystalline powder sample forms a series of diffraction cones, namely the *Debye-Scherrer cones*, each corresponding to the reflection from the same family of crystalline planes in the different powder grains.

Examples of these patterns formed by rings, are represented in figure 30.

In the last 2 decades, however, the development of very effective mathematical procedures (Rietveld method) for the quantitative analysis of powder diffraction patterns determined the rapid diffusion of this method which nowadays can be considered as one of the main investigation techniques in material science.

The compounds studied in this thesis work where in polycrystalline form, due to the impossibility, so far, in the synthesis phase, to produce single crystals. Hence powder diffraction experiments and successive analyses were performed on the samples; however, to a first understanding of the x-ray diffraction technique, a brief overview of the basics of single crystal

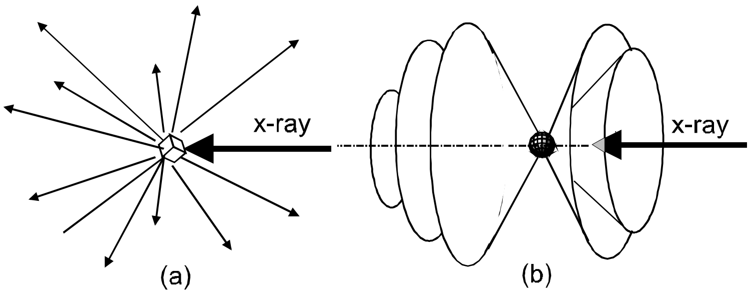

Figure 29: The patterns of diffracted x-rays: (a) from a single crystal and (b) from a polycrystalline sample.

diffraction will be presented.

2.3.1 X-ray scattering and interference

The scattering of a coherent x-rays beam by the atoms of a crystal lattice is determined by two contributions:

- *Thomson scattering* which represents the coherent part,
- *Compton scattering* which, on the contrary, is intrinsically incoherent.

The coherent contribution of the scattered beam gives rise to the well known interference effect which can be described, to a first approximation, by the Bragg's law $2d\ sen(\theta) = n\lambda$. From a classical point of view, the scattering process may be divided in two steps: firstly the incoming radiation is absorbed by the electronic shells, and then re-emitted. The radiation coming from the Thomson process is coherent, thus, it gives rise to the interference effect; however, as reported above, in the scattering process there is also a non negligible contribution from incoherent radiation, ascribed to the Compton process, where the wavelength of the emergent radiation changes accordingly to the equation [40]:

$$\Delta\lambda(\text{Å}) = 0.024(1 - cos2\theta)\,. \tag{54}$$

The incoherent signal appears in the measurements as a diffuse background signal.
The detailed description of the interference between scattered waves has been provided in the references [40,88]; here I summarize the results of the cinematic X-ray diffraction theory which has been developed neglecting the multiple scattering events (*weak* scattering conditions) with the aim to provide a method for extracting structural information from the data. The integrated intensity of the Bragg scattering for a single crystal turns out to be

$$I_{sc}\ (photons/sec.) = \Phi_0\ r_0^2\, P\, |F(\boldsymbol{Q})|^2\, N \frac{\lambda^3}{V_c} \frac{1}{sin2\theta} \tag{55}$$

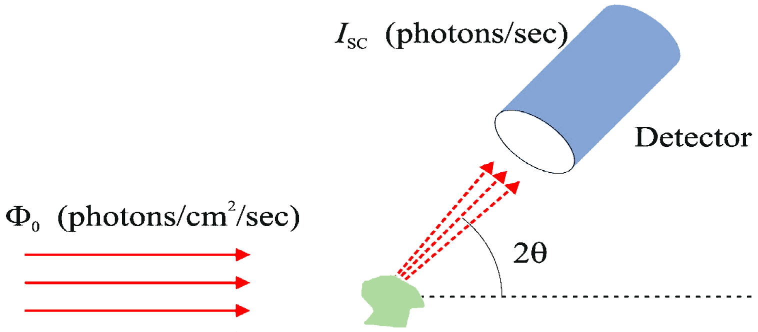

where $r_0^2\, P$ is the classical Thomson scattering term (r_0 is the electron radius and P the polarization factor), $F(\boldsymbol{Q})$ is the structure factor of the unit cell and V_c the unit cell volume in the reciprocal space. The intensity, thus, provides direct information on the absolute value of the structural factors.

2.3.2 X-ray powder diffraction

The general procedure identified in order to extract the crystallographic structure of new materials from diffractions data is summarized in the following.

1. *powder pattern indexing*: the dimensions and the cell symmetry operations must be identified to assign the proper set of Miller indexes to each reflection in the spectrum;

2. *extraction of the measured intensity*: this operation provides the information on the structure factors;

3. *implementation of a structural model for the unit cell*: starting from the structural factors many methods can be used to guess the disposition of the atoms in the unit cell. Probably the newest approach to this problem consists in operating directly in the direct space translating and rotating a fragment of the structure (supposed to be known *a priori*) with Monte Carlo based techniques. The XRD data analysis whose results will be presented in the section 3.1.2 was carried out with the *simulated annealing* procedure, which performs the Monte Carlo calculation simulating alternatively the motional dynamics in annealing and cooling conditions.

4. *optimization of the model parameters*: the parameters are optimized using routines based on the Rietveld method.

The Rietveld method performs the optimization using simultaneously all the information extracted from the diffraction pattern (including lineshapes): it involves a complicated *least squares* calculation that only the recent advances in computer technologies allowed to be easily executed with conventional personal computers.

The possible geometries in a x-ray powder diffraction experiment are essentially Bragg-Brentano and Debye-Scherrer geometries . In the former case the experiment is performed with reflection configuration, while the latter requires a transmission configuration; for a detailed description see reference [88]. The XRD results which will be showed in the section 3 refer to experiments performed in Debye-Scherrer geometry, where the powders are stored in a quartz capillary having diameter ~ 0.7 mm.

Modern powder x-ray diffractometers consist of an x-ray source, a movable sample platform, an x-ray detector (usually a scintillation detector), and the associated computer-controlled electronics. The sample is positioned in the center of the goniometer while the

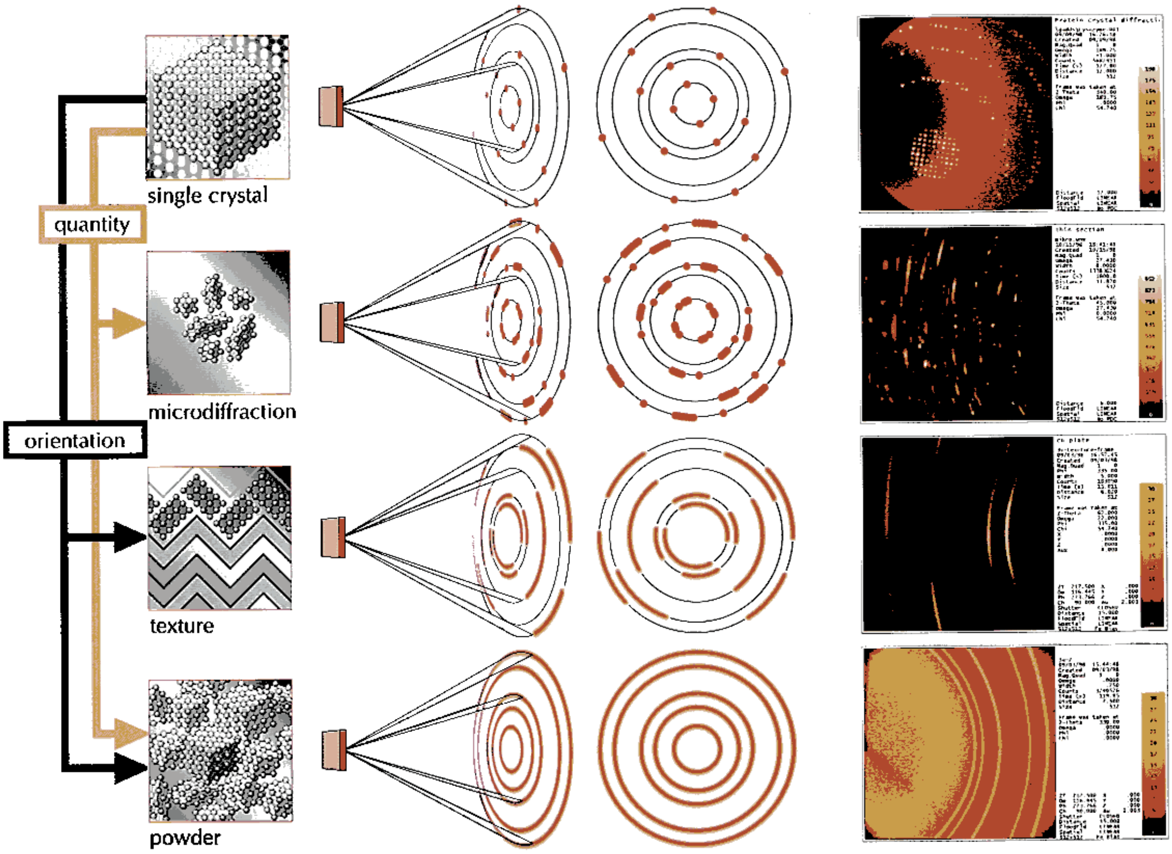

Figure 30: Patterns of diffracted x-rays: different examples depending on the specimen nature.

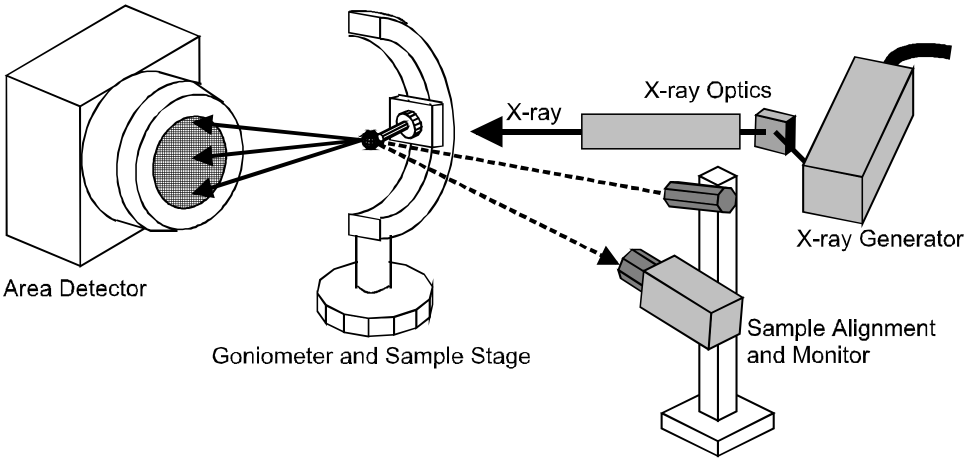

Figure 31: Five major components in an XRD system, an area detector, an x-ray generator, x-ray optics (monochromator and collimator), goniometer and sample stage, sample alignment and monitoring (laser/video) system.

sample holder spins slowly during the experiment to improve the homogeneity of the powder scattering. The x-ray source is a Cu or Mo anode.

2.4 μSR technique

The acronym μSR assumes different meanings, muon spin Rotation, relaxation or resonance, depending on the types of experiment performed.

Although analogous, in principle [28], to other spectroscopic techniques, widely used in solid state physics like NMR and EPR (electron paramagnetic resonance), μSR must be performed in a large scale scientific facility (PSI and ISIS in Europe) because the microscopic probes used to investigate the electromagnetic interactions in the materials are muons (rather than nuclei or electrons).

μSR measurements provide information on the distribution of internal fields, and consequently used to investigate magnetism and superconductivity. Because of their high magnetic moment, about $4.5 \cdot 10^{-26}$ J/T, the muons are sensitive to extremely small magnetic fields, up to 10^{-5} T. Moreover, since in principle the muons implantation takes place randomly in the sample, the signal amplitude in the spectrum turns out to be proportional to the volume fraction; this technique is therefore very useful in the study of multiphasic or partially ordered samples.

The muons were discovered firstly in 1933 by P. Kunze: in a Wilson chamber he observed the path related to such a new ionizing particle having electric charge (+1,-1) and lifetime of 2.2 μs. It turned out that muons may reach the earth surface thanks only to the relativistic time delation. The discovery of Kunze represented thus the first experimental proof of the special relativity predictions. Afterward the particle mass was precisely determined as $m_\mu = 205\ m_e$ and it was pointed out that pion decay was the principal mechanism responsible for the muons production:

$$\pi^- \rightarrow \mu^- + \bar{\nu}_\mu \,, \tag{56}$$

$$\pi^+ \rightarrow \mu^+ + \nu_\mu \,. \tag{57}$$

The weak nuclear interaction leads the pion decay, thus a parity violation takes place, yielding the emerging muons to have negative helicity, $e = -1$ (by defining $e = \mathbf{p} \cdot \mathbf{S}$ where $\mathbf{p}$ is the momentum of the muon and $\mathbf{S}$ its spin).

The muons polarization is therefore fixed by the pion decay;

The μSR measurements which will be shown in this thesis work were performed at the ISIS facility, Rutherford Appleton Laboratory, Chilton (Oxford), UK. Here The muons are produced by colliding the ISIS proton beam on a 10 mm thick carbon target 20 m upstream of the neutron target. Collisions produce pions which decay with a mean lifetime of 26 ns

into muons. Thanks to the pion decay the muon beam is fully polarized, and this polarization is maintained as the beam is transported to the muon spectrometers. The muon target uses only 2-3% of the proton beam, thus, muons can be considered as a secondary product, since almost the whole beam is dedicated to the neutrons production.
In μSR experiments positive muons only are selected and implanted in the samples, since the negative ones may undergo a nuclear capture, which yields not negligible effects in case nuclei with high atomic number are involved.

After the beam of 100% polarized muons is implanted in a sample, the information on the muon spin precessions and relaxations is indirectly provided by the angular distribution of positrons emitted in the following weak decay

$$\mu^+ \rightarrow e^+ + \nu_\mu + \bar{\nu}_e \,. \tag{58}$$

Due to the parity violation, the emitted positrons are distributed about the muon spin direction according to the probability function

$$W(\theta) = 1 + a \; cos \; \theta, \tag{59}$$

where θ is the angle between the muon spin and the direction of the positron emission. The factor a, known as the *asymmetry factor*, increases monotonically with the positron energy up to a value $a = 1$ (see figure 32) for the maximum energy of 52.83 MeV.

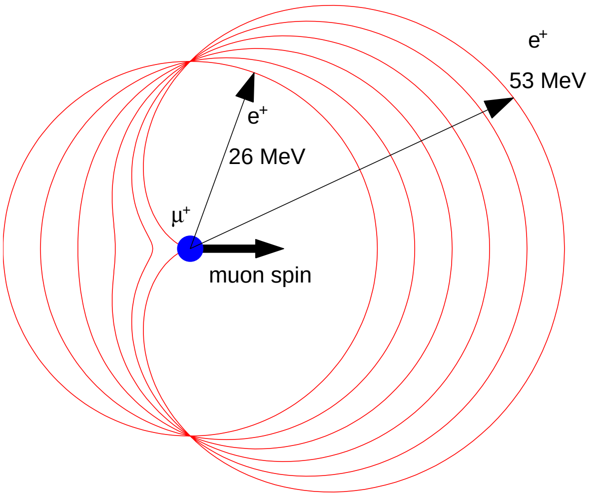

Figure 32: Muon decay: the figure shows the angular distribution of positrons from positively charged muons for various positron energies. Maximum energy ~53 MeV.

The positrons are collected by two banks of detectors arranged respectively in forward and backward positions, so that the asymmetry factor may be inferred from a further analysis of the positrons counts. Of course the measured asymmetry does not represent exactly the parameter a, since empirical factors like the detector sensitivity and the experimental geometry influence the measurement prompting for the identification of the asymmetry through

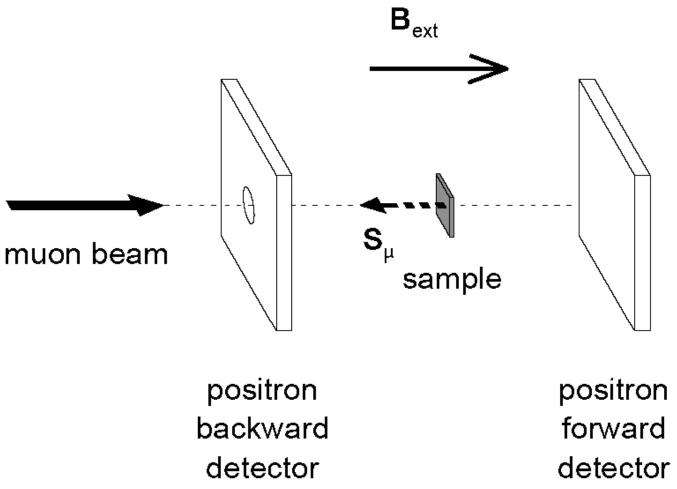

Figure 33: Arrangement of the muon detectors for LF and ZF μSR experiments. Adapted from [29].

the empirical factor A. The evolution of the muon spin polarization is finally described by the difference between forward and backward counts, after the separate summation over the detector banks is performed.

The two most common experimental configurations used in μSR experiments are the transfer field geometry (TF) and the longitudinal field geometry (LF or ZF if the magnetic field is set to zero). In the former a constant magnetic field is applied in a direction perpendicular to the muon spin polarization, in the latter, on the contrary, it is applied along the same direction of the muon spin. The measurements performed on the lithium phthalocyanines which will be discussed in the paragraph 3.2.1 were performed in zero field LF geometry, with the aim to observe the muons precessions induced by the internal fields. TF measurements were used only for calibration procedures, which will not be described here (see the references [14, 105]); in the next paragraph a brief description of the typical μSR experiment in LF geometry will be provided.

2.4.1 Longitudinal field (LF) and zero field (ZF) μSR: Muon Spin Relaxation

In LF or ZF geometry, the positrons counts in the detectors B (backward) and F (forward) (figure 33) are expressed by the relation

$$N_i(t) = N_{oi} e^{-\frac{t}{\tau_\mu}} [1 + AG(t) \cos\theta_i] \qquad i = F, B \tag{60}$$

where θ=0 corresponds to $N_B(t)$ and $\theta = \pi$ to $N_F(t)$. $AG(t)$ represents the so called decay asymmetry P or longitudinal polarization: this is the physical quantity which provides information on the sample intrinsic behaviour. Equation 60 is derived from 59 where the asymmetry parameter a has been substituted by $AG(t)$. A is the empirical asymmetry factor and $G(t)$ represents the complex time evolution resulting from the interaction between the muon and the magnetic fields surrounding it (external + internal field in LF, while only internal in ZF measurements). Since the terms $N_B(t)$, $N_F(t)$ have been calculated from the collected data, the longitudinal polarization P turns out to be:

$$P(t) = \frac{N_F(t) - \alpha N_B(t)}{N_F(t) + \alpha N_B(t)} = AG(t) \tag{61}$$

where α is an empirical geometrical parameter related to the position of the sample: it can be inferred from a calibration measure performed in TF configuration. It is, in principle, necessary to plan a calibration run every time the sample holder position is slightly modified (*e.g.* in case of sample substitution, etc.)

In conclusion, for the sake of completeness, a few examples of muon relaxation functions will be described.

When the muon is implanted in the sample, it can either behave as a free particle in an equilibrium condition surrounded by static fields, it can sense fluctuations in the local fields or "jump" among different positions or, finally, interact with an electron forming a bound state called *muonium* [70]. In the former case, the muon sees as a local magnetic field the sum of the external field and the dipolar fields generated by the neighbouring magnetic moments of electrons or nuclei. In *ZF* conditions the dipolar fields are randomly oriented: this is usually taken into account with a Gaussian fields distribution or, in the approximation of a dilute spin system, with a Lorentzian distribution. The resulting polarization can be calculated as the well known Gaussian or Lorentzian Kubo-Toyabe functions:

$$\mathrm{P}(t) = \frac{1}{3} + \frac{2}{3}\left(1 - \sigma^2 t^2\right) e^{-\sigma^2 t^2/2} \tag{62}$$

or

$$\mathrm{P}(t) = \frac{1}{3} + \frac{2}{3}\left(1 - \lambda t\right) e^{-\Delta t/2} \tag{63}$$

where σ and λ describe the width of the distribution function for the local field at the muon site. Roughly speaking the Kubo-Toyabe functional form can be justified from the following considerations based on the 3 spatial directions: in a powder sample 1/3 of the muons feels a magnetic field parallel to the initial polarization direction, while 2/3 will precess initially and, thus, start dephasing progressively yielding the decay of the corresponding signal. A much more complicated situation arises if the muons jump between different positions or if static muons sense fluctuations in the local fields. From complex calculations the longitudinal polarization function turned out to be Lorentzian in the *strong collision approximation* (extreme *motional narrowing* conditions in NMR language).

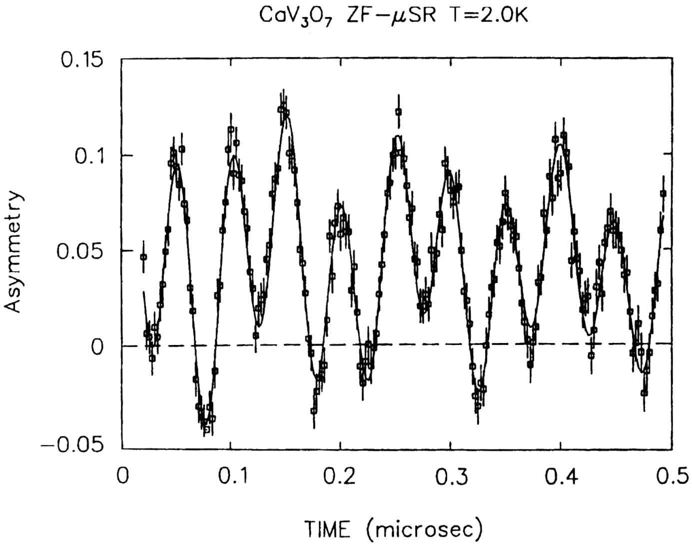

Figure 34: Asymmetry oscillations in an antiferromagnet: ZF μSR spectrum observed in an antiferromagnet, CaV$_3$O$_7$, at T = 2 K. The asymmetry evolution results from the presence of two precessing frequencies while 1/3 of the muons shows a non precessing asymmetry. Adapted from [105].

In summary from the previous considerations the expected longitudinal polarization for a magnetically ordered system can be inferred: in the case of an *antiferromagnet* the bulk magnetometry can only observe the overall magnetization, which is expected to be extremely small because of the competition between two magnetic lattices in antiparallel orientation. In such a condition $ZF - \mu$SR experiments are extremely useful, since μSR acts as a direct probe of the local microscopic field: the muons fraction (2/3) with polarization perpendicular to the direction of the magnetic lattices precess with a unique frequency yielding a finite damped oscillation to appear (figure 34). The remaining (1/3), on the contrary feels a longitudinal field contributing, thus, with a constant component.

Chapter 3

Results and Discussion

In this section the results obtained using the characterization techniques previously described in order to investigate the fullerenium salts and the lithium phthalocyanines will be reported.

3.1 The Fullerenium salt $C_{60}(AsF_6)_2$

The synthesis reaction described in the paragraph 1.3.1 [85] yielded the formation of a new C_{60} phase with a crystallographic structure completely different from the structure of pristine C_{60}: it appeared immediately evident, from preliminary laboratory XRD measurements performed with the BRUKER AXS diffractometer of the physics department.

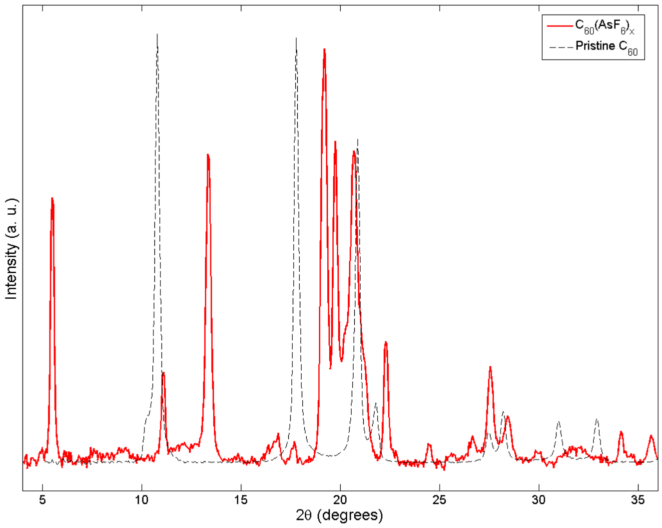

Figure 35: laboratory XRD on $C_{60}(AsF_6)_2$: the new phase (red solid line) shows a strong symmetry loss in comparison with the cubic structure of pristine C_{60} (black dashed line). No unreacted C_{60} was found.

The absence of reflections corresponding to unreacted C_{60}, in the XRD spectrum, is a clear indication of the good efficiency of the reaction (see figure 35).

However, the strong deviation from the cubic symmetry caused much more difficulties in indexing the unit cell of this structure. Figure 35 shows the laboratory XRD spectrum of the new phase: an unresolved group of peaks is evident in the region between the values $17° - 23°$ of the scattering angle 2θ.

The diffraction pattern of this new C_{60} phase was tentatively indexed with the semi-exhaustive method proposed by Werner, Eriksson and Westdahld [109] where a permutation of the Miller indexes through a trial and error routine is performed. Different cells (cubic, tetragonal, orthorhombic, etc.) are used in order to find the best match between the calculated and observed reflections, starting from those with higher intensity. It is one of the most efficient methods of powder pattern indexing available and implemented, nowadays, in various software suite, such as *Materials Studio* (Accelrys software). Afterward, with the Le Bail analysis a preliminary fit of the diffraction pattern was achieved: it takes into account the cell and the profile parameters and provides the knowledge of the space group through the extracted intensities. If the unit cell has been properly identified each reflection in the XRD pattern must be fitted in the Le Bail analysis. In our case, on the contrary, the indexed orthorhombic cell ($a = 9.95$ Å, $b = 8.95$ Å, $c = 16.2$ Å) did not reproduce all the peaks in the diffraction pattern: the necessity of a more detailed analysis with synchrotron light X-Ray diffraction appeared unavoidable in order to identify the crystal structure of the new compound.

Moreover, in parallel to the synchrotron light diffraction experiment, our efforts have been devoted to the measurement of the compound density. As reported in the paragraph 2.3.2 the extraction of the structural data from a powder diffraction pattern requires, after the unit cell indexing and the assignment of the proper space group with the Le Bail analysis, an implementation of a preliminary structural model for the unit cell which, in this case, has been provided by the simulated annealing procedure. The knowledge about the density of the compound, providing information on the proper stoichiometry in the unit cell, represents an important input parameter for the simulated annealing as well as a check for the consistency of the results. The density measurement performed on our powder samples will be described in the next paragraph, whereas the results of the synchrotron data XRD analysis will be presented in the paragraph 3.1.2. To a first sight however, the strong lowering of the symmetry from the cubic pristine C_{60} seems to be compatible with the polymerization of the fullerene units. Similar indication was given by ^{13}C NMR measurements at low temperature (80 K) where all the rotational C_{60} dynamics are frozen: in these conditions the anisotropic interactions contribution is no more averaged to zero by the motional narrowing, thus, the characteristic lineshape can be observed. The detailed analysis of the NMR spectra will be shown in the paragraph 3.1.3, as a confirmation of the structure identification; however it was immediately possible to identify, to a first sight, that the lineshape was formed by two contribution:

- the chemical shift tensor relative to the sp^2 carbon atoms of the C_{60}-cage;
- an extra peak which can be ascribed to the presence of sp^3 hybridized carbons, as it is expected to observe in polymerized C_{60} systems, where the C_{60} molecule is distorted in correspondence to the carbon atoms involved in the polymer bonds.

3.1.1 Powder density determination: gas pycnometry

In this paragraph the experimental density measurement of the fullerenium salt $C_{60}(AsF_6)_2$ in powder samples is reported. The knowledge of the density represents an important parameter for structural investigation of new materials.

The comparison between the experimental information and the theoretical one (coming from the preliminary Le Bail analysis of synchrotron X-ray data) represents a further input for the simulating annealing routine, as well as a consistency check for the final refined structure.

Unfortunately the evaluation of the density in our powder samples is not straightforward: the many empirical methods commonly used to evaluate the powders volume can not be used in this case. They are based on extremely rough approximations which do not take into account the powders peculiarities; on the contrary many empirical factors influence the apparent volume of powders, such as the electrostatic properties.

Moreover, the impossibility to perform the volume measurements with the conventional liquid pycnometers (widely used in chemistry laboratories to evaluate the density of liquid samples) prompted us for the implementation of a home-made *gas pycnometer*.

The gas pycnometry is based on the Boyle-Mariotte's law, which lies in the direct application of the ideal gas law when temperature remains constant. A gas pycnometer operates by detecting the pressure change resulting from displacement of gas by a solid object, as well as by a powder. Figure 36 helps to explain the technique. A sample of known mass is loaded into a chamber of known volume (V_s) that is connected by a closed valve to a gas reservoir, also of known volume (V_r), at a higher pressure (P_r) than the chamber (P_s). After the valve is opened, the final pressure in the system (P_{sys}) allows the unknown sample volume (V_x) to be determined by application of the ideal gas law, PV = nRT.

Assume the system is maintained at a constant temperature T and there is no net loss or gain of gas, that is, the number of gas molecules n is constant throughout the experiment. when the valve is opened the pressure in the reference volume will fall and the pressure in the sample chamber will rise. The larger the volume of the unknown sample, the higher will be the final system pressure, while the initial pressure of the reference chamber represents the upper limit the pycnometer can reach in the case 100% of the volume of the sample chamber is filled by the powder. Mathematically, the initial condition (36a) is

$$P_s(V_s - V_x) + P_r V_r = nRT\,, \tag{64}$$

where R is the gas constant.
After the valve is opened (36b), the condition changes to

$$P_{sys}(V_s + V_r - V_x) = nRT\,. \tag{65}$$

This leads to the expression

$$P_s(Vs - Vx) + P_r V_r = P_{sys}(V_s + V_r - Vx)\,, \tag{66}$$

which can be solved in terms of the unknown quantity Vx,

$$V_x = \frac{(P_{sys}Vs + P_{sys}Vr - P_s V_s - P_r V_r)}{(P_{sys} - P_s)}\,. \tag{67}$$

The accuracy of the method lies mainly in the precise determination of the known volumes (V_s and V_r) and, if necessary, in the calibration of the pressure sensor; moreover both the pycnometer main body material and the analysis gas must be moisture free, as well as the sample. If there are volatile substances within the powder, their partial pressures and cause error and instability. After tuning properly all these parameters, the residual contribution of the instrument to error is confined to leaks and temperature gradients.

Our home-made pycnometer is shown in figure 37; in this case, although the typically used gas is helium, it is designed for operating in the controlled argon atmosphere of our MBRAUN glove box: the air sensitivity of the fullerene compounds makes unavoidable to perform the sample manipulation in controlled atmosphere with moisture and oxygen concentration less than 1 ppm. The instrument works after the complete evacuation of the sample chamber, so that the pressure P_s tends to 0 and the equation 67 becomes

$$V_x = \frac{(P_{sys}Vs + P_{sys}Vr - P_r V_r)}{P_{sys}}\,. \tag{68}$$

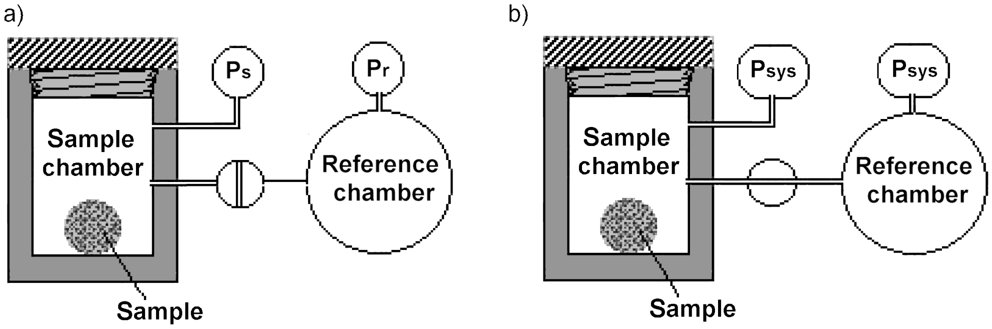

Figure 36: Operation of a precalibrated gas pycnometer.

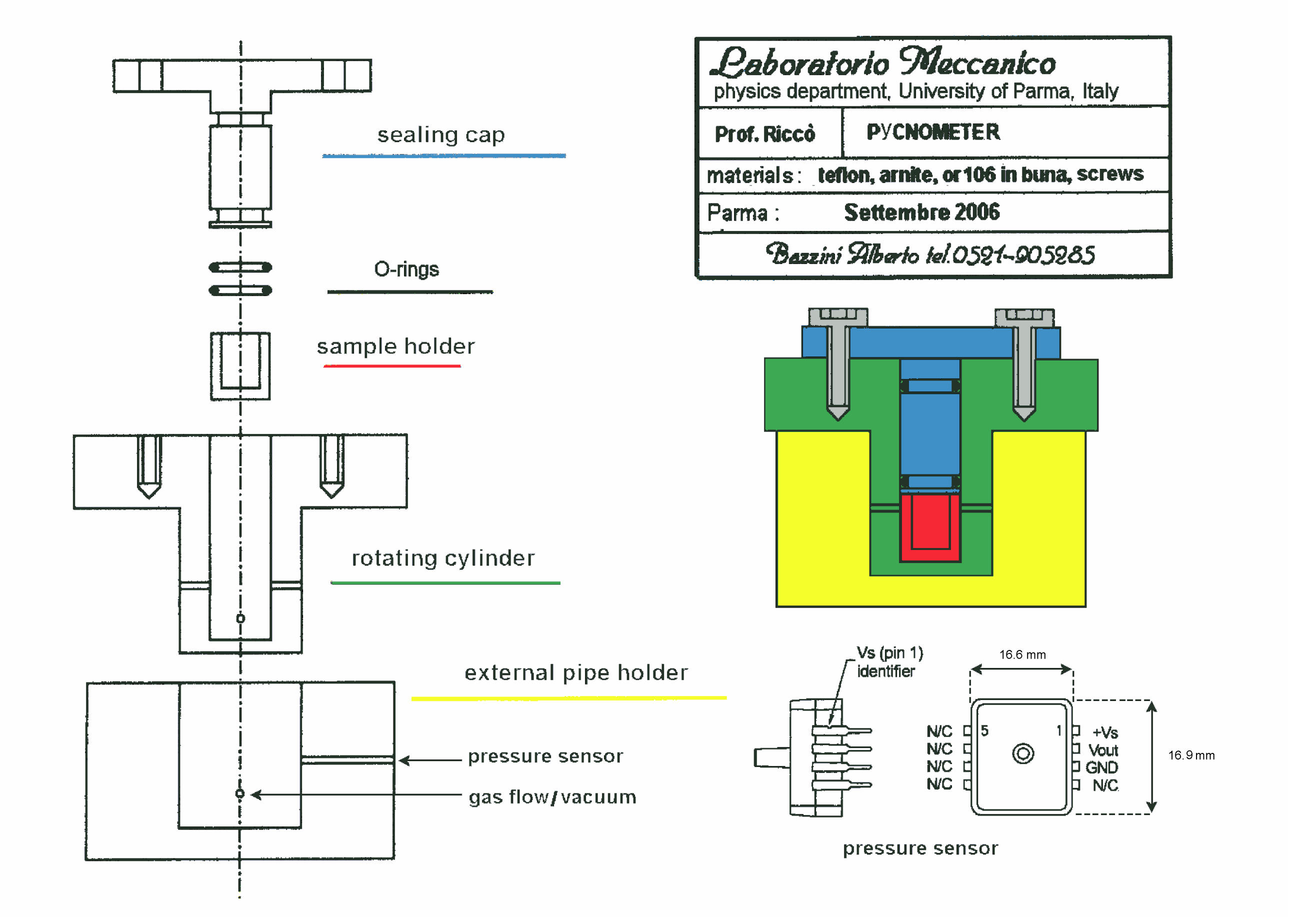

Figure 37: Home-made pycnometer

To reach the optimal working conditions a preliminary evacuation time period is necessary in order to avoid instabilities due to outgassing. The pressure sensor is a signal conditioned high precision trasducer which perform absolute measurements in the range 0-1000 mBar (BSDX series, *Sensortechnics*). Thanks to its reduced physical dimensions (16.6× 16.9 mm), it is applied directly on the external pipe holder; in particular the conic tip is sealed inside the pycnometer body and it is connected to the sample space through a hole with diameter of 1mm. Similar holes provide vacuum and gas flow: depending on the position of the rotating cylinder, the sample chamber may be connected with the pressure sensor (to perform the measurement), with the vacuum pump or the external argon atmosphere. The reference chamber is the internal volume of the pressure sensor itself ($\sim$200 mm^3).

The density measurement of the $C_{60}(AsF_6)_2$ samples was performed on 97.8 mg of powder, corresponding to a volume of $\sim$39 mm^3, yielding a density equal to 2.3 ± 0.1 g/cm^3. Although, in order to increase the measurement accuracy, the sample chamber was designed to measure even higher volumes (more than 100 mm^3, being the reservoir volume $\sim$ 200 mm^3), the apparent extremely large powder volume hindered the manipulation procedure. The experimental density value found is, eventually, considerably higher than the well known density of the pristine C_{60} (1.65 g/cm^3): this fact is consistent with the presence of heavy atoms, like arsenic, in the crystal structure. The measured value (2.3 ± 0.05 g/cm^3) can be considered as a higher limit for the real density since the incidental presence of micro leaks (as well as adsorption phenomena) yields a systematic overestimation of the density values.

3.1.2 Structural investigation: synchrotron powder diffraction

The X-ray powder diffraction experiments were performed at ESRF (European Synchrotron Radiation Facility, Grenoble, Fr.) in the beamline ID31. Thanks to the high resolution of the diffractometer it was possible to resolve the peaks in the central region of the spectra (see figure 38). Then, the structural study started from the indexing of the powder reflections extracted from the data collected at room temperature: the Le Bail pattern decomposition provided the cell parameters $a = 32.050(2)$ Å, $b = 10.4469(5)$ Å, $c = 9.9913(8)$ Å (orthorhombic cell with space group $Imma$).

The peaks intensities, which are directly related to the disposition of the molecules in the unit cell, in this case, are mainly influenced by the C_{60} positions; thus, starting from a fragment of the structure (four fullerenes in the unit cell), the simulated annealing (see paragraph 2.3.2) found out the arrangement of fullerenes. The C_{60} molecules showed an extremely short distance between the closest buckyballs ~ 9 Å (see figure 39a), which, certainly, suggest the

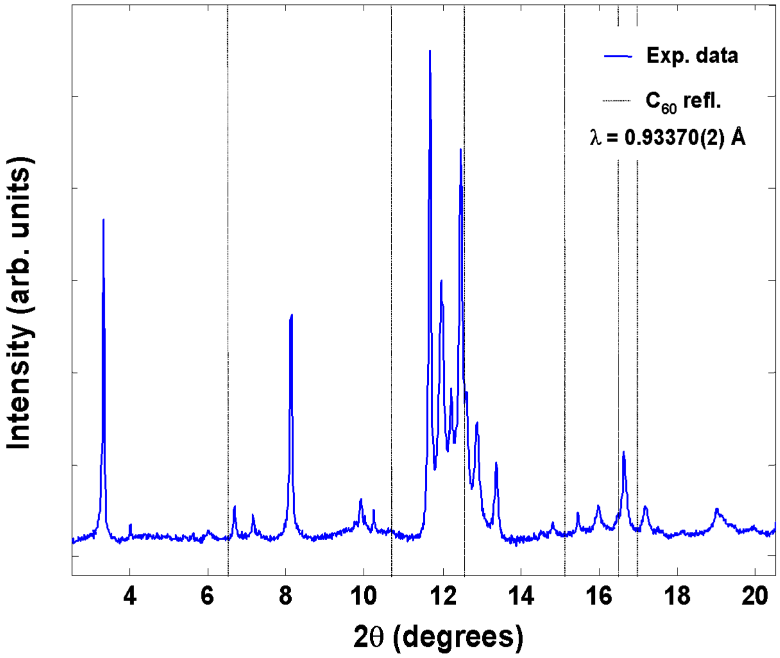

Figure 38: Synchrotron powder diffraction on $C_{60}(AsF_6)_2$.

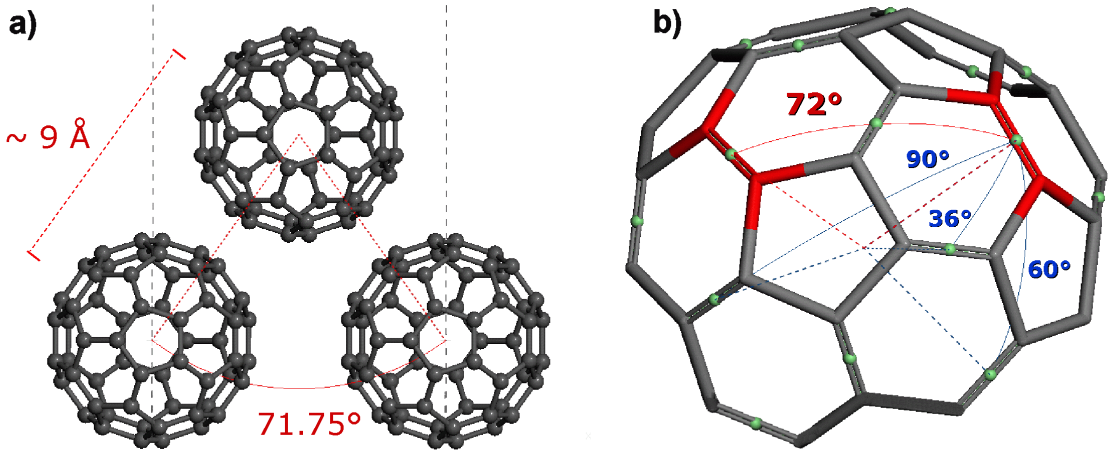

Figure 39: a) C_{60} molecules arrangement in $C_{60}(AsF_6)_2$. Polymerization is strongly encouraged by the extremely short distance between the closest buckyballs ∼ 9 Å; for the first time in the C_{60} compounds a *zigzag* arrangement of the fullerene units is observed. b) Polymerization occurs throughout the couple of *double bonds* forming angles of 72 degrees on the C_{60} cage.

structure polymerization. Moreover, to a first sight, it was not so straightforward how the polymerization could take place: surprisingly the fullerene units form a *zigzag* arrangement where the angle between closest buckyballs turns out to be $\sim 72°$(figure 39a). Indeed, taking a closer look to the fullerene molecule, we noticed that the same angle appears between a couple of so called *double bonds* on the C_{60} cage (see figure 39b).

This observation indicates that the polymerization occurs in the form of [2+2]-cycloaddition along the identified direction of the *double bonds*: C_{60} molecules are connected by double bonds and display a *zigzag* arrangement in separated chains. It is, by all means, a unique feature which has never been observed so far, in the family of the C_{60} polymers.

3.1.3 Structural investigation: low temperature ^{13}C NMR

Nuclear magnetic resonance is an important tool, helping the structural investigation of new materials: it provides information both on molecular dynamics, as it will be widely discussed in the paragraph 3.1.5, both on the structure itself, being sensitive to the electronic background of the NMR nuclei. In the case of the ^{13}C nucleus (having zero quadrupolar moment), structural informations are mainly provided by the chemical shift tensor, because it represents the direct shielding effect of the valence electrons to the coupling between the nuclear spins and the external magnetic field.

In particular the C_{60} chemical shift tensor parameters (see paragraph 2.1.6.2) are $\sigma_{11} = 33\,ppm$, $\sigma_{22} = 182\,ppm$, $\sigma_{33} = 213\,ppm$ [104] which result in $\sigma_{\text{iso}} = 143\,ppm$, $\sigma_{\text{aniso}} = 70\,ppm$ and $\eta_{CS} = 0.28$, where σ_{iso}, σ_{aniso} and η_{CS} are respectively the *isotropic chemical shift*, the *anisotropic chemical shift* and the *asymmetry* of the chemical shift, defined in equation

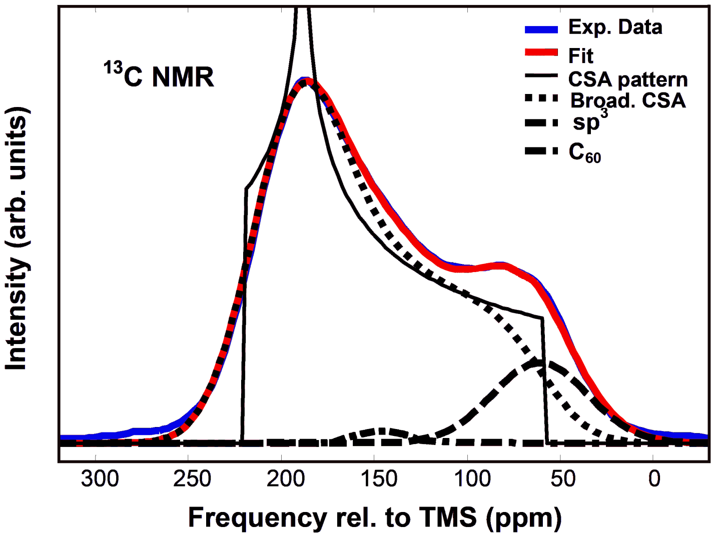

Figure 40: ^{13}C NMR on $C_{60}(AsF_6)_2$ at 80 K.

30. In the A_3C_{60} fullerides the motional narrowing of the molecules at room temperature average to zero the anisotropic features of the C_{60} chemical shift. Upon cooling the molecular dynamics blocks so that at temperature below 80 K it is possible to observe, with ^{13}C NMR experiments, the anisotropic lineshape due to the chemical shift tensor.

Since the icosahedral symmetry of the C_{60} molecule is preserved in the fullerides, thanks to the molecular nature of the solid, all the carbon atoms display the same chemical shift tensor: they are chemically equivalent. On the contrary, in the C_{60} polymers the fullerene units are blocked even at room temperature because of the constraints fixed by the bonds: moreover the distortion of the buckyballs induced by the polymerization, breaks the chemical equivalence of the carbon atoms. A slight modification of the chemical shift tensor is expected for the sp^2 atoms in the distorted C_{60} cage, while the sp^3 hybridized carbons involved in the polymer bonds are expected to display a chemical shift tensor completely different from the one of the carbons in pristine C_{60}. In particular the sp^3 anisotropy is expected to be negligible with respect the anisotropy of sp^2 carbon atoms [78]. With the aim to measure the modified chemical shift tensor of the sp^2 carbons in the cation C_{60}^{2+} as well as to identify the contribution coming from the sp^3 hybridized carbons, ^{13}C NMR measurements have been performed.

The strong signal enhancement at low temperature, due to the Boltzmann factor, prompted us to perform the ^{13}C NMR experiments at 80 K with the aim both to better acquire the weak carbon signal (natural ^{13}C abundance ~1%), and to freeze the possible residual dynamics.

The anisotropic lineshape at 80 K showed features typically observed in the C_{60} polymerized phases [78]; it was fitted taking into account three contributions:

1. the chemical shift tensor relative to the sp^2 carbon atoms of the C_{60}-cage;

2. a Gaussian peak relative to sp^3 hybridized carbons, as it is expected to observe in polymerized C_{60} systems, where the C_{60} molecule is distorted in correspondence to the carbon atoms involved in the polymeric bonds;

3. unreacted C_{60} at about 143 ppm.

The contribution of the third term is negligible (see figure 40); the fitted tensor parameters are $\sigma_{11} = 67.6 \pm 0.7\ ppm$, $\sigma_{22} = 195 \pm 2\ ppm$, $\sigma_{33} = 213 \pm 2\ ppm$, thus, $\sigma_{\text{iso}} = 158.9 \pm 2\ ppm$, $\sigma_{\text{aniso}} = 54.2 \pm 3\ ppm$ and $\eta_{CS} = 0.194 \pm 0.002$.

Based on the isotropic chemical shift, together with the chemical shift anisotropy, it is possible to easily distinguish sp^2 carbons from sp^3 carbons. Thanks to the much smaller anisotropic part of the sp^3 shift tensor with respect to the sp^2 anisotropy [78], in our case the sp^3 contribution has been fitted with a Gaussian term: its center turned out to be 57 ppm,

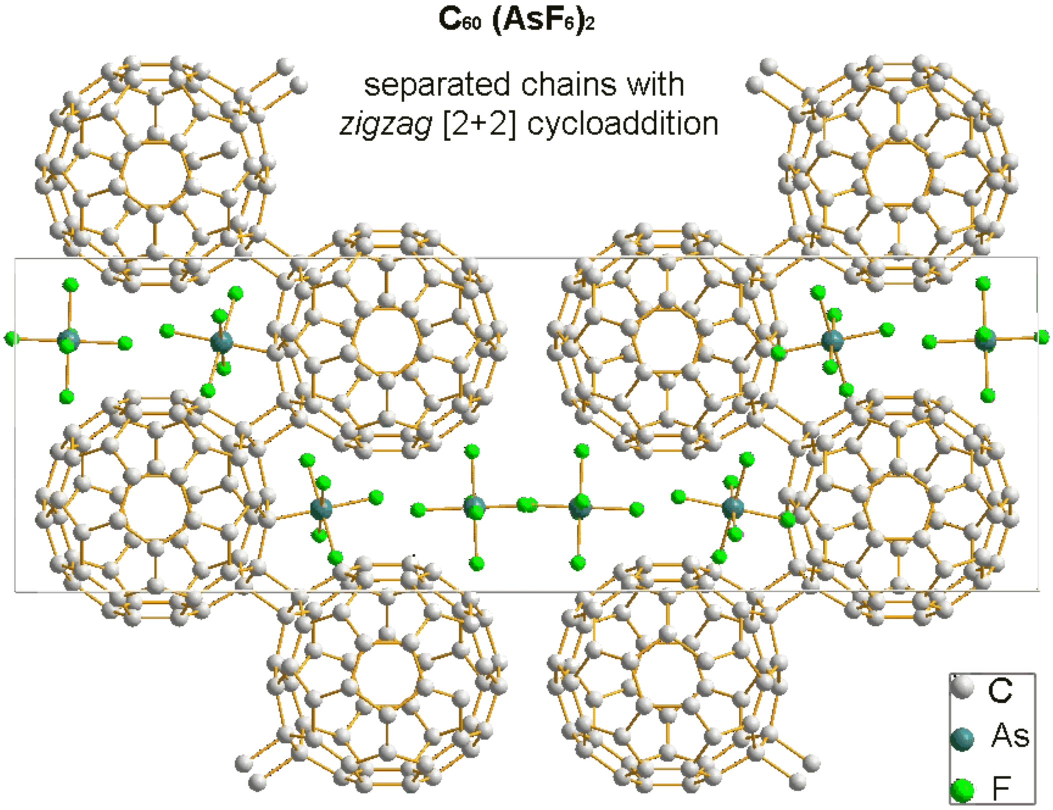

Figure 41: Refined structure of $C_{60}(AsF_6)_2$

which is consistent with the reported range for sp^3 carbon isotropic chemical shift in solids, 0-70 ppm [78].

A further, quantitative, confirmation of the polymeric nature of $C_{60}(AsF_6)_2$ came from the analysis of the spectral intensities: the integrated NMR intensities are directly proportional to the number of carbon atoms contributing to the NMR signal, thus, a direct evaluation of the intensity ratio sp^3/sp^2 carbons was performed yielding the result of 4.1 ± 1 sp^3 carbon per fullerene unit.

Although the accuracy of the fitting routine does not allow a more precise determination of such a ratio, the found value points on the confirmation of the [2+2]-cycloaddition .

The refined structure of the fullerenium salt $C_{60}(AsF_6)_2$ is reported in the figure 41; the calculated density turned out to be 2.2 g/cm^3, which is consistently lower than the measured value. However, the extreme proximity between the closest AsF_6^- ions required further analyses: in the next paragraph the possible formation of the ion $As_2F_{11}^-$ is investigated.

3.1.4 Structural investigation: ^{75}As NMR

Taking a closer look to the $C_{60}(AsF_6)_2$ structure, shown in figure 41, the extreme proximity of the AsF_6^- ions appeared immediately evident: the distance of the closest fluorine atoms between two different ions may result ~ 1.43 Å, which is compatible with the typical values of the bond lengths. Due to that reason, the incidental presence of $As_2F_{11}^-$ ions in the intercalation sites becomes realistic, thus, it was taken into account.

In order to confirm the exclusive presence of AsF_6^- ions in the structure, solutions of $C_{60}(AsF_6)_2$ were prepared suspending a few milligrams of powder in water and performing a ultra-sonic treatment. ^{75}As NMR measurements were performed at room temperature (RT) on these water solutions: the RT ^{75}As NMR spectrum is shown in figure 42: the peaks septet represents the hallmark of the J-coupling interaction (see paragraph 2.1.6.5) between the arsenic nucleus and the six equivalent fluorine atoms of the AsF_6^- ion. This particular NMR pattern is strongly related to the ion symmetry, thus, the corresponding J-coupling spectrum of $As_2F_{11}^-$, due to its strong deviation from spherical symmetry, is expected to be completely different, in particular characterized by a higher number of peaks as a consequence of the symmetry loss: the structures of the ions AsF_6^- and $As_2F_{11}^-$ are shown in the figure 43. In conclusion, no indications come from ^{75}As NMR data about the presence of ions species different from AsF_6^- in the solutions.

Moreover the pH measured in the solution was found to be consistent with the following reaction scheme:

$$C_{60}(AsF_6)_2 + 2\,H_2O \longrightarrow C_{60}(OH)_2 + 2\,AsF_6^- + 2H^+ \ . \tag{69}$$

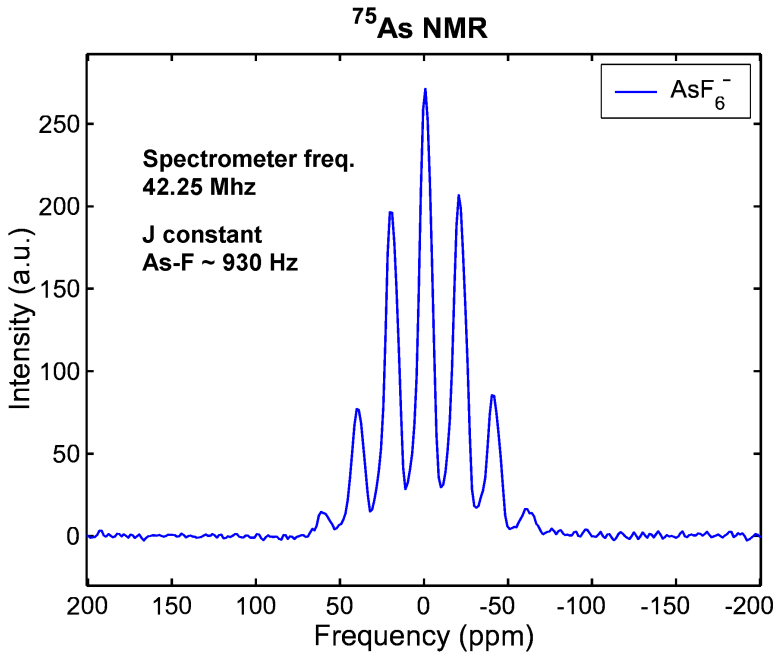

Figure 42: Room temperature ^{75}As NMR on $C_{60}(AsF_6)_2$ water solution.

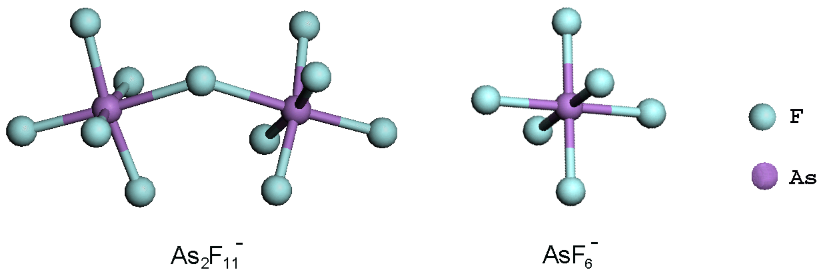

Figure 43: Structure of the ions AsF_6^- and $As_2F_{11}^-$

The pH measurement confirms the presence of the cation C_{60}^{2+}. Furthermore, based on this information together with the ^{75}As NMR spectrum showing the j-coupling interaction exclusively for the AsF_6^- ion, the hypothesis on the formation, in the solid state phase, of the counter-ion $As_2F_{11}^-$ can be excluded because, in this case, the lower C_{60} oxidation state (C_{60}^{1+}) results in a higher pH value contradicting the experimental result.

3.1.5 AsF_6^- dynamics vs. temperature: ^{19}F NMR study

Although the ^{75}As NMR provided the notable confirmation about both the presence of the AsF_6^- ion and the stoichiometry of the fullerenium salt $C_{60}(AsF_6)_2$, these NMR measurements leave unresolved the problem of the extreme proximity of the ions, hinting, thus, to a more complicated phenomenology with respect to the one taken into account.

To shed more light on the behaviour of the AsF_6^- ions, ^{19}F NMR measurements were performed from room temperature down 5 K, close to the temperature of liquid helium, in order to find out the temperature evolution of the AsF_6^- dynamics. Figure 44 shows the temperature evolution of the ^{19}F NMR spectrum: the linewidth presents only a small increase as far as the temperature reaches 70 K, while it changes abruptly at about 30 K (figure 45); in the temperature region 5 - 30 K, once more, it does not show significant changes.

The first consideration we could do on the ions dynamics is to confirm the presence of rotational motion at RT; it seems as well that the temperature, where the RT dynamics blocks almost completely is 30 K. Simulation of the NMR powder spectrum in motional narrowing conditions appeared, thus, unavoidable in order to better understand the measurements. We expected the main lineshape contribution to be the dipolar one, due to the strong dipolar coupling constant between fluorine nuclei; in consideration of that, the powder spectra simulations were carried out taking into account only the direct dipolar interaction term.

The room temperature simulation routines were implemented in the Matlab programming language in the perspective to distinguish between the two following hypothetical rotational dynamics.

- *isotropic rotation*: In consideration of the extreme proximity between closest AsF_6^- ions in the structure of $C_{60}(AsF_6)_2$, we expect their rotational dynamics to be not

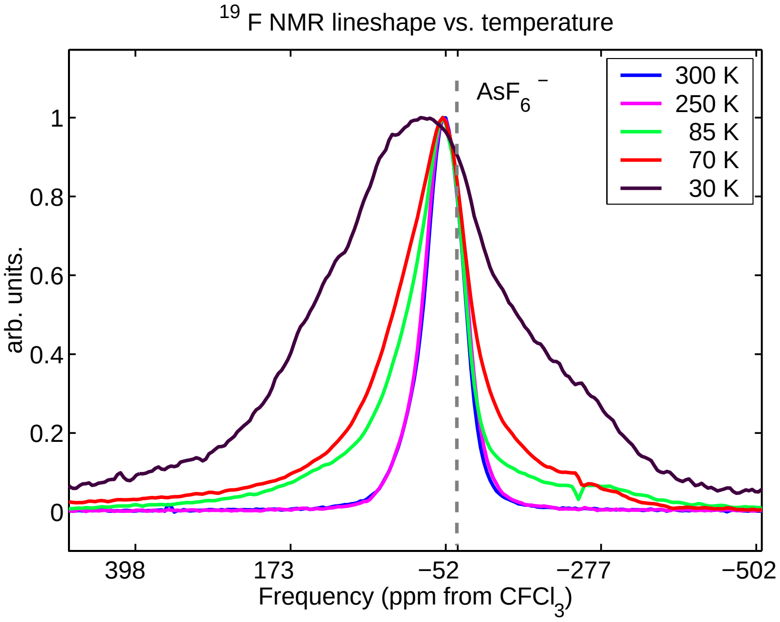

Figure 44: Temperature evolution of ^{19}F NMR spectrum of $C_{60}(AsF_6)_2$. A progressive broadening of the resonance line takes place in the temperature region 80 - 170 K. At T=30 K the asymmetry of the spectrum becomes more pronounced and the overall linewidth remains constant. The measurements were performed in a magnetic field of ~ 2.2 T

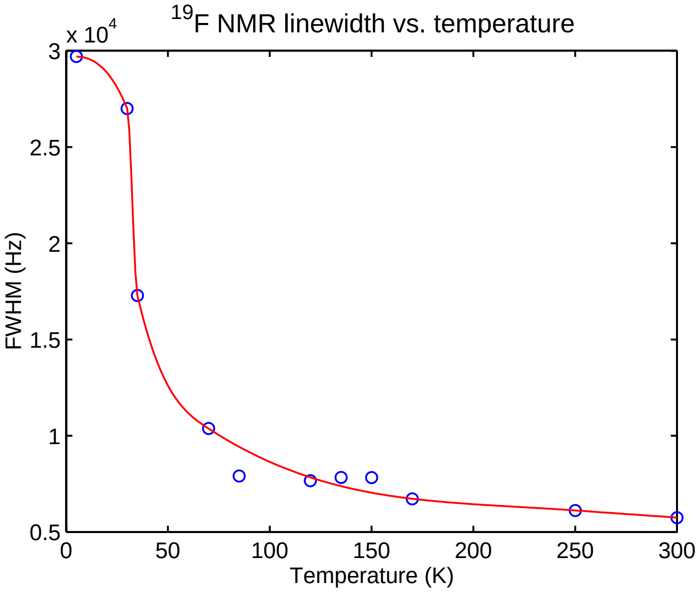

Figure 45: Temperature evolution of ^{19}F NMR linewidth of $C_{60}(AsF_6)_2$. The linewidth presents a small increase as far as the temperature reaches 70 K, while it changes abruptly at about 30 K; in the temperature region 5 - 30 K, once more, it does not show significant changes.

completely free, even at room temperature. Although the ion proximity does not yield the formation of chemical bonds, it makes the isotropic motion assumption to appear unlikely.

- *uniaxial rotation*: Due to the lack of interstitial space between the AsF_6^- ions, their isotropic motion seems to be precluded: if the ions are substituted by uniform spheres centered in the corresponding lattice positions, a non negligible intersection between closest spherical volumes appears.

  For these reasons we assumed that the rotation may occur about fixed directions; thus the rotation axes of neighbour ions constrain the reciprocal motion such as the AsF_6^- rotate "embedded" in pairs.

The simulated spin system consists in a octahedron of 6 spin 1/2, having nearest neighbours distances corresponding to the distances of the ^{19}F atoms in the AsF_6^- ion (*i.e.* 2.48 Å). The system Hamiltonian, in this case, takes into account both the term A and B of the dipolar alphabet (paragraph 2.1.6.4) for each of the 15 dipolar couplings, because, for homonuclear systems, both such terms commute with the Zeeman Hamiltonian yielding a first order contribution to the eigenvalues energies.

Powder spectra simulations were first performed, as a test for the Matlab routine, using a simple toy model formed by 3 spin 1/2 in a triangular arrangement (with equal distances). In this case the simulated spectra shows a good agreement with literature data. The references [46, 3] report on the first measurements performed over a triangular configuration of hydrogen atoms, showing in parallel the relative simulated patterns, both for static and uniaxial rotation conditions. Successively the same routine was implemented for our 6 spin 1/2 octahedron: in the static case no significant changes were introduced in the code, while in order to rewrite properly the system Hamiltonian under uniaxial rotation, the model reported in ref. [46] was generalized to the octahedral spin configuration.

Figure 46 and 47 show respectively the test simulations and the results obtained for our 6 spin 1/2 system: as expected, in both cases, the uniaxial rotation results in a partial narrowing of the resonance line.

The simulated NMR spectra, moreover, before the comparison with the experimental line, were convoluted with a Gaussian function accounting for lattice dipolar broadening: this yields a smoothing of the dipolar features, thus, the resulting line results comparable with the experimental one. Surprisingly, the best agreement between experiment and uniaxial simulation is not found at room temperature, as evident from the figure 47b, but in the intermediate temperature region (see figure 48).

In consideration of these findings the comparison between room temperature NMR spectra and the lineshape simulation in conditions of isotropic molecular motion is expected to shed more light on the structural problem related to the AsF_6^- ions proximity, responsible for this room temperature behaviour. Due to the traceless character of the dipolar tensor, the intra-molecular fluorine contribution to the NMR line is averaged to zero, in isotropic rotation conditions. The only inter-molecular dipolar broadening contributes to the spectrum yielding a Gaussian lineshape; thus, in this case, no simulations were necessary: a direct calculation of the Gaussian second moment was performed throughout the *method of moments* described in the paragraph 2.1.6.4. However, the application of the Van - Vleck formula [107], in this case, requires a further generalization [30,4] resulting in the following modification [97] of the equation 45:

$$M_{2\,homonuclear} = \mathbf{N}\,\frac{3}{5}\gamma^4\hbar^2 I(I+1)\sum_k \frac{1}{r_{j,k}^6}\,, \tag{70}$$

where I is the fluorine spin, the factor $\mathbf{N}$, arising from the model described in ref. [30], represents the number of active spin 1/2 in the molecular unit (in the case of AsF_6^-, $\mathbf{N}$=6). The summation is performed on the lattice position corresponding to the ion centers (in this particular case, the arsenic positions).

Figure 49 shows the comparison between the calculated Gaussian broadening and the experimental line at room temperature: a better agreement appears with respect to the previous case, suggesting, thus, a complex interpretation of the AsF_6^- ions behaviour. The AsF_6^- ion rotation can not be completely isotropic, as previously described: a uniaxial rotation together with a slower reorientation of the rotation axes may occur at room temperature. In this case the overall effect of the motion results in a further narrowing of the resonance line. Further-

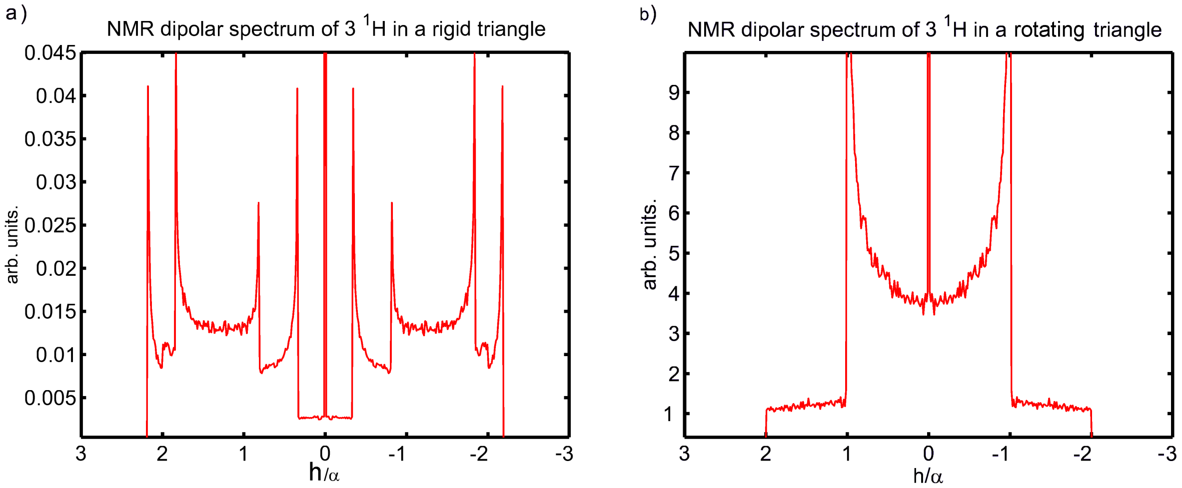

Figure 46: NMR powder spectrum simulations for an equilateral triangular spin 1/2 configuration. The NMR spectra of three hydrogen nuclei with relative distance R equal to 1.79 Å are simulated in the following cases: a) rigid triangle, b) rigid triangle rotating about the normal to its plane. For easier comparison with literature [3] the x-axis is reported in h/α, where h is the dipolar linewidth expressed in Gauss and $\alpha = \frac{3}{4}\frac{\gamma_H \hbar}{R^3}$

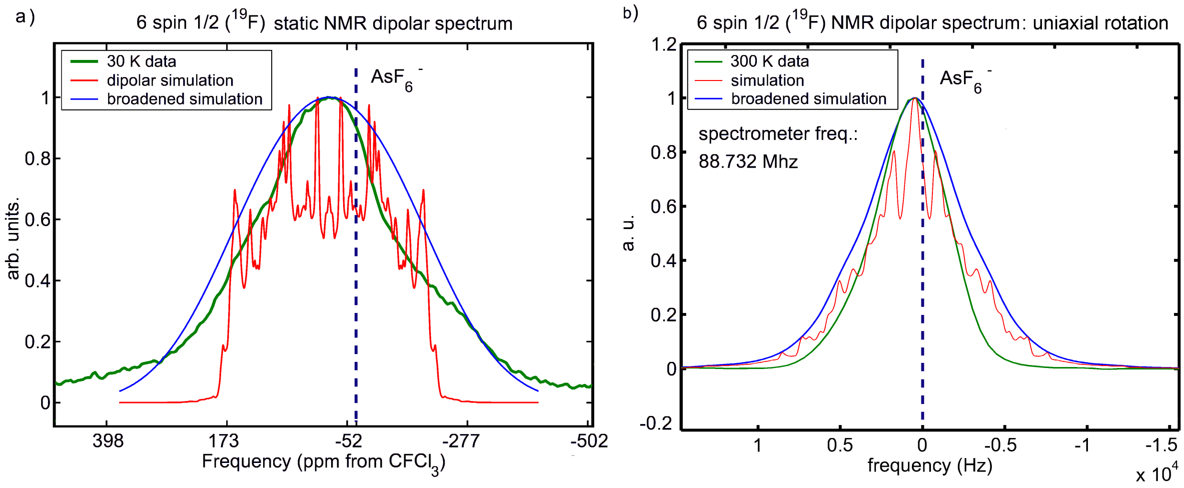

Figure 47: ^{19}F NMR powder spectra simulations. The dipolar powder spectrum for an octahedral configuration of 6 spin 1/2 has been simulated in the following cases: a) rigid spin system; b) rigid octahedron rotating about one of its principal axis. The powder average is carried out using a uniform random distribution of orientations on a sphere.

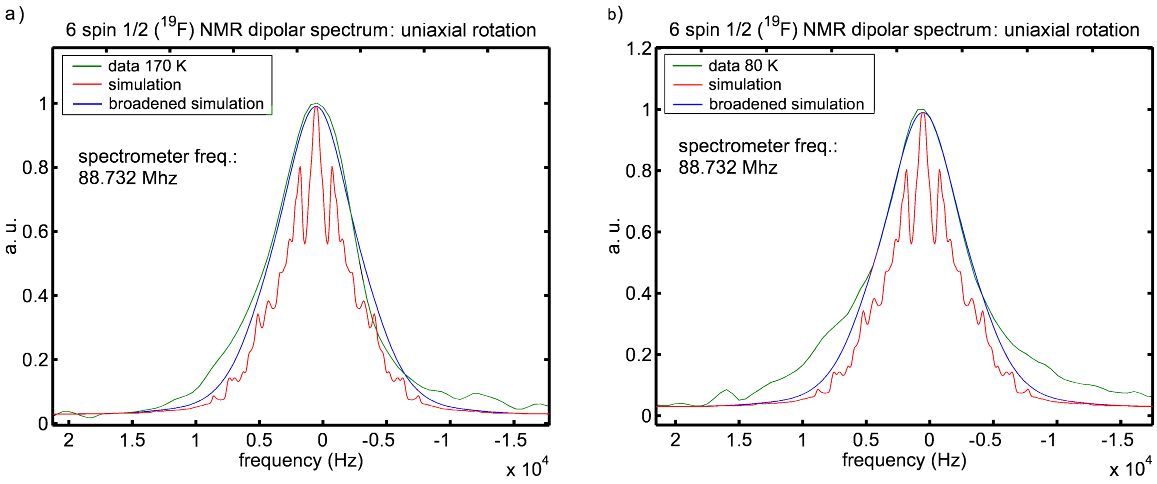

Figure 48: The dipolar powder spectrum simulated for an octahedral configuration of 6 spin 1/2 has been compared also with ^{19}F NMR measurements performed in the temperature region between 30K and 250K. A significant agreement with calculation was found for the reported temperatures 170 K (a) and 80 K (b), even if, in the latter case, the baseline shows a consistent broadening. The simulated lineshape is convoluted with a Gaussian distribution having standard deviation Δ (see paragraph 2.1.6.4) $\sim$ 1200 Hz.

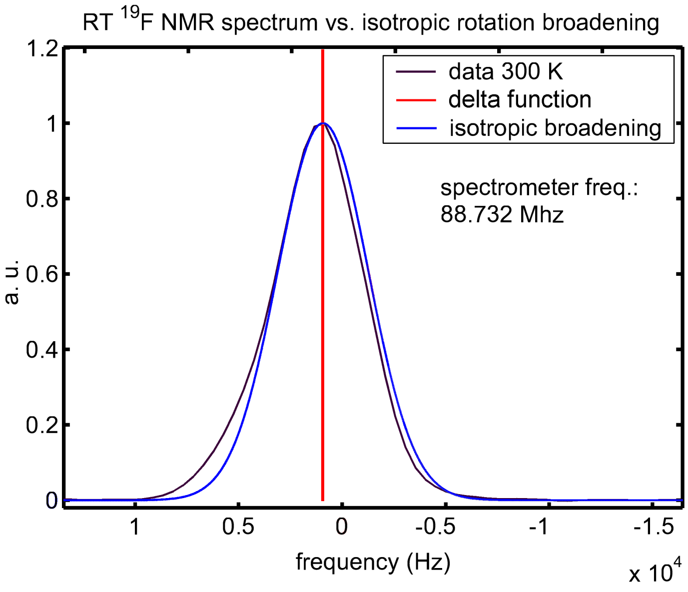

Figure 49: Room temperature ^{19}F NMR vs. dipolar broadening from isotropic rotation of AsF_6^-. The blue solid line results from the Gaussian convolution of a delta function (red solid line), the second moment being calculated with the generalized *Method of Moments* (see text). The derived value for the standard deviation of the Gaussian distribution resulted $\sim$ 2200 Hz: from a comparison with the simulations shown in figure 47 at room temperature, a better agreement is found between calculation and experiment in the assumption of isotropic rotation of AsF_6^- ions.

more, the slight increase of the FWHM in the temperature range 70-180 K can be ascribed to the progressive blocking of the axes reorientation upon cooling. This characteristic behaviour, indeed, encourage a more uniaxial rotational dynamics in the mentioned temperature region.

In parallel to the room temperature investigation of AsF_6^- ions dynamics, rigid lattice second moment calculations were performed through the *Method of Moments* [1,99] in order to estimate the homonuclear ^{19}F-^{19}F broadening in $C_{60}(AsF_6)_2$ at low temperature ($T \leq 30$ K). A reasonable result turned out to be about 10000 Hz: although the calculation is strongly dependent on the relative AsF_6^- positions due to the ions proximity, this result can explain the origin of the low temperature line width (figure 47a), even if the asymmetry of the experimental line con not be accounted by dipolar simulations. A more complicated phenomenology seems to arise for temperatures below 30 K: the detailed study of the low temperature lineshape is in progress.

3.1.6 Magnetic properties of $C_{60}(AsF_6)_2$

The magnetic behaviour of the fullerenium salt $C_{60}(AsF_6)_2$ was characterized with SQUID magnetometry. The measurements were performed in our Quantum Design SQUID magnetometer applying fields up to 5 Tesla. SQUID data were fitted with a Curie-Weiss function and a temperature independent component. The magnitude of the Curie-Weiss constant (0.0529 ±2 emu K/mol) leads to the conclusion that the compound is diamagnetic with paramagnetic impurities (one electron spin per ~ 7 formula units).

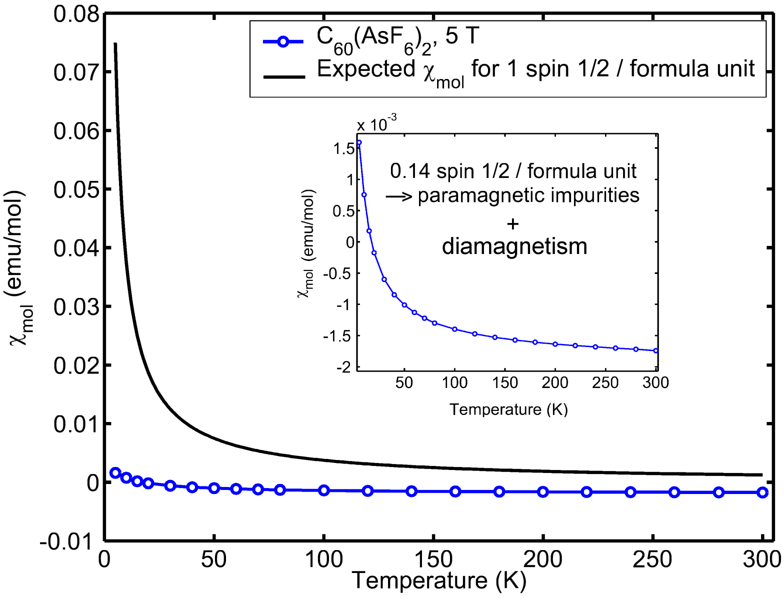

Figure 50: Molar susceptibility in a field cooling measurement at 5 T for a sample of $C_{60}(AsF_6)_2$. The data show a diamagnetic behaviour with a small contribution from paramagnetic impurities (0.14 spin $\frac{1}{2}$ / formula unit).

If the fullerides-like band structure (see paragraph 1.3) were kept in this compound, such a diamagnetic behaviour would prove that for the C_{60}^{2+} cation the Jahn-Teller energy (which prompts for a singlet state) dominates on the Hund's energy (favouring a triplet state). However, due to the polymeric nature of this fullerenium salt, the C_{60} units are sensibly distorted from the icosahedral symmetry of the isolated molecule, mainly in correspondence of the polymer bonds. Consequently the symmetry loss lifts the molecular orbital degeneracy which is essential for the onset of strongly correlation effects: the formation of a fulleride-like band structure is hampered by the polymerization which tends to localize the electrons originating insulating compounds.

The diamagnetism found in $C_{60}(AsF_6)_2$ arise, thus, from the insulating nature of the polymer.

3.2 Lithium Phthalocyanines

The investigation of transition metal-phthalocyanines in the bulk phase (strongly encouraged by the results described in the section 1.2), under alkali atom doping, was initially focused on CuPc, in order to obtain the lithium intercalation of this phthalocyanine; however, the experimental efforts profused in this direction did not have success.

During the solid state reaction an undesired effect takes place: the alkali atom substitutes the central metal in the phthalocyanine core. In our case, the lithium doping promotes the

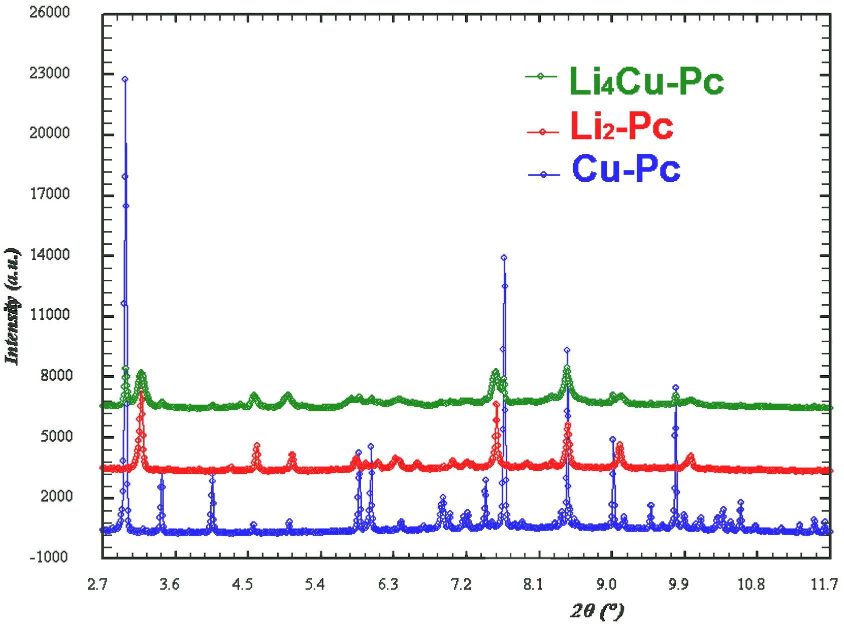

Figure 51: XRD analysis of CuPc lithium intercalation

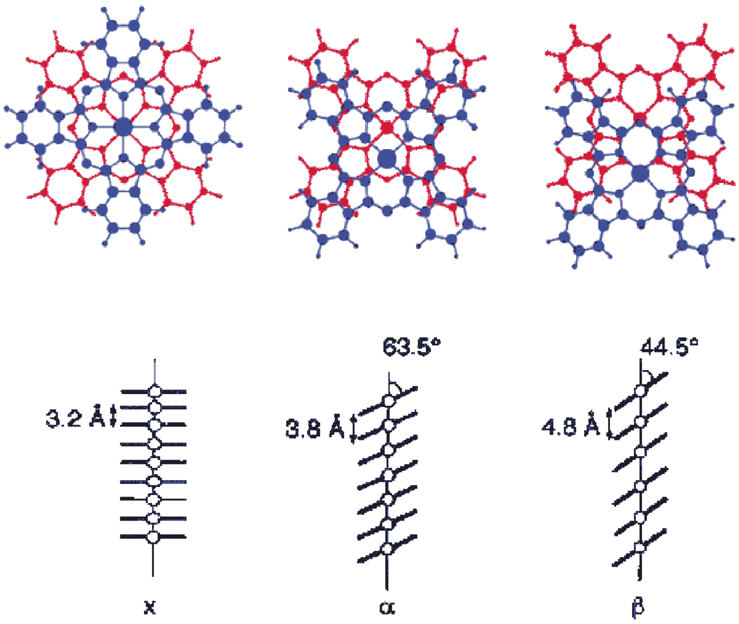

Figure 52: Molecular stacking modes in the X-form, α-form and β-form of LiPc. Adapted from ref. [102, 15].

formation of Li_2Pc, yielding the segregation of Cu in a metallic phase. Figure 51 shows the X-ray diffraction spectrum of the reaction products: a strong intensity decrease is evident for the peaks corresponding to the pure CuPc phase, while the opposite situation occurs for the reflections of Li_2Pc; for higher 2θ values characteristic peaks of the metallic Cu are also present. We decided, thus, to study MPc-s made with alkali metals (lithium) in the perspective of doping with the same alkali metal present in the core of the phthalocyanine. This new approach was motivated by the necessity to overcome the above reported problem related to the competition between transition metals and alkali metals in filling the phthalocyanine core.

The experimental efforts were dedicated to the study of lithium phthalocyanines LiPc and Li_2Pc, as anticipated in the paragraph 1.2.2. The interest in LiPc characterization lies in the radical nature of the molecule yielding an intrinsic magnetic behaviour due to the unpaired electron in one nitrogen atom. On the contrary Li_2Pc was studied upon lithium doping in the perspective to induce a transition to a metallic phase, as reported on thin films [23].

3.2.1 Magnetic characterization of LiPc

LiPc presents three polymorphic forms reported in the literature as α, β, and X polymorphs (figure 52). We synthesized LiPc starting from ortho-dicyanobenzene and lithium iodide, with a chemical reaction performed at 250 °C as described in the references [15, 54]:

$$8\ \mathrm{ODCB} + 2\ \mathrm{LiI} \xrightarrow{250^\circ\mathrm{C}} 2\ \mathrm{LiPc} + \mathrm{I}_2 \uparrow \tag{71}$$

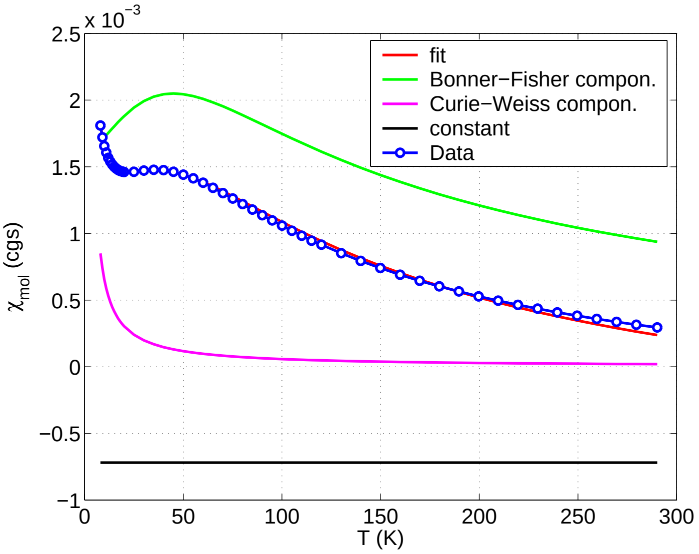

Figure 53: Molar susceptibility of β LiPc in 1 T fitted with a mean-field modification of Bonner-Fisher 1-D AFM chain model to take into account also a weak inter-chain coupling. Adapted from ref. [9]

A mixture of the three different polymorphs is obtained: it is possible to separate the different phases with a sublimation process performed under vacuum at 400°C [9]: after the treatment the sublimated powder results mainly formed by the α polymorph, while the unsublimated powder is mainly composed by β phthalocyanine.
The structural analysis of these α and β polymorphic forms was performed in the Ph.D. thesis of Dr. Daniele Pontiroli [88], while the magnetic properties of LiPc have been widely studied with SQUID magnetometry in the Ph.D thesis work of Dr. Matteo Belli [9]; in the present paragraph I remind the main result regarding the polymorph β and I present its μSR characterization performed at ISIS (Rutherford Appleton Laboratory, Chilton, UK) on the EMU beamline.

The susceptibility for the β polymorph, showed the characteristic temperature behaviour which was fitted with a *modified* Bonner-Fisher (B-F) model [13] associated to a Curie-Weiss contribution coming from paramagnetic impurities; the amount of ferromagnetic impurities resulted negligible. The cited B-F model consists in a one-dimensional antiferromagnetic intra-chain coupling, while the coupling between adjacent chains is assumed negligible. In this case, however, the impossibility to fit properly our experimental data with the simple B-F model makes the assumption of 1-D coupling to appear not strictly justified for LiPc. The occurrence of a weak inter-chain interaction was taken into account with a first order molecular field correction, as outlined by Estes *et. al.* [37]. Figure 53 shows how the fitted curve presents a good agreement with data; the detailed description of the modified B-F model can be found in ref. [9].

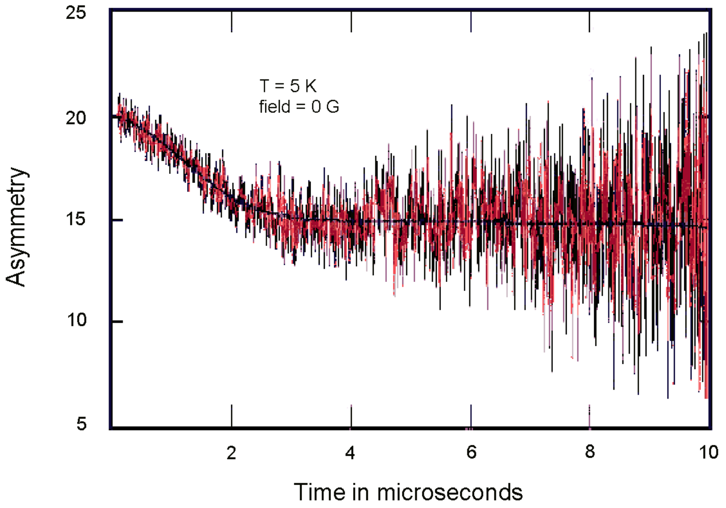

Figure 54: Example of a ZF-μSR measurement at low temperature (T $<$ 45 K). No oscillations related to the presence of a local field due to a magnetically ordered state is detected.

In low temperature conditions the contribution of the weak inter-chain interactions yields a 2-D coupling (intra-chain + inter-chain) which may present magnetic ordering (impossible in 1-D coupled systems). In consideration of these findings, μSR experiments in zero field conditions (ZF, see paragraph 2.4.1) were performed in order to better investigate the behaviour of the inter-chain magnetic coupling. The presence of a ferromagnetic coupling, however is ruled out by the SQUID results: the ferromagnetic signal would be easily detected by the bulk magnetometry technique. On the contrary the presence of an antiferromagnetic coupling can be more properly investigated only with μSR, probing the microscopic local fields (see paragraph 2.4.1). Thus, If an antiferromagnetic ordering occurs at low temperature, the onset of a characteristic oscillating μSR signal is expected, as a result of the muons precession in the local field.

The experimental results are shown in figure 54: the data fitting was carried out with the routine *Wimda* using Gaussian functions: the Gaussian relaxation found can be ascribed to the effect of dipolar broadening from a rigid spin lattice without magnetic ordering.

In conclusion μSR experiments ruled out the presence of a consistent inter-chains coupling at low temperature, because no magnetically ordered state is observed down to 2 K. LiPc, in its β polymorphic phase, represents thus a good example of 1-D coupling even in low temperature conditions.

3.2.2 Structural and electronic properties of Li_2Pc

Li_2Pc (see figure 55) is commercially available, thus it was purchased from *Sigma Aldrich*, and required a re-sublimation at high temperature to improve the crystallinity and increase

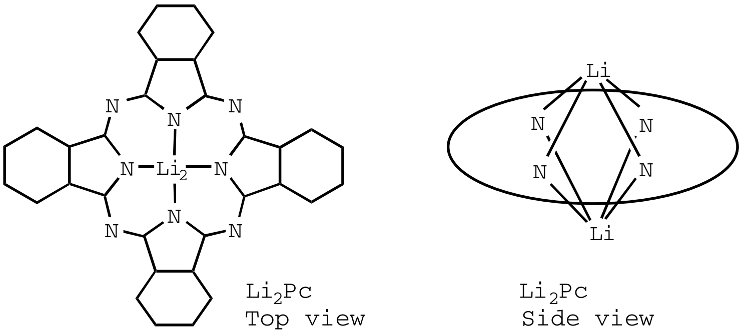

Figure 55: Top and side view of the Li_2Pc molecule. The latter shows as both the Li atoms are shifted from the plane of the molecule (LiPc on the contrary remains an almost planar molecule). Adapted from ref. [68].

the purity of the material. The crystal structure of pure Li_2Pc had never been observed experimentally so far, but only predicted theoretically. It turns out to be again different from the polymorphs of the radical LiPc so that it has been referred to as ϵ phase. Figure 56 shows the Le Bail pattern decomposition of the synchrotron radiation X-rays data collected at ESRF. The unit cell parameters are: a = 18.37 Å, b = 5.14 Å, c = 14.09 Å, β = 118.16°, being β the angle between the x and z axes. From the simulated annealing procedure the resulting chains packing occurs along the y direction yielding a 40° stacking angle (see figure

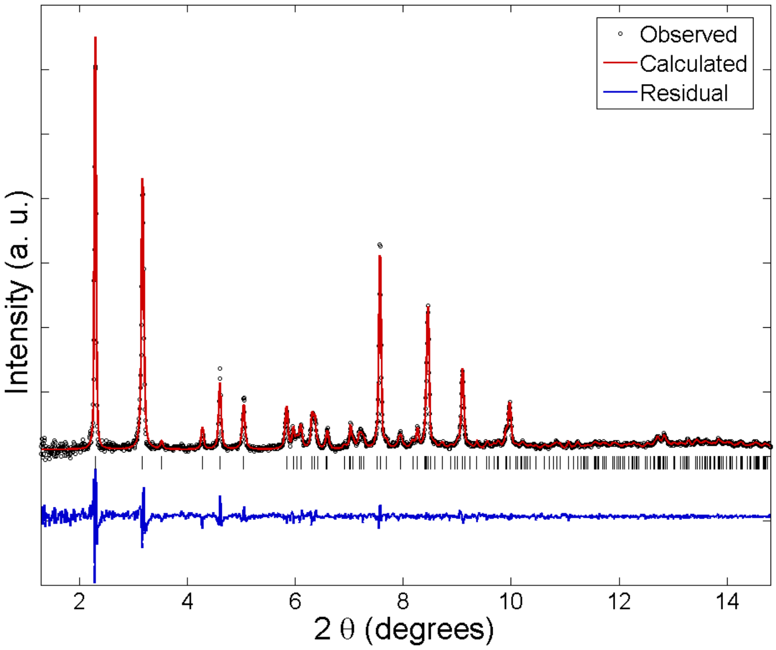

Figure 56: Li_2Pc X-rays diffraction pattern with synchrotron radiation (ESRF, BM1B). The refined cell parameters are: a = 18.37 Å, b = 5.14 Å, c = 14.09 Å, β = 118.16° (R_{wp} = 7.84 %).

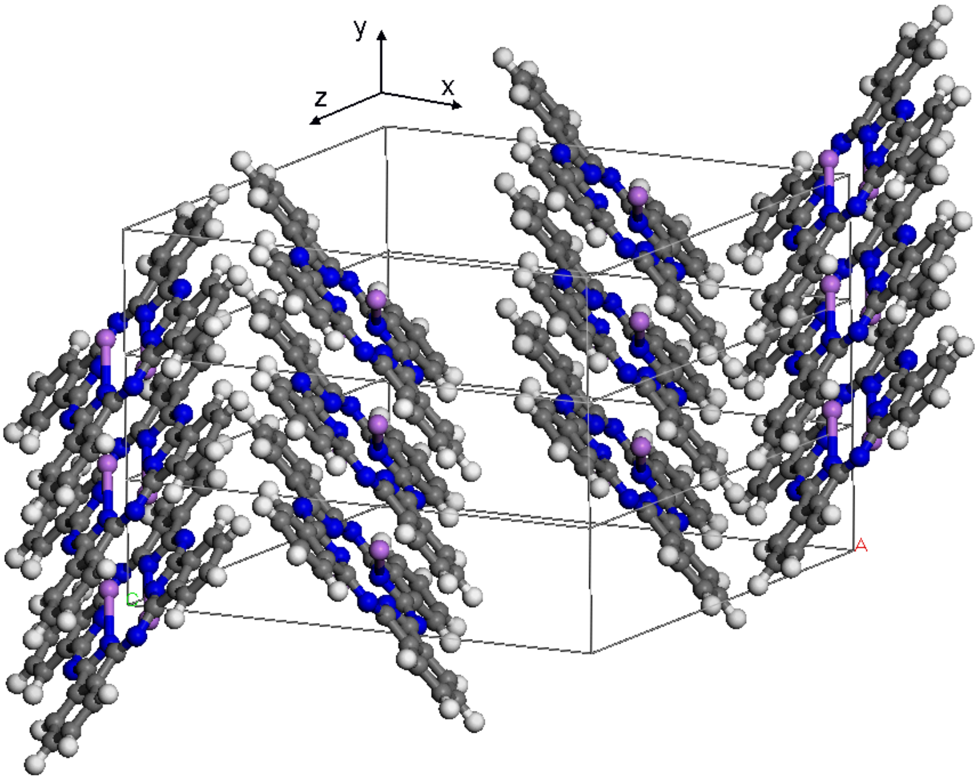

Figure 57: Li_2Pc stacking. The stacking angle is 40.02° (formed by the molecules with the y-axis).

57).

Lithium intercalation of Li_2Pc: Li_2Li_2Pc and Li_3Li_2Pc

The alkali atom intercalation in the bulk phthalocyanine structure occurred by means of a solid state reaction where the LiPc powder, mixed with lithium azide, LiN_3 (also in powder form) undergoes a thermal treatment. Metal azides, in general, are metastable compounds which easily react or explode returning nitrogen gas and the metal separately: azides stability is strongly dependent on the metallic species involved. In the case of lithium azide the reaction takes place in a safe mode during a slow ramp thermal treatment. The thermal decomposition of LiN_3 promotes the intercalation of lithium atoms in the phthalocyanine powder. Figure 58 shows the monitored temperature and pressure: the azide decomposition is evidenced by the presence of a pressure peak due to the nitrogen gas. The XRD analysis performed on the synthesized Li_2Li_2Pc and Li_3Li_2Pc suggest that the Li_2Pc structure is preserved only with small variations of the cell parameters as shown in figure 60.

Finally, the electronic properties of Li_2Pc, Li_2Li_2Pc and Li_3Li_2Pc were characterized with SQUID magnetometry measurements. In the case of the doped phases, we expected respectively two and three electrons to be transferred from the doping lithium atoms to the

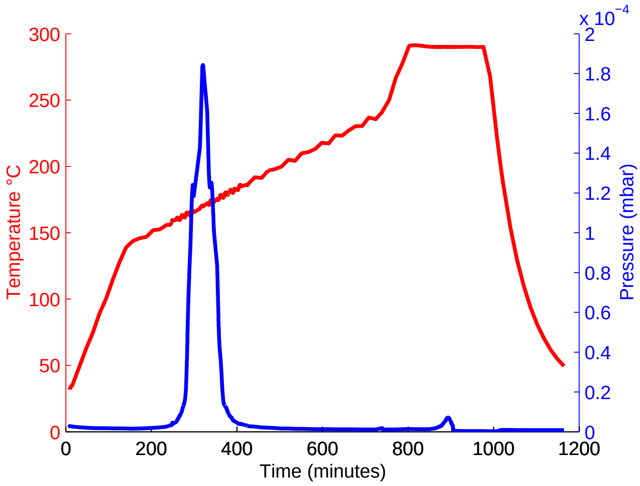

Figure 58: Thermal treatment on Li_2Pc. The pressure peak indicates the lithium azide decomposition.

LUMO level of Li_2Pc which shows double degeneracy (see figure 59) as reported for other phthalocyanines (paragraph 1.2.1). The ground state geometry as well as the absorption spectra of Li_2Pc have been calculated by Liu *et. al.* using the time dependent density functional theory (TDDFT): the excitation energy between the HOMO $2a_{1u}$ and LUMO $6e_g$ orbitals turned out to be 2.02 eV in good agreement with the experimental value 1.89 eV [68].

The SQUID magnetometry results are shown in figure 61: the most diamagnetic behaviour is observed in Li_2Li_2Pc, where the LUMO orbital is half filled, having two electrons. Taking as a reference compound the undoped Li_2Pc, slightly diamagnetic, we outline that its intercalated new phases show a more diamagnetic response with respect Li_2Pc. Moreover it appears surprising that the most diamagnetic compound turns out to be Li_2Li_2Pc, which, in principle, is the best candidate for the onset of a metallic state.

So far we can not conclude if a contribution from the Pauli paramagnetism is also present in these new compounds, since, although the phthalocyanine core diamagnetism does not change as a consequence of the lithium intercalation, on the contrary, the Van Vleck paramagnetism is strongly influenced by the electron transfer in the phthalocyanine molecular orbitals, and the possible presence of a Van Vleck term has not been taken into account.

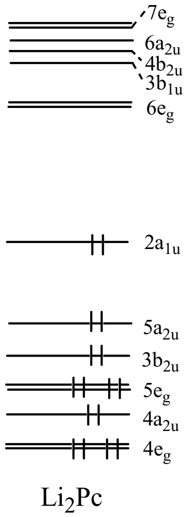

Figure 59: Molecular orbitals energy levels in Li_2Pc obtained from TDDFT calculations. Adapted from ref. [68].

The Van Vleck paramagnetism is a temperature indepen-

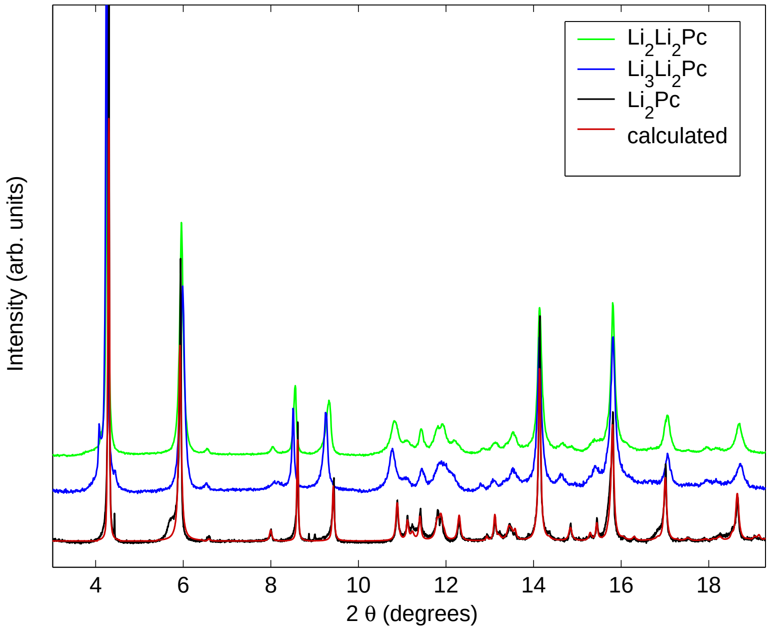

Figure 60: X-rays diffraction pattern of Li$_x$Li$_2$Pc, x=2,3. The data refinement (carried out with GSAS software suite) indicate that the Li$_2$Pc structure is preserved with small variations of the cell parameters. The Li$_2$Li$_2$Pc cell parameters are: a = 18.38 Å, b = 5.19 Å, c = 14.07 Å, β = 117.19°. In the case of Li$_3$Li$_2$Pc we found a = 18.33 Å, b = 5.21 Å, c = 14.07 Å, β = 116.58°

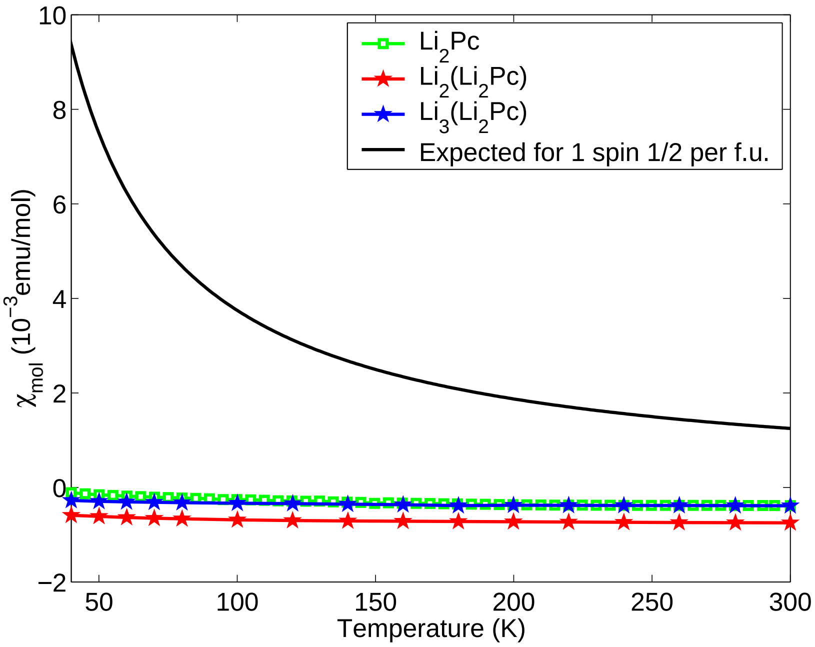

Figure 61: Molar susceptibility for Li$_2$Pc, Li$_2$Li$_2$Pc and Li$_3$Li$_2$Pc measured with SQUID magnetometry as a function of temperature.

dent positive term arising from the mixing of the molecular ground state with excited states, caused by the applied magnetic field. It assumes the form:

$$\chi_{vv} = \frac{N}{V}\,\mu_B^2\hbar \sum_n \frac{|\langle 0|L_z + gS_z|0\rangle|^2}{E_n - E_0}\,, \tag{72}$$

where μ_B is the Bohr magneton, L_z, S_z the z-components of the orbital and spin angular moments, and finally E_n the molecular n level energy ($E_n > E_0$) [12]. Its contribution is practically impossible to establish independently from the core diamagnetism: this unfortunately prevents an absolute determination of the Pauli susceptibility.

In summary the Van Vleck term may significantly influence the observed value of the measured susceptibility hindering the determination of the Pauli term, which, if present, is just a small difference among larger terms. To a first approximation, thus, we do not observe Pauli paramagnetism in the intercalated lithium-phthalocyanines; this suggest that Li_2Li_2Pc as well as Li_3Li_2 are diamagnetic insulating compounds. However the presence of a weak Pauli term can not be excluded until an evaluation of the Van Vleck term will be provided.

Conclusions

This PhD thesis work presents an investigation on new classes of strongly correlated molecular compounds whose building blocks are respectively the phthalocyanine molecule and the fullerene molecule. The interest in these new materials was motivated by both theoretical [64, 42, 103] and experimental works [23] pointing on the possible presence of a close analogy in the electronic properties between the mentioned compounds and the *fullerides*, where the C_{60} molecule is electron-doped.

At first, a preliminary study evidenced the compound LiPc and Li_2Pc as two representative phthalocyanine-based materials. Thus, in order to identify the electronic and magnetic properties, SQUID magnetometry measurements, together with muon spin relaxation (μSR) experiments have been performed on LiPc, whose radicalic character yielded, in the β polymorph, an antiferromagnetic 1-dimensional coupling which has been referred to as intra-chain coupling. The presence of weak inter-chain interactions, indicated by the SQUID analysis in the paragraph 3.2.1 [9], suggested the possibility to observe at low temperature an antiferromagnetic ordering. This possibility, however has been definitively ruled out by the μSR experiments: LiPc, in its β polymorphic phase represents, thus, a good example of 1-D coupling.

Li_2Pc has been characterized with XRD and SQUID magnetometry upon progressive lithium doping, with the aim to extend to the bulk phase the remarkable electronic properties observed in thin phthalocyanine films [23]. The new doped phthalocyanines Li_xLi_2Pc have been synthesized, with $x = 2, 3$.

In summary the individuation of a Pauli paramagnetic term (which is the hallmark of a metallic behaviour) from the SQUID data analysis is hampered by the unknown contribution of Van Vleck paramagnetism. Surprisingly, indeed, Li_2Li_2Pc, the best candidate for the onset of a metallic state, shows the highest diamagnetic behaviour. We suggest that Li_2Li_2Pc and Li_3Li_2 are diamagnetic insulating compounds, however the presence of a weak Pauli term can not be excluded until an evaluation of the Van Vleck term will be provided. Consequently, no transition to a metallic state as a function of the electron doping, can be unambiguously identified, relatively to the tested stoichiometries $x = 2, 3$.

Finally, concerning the fullerene-based molecular compounds, this work reports, 17 years

after the discovery of fullerene, on the structural and physical study of the first fullerenium salt $C_{60}(AsF_6)_2$ where the fullerene is present in the solid state with the 2+ charged state C_{60}^{2+}.
Since it is well known that C_{60} is an exceptionally good electron acceptor but also, on the other hand, a bad electron donor, the synthesis of materials in which C_{60} is present in its oxidized state is extremely difficult and, in the case of $C_{60}(AsF_6)_2$, it required the use of strong oxidants like superacids [85, 91].

Our structural investigation was carried out with synchrotron powder X-rays diffraction, gas pycnometry and ^{13}C NMR. The results show that C_{60} molecules develop interconnections through coupled intermolecular bonds (2+2 cycloaddition) in such a way to form an architecture of 1D chains with a *zigzag* arrangement which has neither been observed before experimentally nor been anticipated theoretically in the C_{60} polymers.
The C_{60} molecules, in fullerides, show at room temperature an isotropic rotational motion, while in $C_{60}(AsF_6)_2$ the fullerenes are blocked at room temperature because of the polymeric bonds. On the contrary a complicated rotational dynamics was outlined in the AsF_6^- ions, through a ^{19}F NMR study versus temperature. The competition between the thermal energy and the extreme proximity of the ions pairs does not allow complete narrowing conditions yielding a characteristic phenomenology.
SQUID magnetometry shows that this polymer is a diamagnetic insulator.

In conclusion, a remarkable future perspective has been identified in this research line focused on the fullerenium salts: the behaviour of $C_{60}(AsF_6)_2$ as a function of temperature will be intensively studied in analogy with the behaviour of the fulleride Li_4C_{60}.
At room temperature, Li_4C_{60} shows a similar 2+2 cycloaddition polymerization and undergoes a phase transition upon heating at ~ 300 °C under vacuum, yielding a monomeric state in a cubic lattice.
A similar phenomenology has been recently observed in the fullerenium salt: the formation of a new C_{60} phase which presents a *fcc* structure has been observed at ~ 300 °C. It is worth noticing that, in this case, cooling the system to room temperature does not recover the fullerene polymerization and the monomer cubic phase is preserved.
In the fullerene compounds, the high symmetry of the *fcc* cubic structure, as discussed in the paragraph 1.1.4, promotes the onset of high correlation effects resulting in a metallic behaviour.
Further investigations pointing in this direction are in progress.

Bibliography

[1] ABRAGAM, A. *The Principles of Nuclear Magnetism.* No. 32 in The International Series of Monographs on Physics. Clarendon Press, Oxford, 1983.

[2] ALLEMAND, P. M., KHEMANI, K. C., KOCH, A., WUDL, F., HOLCZER, K., DONOVAN, S., GRÜNER, G., AND THOMPSON, J. D. Organic Molecular Soft Ferromagnetism in a Fullerene C_{60}. *Science 253* (July 1991), 301.

[3] ANDREW, E. R., AND BERSOHN, R. Nuclear Magnetic Resonance Line Shape for a Triangular Configuration of Nuclei. *The Journal of Chemical Physics 18*, 2 (1950), 159.

[4] ANDREW, E. R., AND EADES, R. G. A magnetic resonance investigation of *cyclo*hexane. In *Proceedings of the Royal Society of London* (1952), vol. 216 of *series A, Mathematical and Physical Sciences*, p. 398.

[5] ANDREW, E. R., AND EADES, R. G. A nuclear magnetic resonance investigation of three solid benzenes. In *Proceedings of the Royal Society of London* (1952), vol. 218 of *series A, Mathematical and Physical Sciences*, p. 537.

[6] AUERBACH, A., MANINI, N., AND TOSATTI, E. Electron-vibron interactions in charged fullerenes. I. Berry phases . *Physical Review B 49* (1994), 12998.

[7] AXE, J. D., MOSS, S. C., AND NEUMANN, D. A. Structure and dynamics of crystalline C_{60}. In *Solid State Physics. Advances in Research and Applications* (Boston, San Diego, New York, London, Sydney, Tokyo, Toronto, 1994), H. Ehrenreich and E. F. Spaepen, Eds., vol. 48, Academic Press Limited, pp. 149–224.

[8] BARDEEN, J., COOPER, L. N., AND SCHRIEFFER, J. R. Theory of Superconductivity. *Physical Review 108* (1957), 1175.

[9] BELLI, M. Magnetic and Transport Properties of Intercalated Fullerides. *PhD Thesis* (2006).

[10] BLINC, R., SELIGER, J., DOLINŠEK, J., AND ARČON, D. Two-Dimensional ^{13}C NMR Study of Orientational Ordering in Solid C_{60}. *Physical Review B 49*, 7 (February 1994), 4993–5002.

[11] BLOCH, F. Nuclear Induction. *Physical Review 70* (1946), 460.

[12] BLUNDELL, S. *Magnetism in condensed matter.* Oxford University Press, Oxford, UK, 2006.

[13] BONNER, J. C., AND FISHER, M. E. Linear Magnetic Chains with Anisotropic Coupling. *Physical Review 135*, 3A (August 1964), A640–A658.

[14] BREWER, J. H., AND CYWINSKI, R. μSR: an introduction. In *Muon Science. Muons in Physics, Chemistry and Materials* (Bristol and Philadelphia, 1999), S. L. Lee, S. H. Kilcoyne, and E. R. Cywinski, Eds., vol. 51 of *SUSSP Proceedings, NATO ASI series*, Institute of Physics Publishing, pp. 1–10.

[15] BRINKMANN, M., TUREK, P., AND ANDRÉ, J.-J. EPR Study of the x, α and β Structures of Lithium Phthalocyanine. *Journal of Materials Chemistry 8*, 3 (1998), 675–685.

[16] BRUNO, C., DOUBITSKI, I., MARCACCIO, M., PAOLUCCI, F., PAOLUCCI, D., AND ZAOPO, A. Electrochemical Generation of C_{60}^{2+} and C_{60}^{3+} . *Journal of the American Chemical Society 125* (2003), 15738.

[17] CAPELLMANN, H. Ferromagnetism and strong correlations in metals. *Journal of Physics F: Metal Physics 4* (September 1974), 1466.

[18] CHAKRAVARTY, S., AND KIVELSON, S. A. Electronic mechanism of superconductivity in the cuprates, C_{60}, and polyacenes. *Physical Review B 64* (2001), 064511.

[19] COX, E. G. Crystal Structure of Benzene. *Reviews of Modern Physics 30*, 1 (1958), 159.

[20] COX, S. F. J. Muonium states and dynamics. In *Muon Science. Muons in Physics, Chemistry and Materials* (Bristol and Philadelphia, 1999), S. L. Lee, S. H. Kilcoyne, and E. R. Cywinski, Eds., vol. 51 of *SUSSP Proceedings, NATO ASI series*, Institute of Physics Publishing, pp. 239–286.

[21] CRACIUN, M. F., ROGGE, S., DEN BOER, M. J. L., KLAPWIJK, T. M., AND MORPURGO, A. F. Alkali Doped Metal-Phthalocyanines: a New Class of Molecular Metals. *cond-mat 0401036* (January 2004).

[22] CRACIUN, M. F., ROGGE, S., DEN BOER, M. J. L., MARGADONNA, S., PRASSIDES, K., IWASA, Y., AND MORPURGO, A. F. Doping-Induced Insulator-Metal-Insulator Transition in a Large Class of Molecular Solids. *cond-mat 0401036* (April 2005).

[23] CRACIUN, M. F., ROGGE, S., AND MORPURGO, A. F. Correlation between Molecular Orbitals and Doping Dependence of the Electrical Conductivity in Electron-Doped Metal-Phthalocyanine Compounds. *Journal of the American Chemical Society 127* (2005), 12210–12211.

[24] DATARS, W. R., CHIEN, T. R., NKUM, R. K., AND UMMAT, P. K. Intercalation of AsF_5 in C_{60}. *Physical Review B 50* (1994), 4937.

[25] DATARS, W. R., PALIDWAR, J. D., AND UMMAT, P. K. Identification of acceptors in C_{60}. *Journal of Physics and Chemistry of Solids 57* (1996), 977.

[26] DATARS, W. R., AND UMMAT, P. K. Identification of AsF_6^- in C_{60}. *Solid State Communications 94* (1995), 649.

[27] DE HEER, W. A., KNIGHT, W. D., CHOU, M. Y., AND COHEN, M. L. *Solid state physics*, vol. 40. Academic Press, New York, 1987.

[28] DE RENZI, R. μSR and NMR: fundamental concepts and selected examples. In *Muon Science. Muons in Physics, Chemistry and Materials* (Bristol and Philadelphia, 1999), S. L. Lee, S. H. Kilcoyne, and E. R. Cywinski, Eds., vol. 51 of *SUSSP Proceedings, NATO ASI series*, Institute of Physics Publishing, pp. 211–237.

[29] DE REOTIER, P. D., AND YAOUANC, A. Muon Spin Rotation and Relaxation in Magnetic Materials. *Journal of Physics: Condensed Matter 9* (1997), 9113–9166.

[30] DIMITRIEVA, L. V., AND MOSKALEV, V. V. Calculation of the Second Moment of a Nuclear Magnetic Resonance Line in Isotropic Rotation of Molecules. *Soviet Physics of the Solid State 3* (1964), 1623.

[31] DUARTE, J. P., VILãO, R. C., GIL, J. M., ALBERTO, H. V., DE CAMPOS, N. A., AND WEIDINGER, A. Muoniated Radicals in the Organic Semiconductor Zinc-Phthalocyanine. *Physica B 326* (2003), 94–96.

[32] EDÉN, M. Computer Simulations in Solid-State NMR. I. Spin Dynamics Theory. *Concepts in Magnetic Resonance Part A 17A*, 1 (2003), 117–154.

[33] EDÉN, M. Computer Simulations in Solid-State NMR. II. Implementations for Static and Rotating Samples. *Concepts in Magnetic Resonance Part A 18A*, 1 (2003), 1–23.

[34] EDÉN, M. Computer Simulations in Solid-State NMR. III. Powder Averaging. *Concepts in Magnetic Resonance Part A 18A*, 1 (2003), 24–55.

[35] ELIASHBERG, G. M. *Soviet Physics JETP V 11* (1960), 696.

[36] ERNST, R. R., BODENHAUSEN, G., AND WOKAUN, A. *Principles of Nuclear Magnetic Resonance in One and Two Dimensions*, 5th ed. No. 14 in International Series of Monographs on Chemistry. Oxford Science Publications, Oxford, 1987.

[37] ESTES, W. E., GAVEL, D. P., HATFIELD, W. E., AND HODGSON, D. J. Magnetic and Structural Characterization of Dibromo- and Dichlorobis(thiazole)copper(II). *Inorganic Chemistry 17*, 6 (1978), 1415–1421.

[38] FORRÓ, L., AND MIHÁLY, L. Electronic Properties of Doped Fullerenes. *Reports on Progress in Physics 64* (March 2001), 649–699.

[39] FUHRER, M. S., CHERREY, K., ZETTL, A., COHEN, M. L., AND CRESPI, V. Carbon Isotope Effect in Single Crystal Rb_3C_{60}. *Physical Review Letters 83* (1999), 404.

[40] GIACOVAZZO, C., MONACO, H. L., ARTIOLI, G., VITERBO, D., FERRARIS, G., GILLI, G., ZANOTTI, G., AND CATTI, M. *Foundamentals of Crystallography*, 2rd ed. Oxford University Press, 2002.

[41] GOLDSTEIN, H. *Classical Mechanics*. Addison-Wesley, Massachusetts, USA, 1965.

[42] GRANATH, M., AND ÖSTLUND, S. Superconductivity in hole-doped C_{60} from electronic correlations. *Physical Review B 66* (2002), 180501.

[43] GREGORY, P. Industrial Applications of Phthalocyanines. *Journal of Porphyrins and Phthalocyanines 4* (2000), 432.

[44] GUNNARSSON, O. Superconductivity in Fullerides. *Reviews of Modern Physics 69*, 2 (April 1997), 575–606.

[45] GUNNARSSON, O. *Alkali-Doped Fullerides Narrow-Band Solids with Unusual Properties*. World Scientific, 2003.

[46] GUTOWSKY, H. S., AND PAKE, G. E. Structural Investigations by Means of Nuclear Magnetism. II Hindered Rotation in Solids. *The Journal of Chemical Physics 18*, 2 (1950), 162.

[47] HADDON, R. C., BRUS, L. E., AND RAGHAVACHARI, K. Electronic Structure and Bonding in Icosahedral C_{60}. *Chemical Physics Letters 125*, 5-6 (April 1986), 459–464.

[48] HADDON, R. C., HEBARD, A. F., ROSSEINSKY, M. J., MURPHY, D. W., DUCLOS, S. J., LYONS, K. B., MILLER, B., ROSAMILIA, J. M., FLEMING, R. M., KORTAN, A. R., GLARUM, S. H., MAKHIJA, A. V., MULLER, A. J., EICK, R. H., ZAHURAK, S. M., TYCKO, R., DABBAGH, G., AND THIEL, F. A. Conducting films of C_{60} and C_{70} by alkali-metal doping. *Nature 350* (March 1991), 320–322.

[49] HAHN, E. L. Spin Echoes. *Physical Review 80* (November 1950), 580.

[50] HAN, J. E., KOCH, E., AND GUNNARSSON, O. Metal-Insulator Transitions: Influence of Lattice Structure, Jahn-Teller Effect and Hund's Rule Coupling. *Physical Review Letters 84*, 6 (February 2000), 1276–1279.

[51] HEBARD, A. F. Buckminsterfullerene. *Annual Review of Materials Science 23* (August 1993), 159–191.

[52] HEBARD, A. F., ROSSEINSKY, M. J., HADDON, R. C., MURPHY, D. W., GLARUM, S. H., PALSTRA, T. T. M., RAMIREZ, A. P., AND KORTAN, A. R. Superconductivity at 18 K in potassium-doped C_{60}. *Nature 350* (April 1991), 600–601.

[53] HEINEY, P. A., FISCHER, J. E., MCGHIE, A. R., ROMANOV, W. J., DENENSTEIN, A. M., JR., J. P. M., AND III, A. B. S. Orientational Ordering Transition in Solid C_{60}. *Physical Review Letters 66*, 22 (June 1991), 2911–2914.

[54] HOMBORG, H., AND TESKE, C. L. Lithiumphthalocyanine: Darstellung und Charakterisierung der monoklinen und tetragonalen Modifikationen von LiPc(1-) und der Halogenaddukte LiPc(1-)X (X = Cl, Br, I). *Z. Anorg. Allg. Chem. 527* (1985), 45–61.

[55] IWASA, Y., SHIMODA, H., PALSTRA, T. T. M., MANIWA, Y., ZHOU, O., AND MITANI, T. Metal-insulator transition in ammoniated K_3C_{60}. *Physical Review B 53* (1996), R8836.

[56] JOSEPHSON, B. D. Coupled Superconductors. *Review of Modern Physics 36* (1964), 216.

[57] JOSEPHSON, B. D. The discovery of tunnelling supercurrents. *Review of Modern Physics 46* (1974), 251.

[58] KITTEL, C. *Introduction to Solid State Physics*, 3rd ed. John Wiley and Sons, New York, 1966.

[59] KOCH, E., GUNNARSSON, O., AND MARTIN, R. M. Filling Dependence of the Mott transition in the Degenerate Hubbard Model. *Physical Review B 60*, 23 (December 1999), 15714–15720.

[60] KOCH, E., GUNNARSSON, O., AND MARTIN, R. M. Metal-insulator Transitions in Generalized Hubbard Models. *Computer Physics Communications 127* (2000), 137–142.

[61] KRÄTSCHMER, W., LAMB, L. D., FOSTIROPOULOS, K., AND HUFFMAN, D. R. Solid C_{60}: a new form of carbon. *Nature 347* (September 1990), 354–358.

[62] KROTO, H. W., HEATH, J. R., O'BRIEN, S. C., CURL, R. F., AND SMALLEY, R. E. C_{60}: Buckminsterfullerene. *Nature 318* (1985), 162.

[63] LÜDERS, M., BORDONI, A., MANINI, N., CORSO, A. D., FABRIZIO, M., AND TOSATTI, E. Coulomb couplings in positively charged fullerene. *Philosophical Magazine B 82* (2002), 1611.

[64] LÜDERS, M., MANINI, N., GATTARI, P., AND TOSATTI, E. Hund's rule magnetism in C_{60} ions. *The European Physical Journal B 35* (September 2003), 57.

[65] Lecture notes from the training course in pulsed muon techniques. Published on the World Wide Web, February 2005. http://www.isis.rl.ac.uk/muons/trainingcourse/course2005.htm.

[66] LEZNOFF, C. C. *Phthalocyanines.* John Wiley and Sons, 1996.

[67] LIAO, M.-S., AND SCHEINER, S. Electronic Structure and Bonding in Metal Phthalocyanines, Metal=Fe, Co, Ni, Cu, Zn, Mg. *Journal of Chemical Physics 114*, 22 (June 2001), 9780–9791.

[68] LIU, X., XU, L.-C., HE, T.-J., CHEN, D.-M., AND LIU, F.-C. Density Functional Theory Investigation of Geometries and Electronic Spectra of Lithium Phthalocyanines. *Chemical Physics Letters 379* (2003), 517–525.

[69] LOF, R. W., VAN VEENENDAAL, M. A., KOOPMANS, B., AND SAWATZKY, G. A. Band Gap, Excitons and Coulomb Interaction in Solid C_{60}. *Physical Review Letters 68*, 26 (June 1992), 3924–3927.

[70] MACFARLANE, W. A., KIEFL, R. F., DUNSIGER, S., SONIER, J. E., CHAKHALIAN, J., FISCHER, J. E., YILDIRIM, T., AND CHOW, K. H. Muon-Spin-Relaxation Studies of the Alkali-Fulleride Superconductors. *Physical Review B 58*, 2 (July 1998), 1004–1024.

[71] MAN, P. P. Numerical Analysis of Hahn Echoes in Solids. *Physical Review B 52*, 13 (May 1995), 9418–9426.

[72] MAN, P. P. Numerical Analysis of Solomon Echo Amplitudes in Static Solids. *J. Chem. Phys. 106*, 10 (March 1997), 3908–3919.

[73] MANINI, N., TOSATTI, E., AND AUERBACH, A. Electron-vibron interactions in charged fullerenes. II. Pair energies and spectra. *Physical Review B 49* (1994), 13008.

[74] MANIWA, Y., SUGIURA, D., KUME, K., KIKUCHI, K., SUZUKI, S., ACHIBA, Y., HIROSAWA, I., TANIGAKI, K., SHIMODA, H., AND IWASA, Y. Determination of ^{13}C NMR Isotropic Knight Shift and Deviation from BCS Relation in A_3C_{60} Superconductors. *Physical Review B 54*, 10 (September 1999), R6861–R6864.

[75] MARGADONNA, S., PONTIROLI, D., BELLI, M., SHIROKA, T., RICCÓ, M., AND BRUNELLI, M. Li_4C_{60}: A Polymeric Fulleride with Two-Dimensional Architecture and Mixed Interfullerene Bonding Motifs. *J. Am. Chem. Soc. 126*, 46 (October 2004), 15032–15033.

[76] McCall, D. W., and Douglass, D. C. Nuclear Magnetic Resonance in Solid Adamantane. *The Journal of Chemical Physics 33* (1960), 777.

[77] Mckeown, N. B. *Phthalocyanine Materials - Synthesis, Structure and Function.* Cambridge University Press, 1998.

[78] Mehring, M., Thier, K.-F., Rachdi, F., and de Swiet, T. Localized and Delocalized Electronic States in A_1C_{60} (A=Rb, Cs). *Carbon 38* (2000), 1625–1633.

[79] Migdal, A. B. *Soviet Physics JETP 34* (1958), 996.

[80] Murphy, D. W., Rosseinsky, M. J., Fleming, R. M., Tycko, R., Ramirez, A. P., Haddon, R. C., Siegrist, T., and and, G. D. Synthesis and Characterization of Alkali Metal Fullerides: A_xC_{60}. *Journal of Physics and Chemistry of Solids 53*, 11 (November 1992), 1321–1332.

[81] O'Donnell, T. A. *Superacids and Acidic Melts as Inorganic Chemical Reaction Media.* VCH Publishers, Weinheim, Germany, 1993.

[82] Orti, E., and Brédas, J.-L. Photoelectron Spectra of Phthalocyanine Thin Films: A Valence Band Theoretical Interpretation. *Journal of Chemical Physics 92*, 2 (1990), 1228–1235.

[83] Orti, E., and Brédas, J.-L. Photoelectron Spectra of Phthalocyanine Thin Films: A Valence Band Theoretical Interpretation. *Journal of the American Chemical Society 114*, 22 (1992), 8669–8675.

[84] Paci, P., Capone, M., Cappelluti, E., Ciuchi, S., and Grimaldi, C. Isotope effects in the Hubbard-Holstein model within dynamical mean-field theory. *Physical Review B 74* (2006), 205108.

[85] Pagliari, M. Sintesi e Caratterizzazione di Fulleriti Cationiche. *PhD Thesis* (2007).

[86] Pake, G. E. Nuclear Resonance Absorption in Hydrated Crystals: Fine Structure of the Proton Line. *The Journal of Chemical Physics 16* (1948), 327.

[87] Pennington, C. H., and Stenger, V. A. Nuclear magnetic resonance of C_{60} and fulleride superconductors. *Reviews of Modern Physics 68*, 3 (July 1996), 855–910.

[88] Pontiroli, D. Synthesis, Structural Investigation and Spectroscopic Properties of Lithium Fullerides. *PhD Thesis* (2006).

[89] Powles, J. G., and Mansfield, P. Double-pulse nuclear-resonance transients in solids. *Physics Letters 2* (1962), 58.

[90] Prassides, K. *Fullerene-Based Materials Structure and Properties.* Structure and Bonding. Springer Verlag, 2004.

[91] Reed, C. A., Kim, K. C., Bolskar, R. D., and Mueller, L. J. Taming Superacids: Stabilization of the Fullerene Cations HC_{60}^{+} and $C_{60}^{\cdot+}$. *Science 289* (2000), 101.

[92] Riccò, M., Gianferrari, F., Pontiroli, D., Belli, M., Bucci, C., and Shiroka, T. Unconventional isotope effects in superconducting fullerides. *Europhysics Letters 81* (2008), 57002.

[93] Riccò, M., Shiroka, T., Belli, M., Pontiroli, D., Pagliari, M., Ruani, G., Palles, D., Margadonna, S., and Tomaselli, M. Unusual Polymerization in the Li_4C_{60} Fulleride. *Physical Review B 72* (2005), 155437.

[94] Riccò, M., Shiroka, T., Sartori, A., Bolzoni, F., and Tomaselli, M. Electronic properties of $(NH_3)_xNaK_2C_{60}$. *Europhysics Letters 53*, 6 (March 2001), 762–768.

[95] Rosseinsky, M. J. Recent Developments in the Chemistry and Physics of Metal Fullerides. *Chem. Mater. 10* (1998), 2665–2685.

[96] Schirber, J. E., Morosin, B., Kwei, G. H., Yildirim, T., Fischer, J. E., and Jorgensen, J. D. Superconductivity in the Polymeric Phase of Na_2CsC_{60}. *Physica C 353* (November 2001), 207–212.

[97] Sherwood, J. N. *The Plastically Crystalline State.* John Wiley and Sons, 1979.

[98] Shimoda, H., Iwasa, Y., Miyamoto, Y., Maniwa, Y., and Mitani, T. Superconductivity of fcc Fullerides Containing Off-Centered Octahedral Cations. *Physical Review B 54*, 22 (December 1996), R15653–R15656.

[99] Slichter, C. P. *Principles of Magnetic Resonance*, 3^{rd} ed. No. 1 in Springer series in solid-state sciences. Springer Verlag, Berlin, 1990.

[100] Stafström, S., and Fagerström, J. Electronic Structure and Stability of Fullerene Polymers. *Applied Physics A 64* (November 1997), 307–314.

[101] Sugano, S., Nishina, Y., and Ohnishi, S. *Microclusters.* Springer Verlag, 1987.

[102] Sumimoto, M., Sakaki, S., Matsuzaki, S., and Fujimoto, H. Significant Differences in Electronic Structure among X-, α- and β-Forms of Lithium Phthalocyanine. *Dalton Transactions* (2003), 31–33.

[103] Tosatti, E., Fabrizio, M., Tóbik, J., and Santoro, G. E. Strong Electron Correlations in Electron Doped Phthalocyanine Conductors Near Half Filling. *Physical Review Letters 93*, 11 (September 2004), 117002.

[104] Tycko, R., Dabbagh, G., Fleming, R. M., Haddon, R. C., Makhija, A. V., and Zahurak, S. M. Molecular Dynamics and the Phase Transition in Solid C_{60}. *Physical Review Letters 67*, 14 (September 1991), 1886–1889.

[105] Uemura, Y. J. μSR relaxation functions in magnetic materials. In *Muon Science. Muons in Physics, Chemistry and Materials* (Bristol and Philadelphia, 1999), S. H. K. S. L. Lee and E. R. Cywinski, Eds., vol. 51 of *SUSSP Proceedings, NATO ASI series*, Institute of Physics Publishing, pp. 85–114.

[106] Van Vleck, J. H. *The Theory of Electric and Magnetic Susceptibilities.* The International Series of Monographs in Physics. Oxford University Press, 1932.

[107] Van Vleck, J. H. The Dipolar Broadening of Magnetic Resonance Lines in Crystals. *Physical Review 74* (1948), 1168.

[108] W. G. Jenks, I. M. T., and Wikswo, J. P. *SQUIDS*, vol. 19 of *Encyclopedia of Applied Physics.* VCH Publishers, Inc., 1997.

[109] Werner, P. E., Eriksson, L., and Westdahl, M. TREOR, a semi-exhaustive trial-and-error powder indexing program for all symmetries. *Journal of Applied Physics 18* (1985), 367.

[110] Yoshinari, Y., Alloul, H., Brouet, V., Kriza, G., Holczer, K., and L.Forro. Molecular Motion and Phase Transition in K_3C_{60} and Rb_3C_{60} by Nuclear Magnetic Resonance. *Physical Review B 54*, 9 (September 1996), 6155–6166.

[111] Yoshinari, Y., Alloul, H., Kriza, G., and Holczer, K. Molecular motion and phase transition in K_3C_{60}: A ^{13}C NMR Study. *Physical Review Letters 71*, 15 (October 1993), 2413–2416.

[112] Zhou, O., Palstra, T. T. M., Iwasa, Y., Fleming, R. M., Hebard, A. F., Sulewski, P. E., Murphy, D. W., and Zegarski, B. R. Structural and electronic properties of $(NH_3)_xK_3C_{60}$. *Physical Review B 52* (1995), 483.

Acknowledgements

Un caro ringraziamento a tutti gli amici/colleghi... Matteo, Mauro, Daniele, Angelo, Marcello, Massimo che hanno seguito il mio lavoro di ricerca in questi anni, al lab. NMR in generale, a tutti i dottorandi o pseudo-dottorandi del dipartimento, ed infine, ma non per importanza a Toni, sempre presente fra noi anche se da qualche anno la Scienza lo ha chiamato all'estero.